

# High-resolution CMB bispectrum estimator



**Wu Hyun Sohn**

Department of Applied Mathematics and Theoretical Physics  
University of Cambridge

This dissertation is submitted for the degree of  
*Doctor of Philosophy*

Trinity College

August 2021



# Table of contents

<b>List of figures</b>	<b>vii</b>
<b>List of tables</b>	<b>xi</b>
<b>1 Introduction</b>	<b>1</b>
1.1 From background to foreground . . . . .	1
1.2 The homogeneous universe . . . . .	4
1.2.1 Geometry . . . . .	4
1.2.2 The FLRW universe . . . . .	6
1.2.3 Cosmic inventory . . . . .	7
1.2.4 Evolution of the universe . . . . .	10
1.3 Inflation . . . . .	12
1.3.1 The horizon problem . . . . .	13
1.3.2 Slow-roll inflation . . . . .	16
1.3.3 Quantum fluctuations . . . . .	18
<b>2 Cosmic Microwave Background Anisotropy</b>	<b>23</b>
2.1 The inhomogeneous universe . . . . .	23
2.1.1 Perturbation theory . . . . .	23
2.1.2 Boltzmann Equations . . . . .	24
2.1.3 CMB anisotropy . . . . .	24
2.2 Bispectrum . . . . .	24
2.3 CMB Bispectrum . . . . .	24
2.4 CMB polarisation . . . . .	24
<b>3 Bispectrum and Primordial Non-Gaussianity</b>	<b>25</b>
3.1 Bispectrum . . . . .	25
3.2 Primordial non-Gaussianity . . . . .	25
3.3 CMB bispectrum estimation . . . . .	25

3.3.1	CMB bispectrum . . . . .	25
<b>4</b>	<b>CMB Stage-4 Forecast</b>	<b>27</b>
4.1	Background . . . . .	27
4.2	Feature model bispectrum . . . . .	29
4.2.1	CMB bispectrum . . . . .	29
4.2.2	Feature model . . . . .	30
4.2.3	Separability . . . . .	31
4.3	Efficient computation of the estimator with polarisation . . . . .	32
4.3.1	Estimator . . . . .	32
4.3.2	Orthonormalising the covariance matrix . . . . .	33
4.3.3	Estimator for feature models . . . . .	34
4.3.4	Probing beam and instrumental noise . . . . .	35
4.3.5	Implementation and validation . . . . .	37
4.4	CMB-S4 forecast results . . . . .	37
4.4.1	Phase dependence . . . . .	37
4.4.2	$l_{max}$ dependence . . . . .	39
4.4.3	Beam and noise dependence . . . . .	39
4.4.4	Oscillation frequency dependence . . . . .	40
4.4.5	Comparison to scale invariant models . . . . .	43
4.5	Discussion . . . . .	45
<b>5</b>	<b>High-Resolution CMB Bispectrum Estimator</b>	<b>47</b>
5.1	Formalism . . . . .	49
5.1.1	CMB-BEst formalism . . . . .	49
5.1.2	Basis functions . . . . .	51
5.1.3	Primordial basis expansion . . . . .	54
5.2	Implementation and optimisation . . . . .	58
5.2.1	Algorithm . . . . .	59
5.2.2	Parallel computing . . . . .	62
5.2.3	Data locality . . . . .	64
5.3	Validation . . . . .	69
5.3.1	Internal consistency checks . . . . .	69
5.3.2	Consistency with Planck . . . . .	75
5.3.3	Proof of concept . . . . .	86
5.3.4	Future work . . . . .	87

Table of contents	v
-------------------	---

---

References	89
------------	----



# List of figures

1.1	Horizon problem . . . . .	14
1.2	Horizon problem . . . . .	15
4.1	Forecast error bars $\sigma^{T+E}$ versus the phase $\phi$ . Apart from the smallest frequency $\omega = 10$ , the error bar remains almost constant. This implies that the sine ( $\phi = 0$ ) and cosine ( $\phi = \pi/2$ ) feature models can be constrained independently. . . . .	38
4.2	Forecast error bars $\sigma_{\text{sin}}^{T+E}$ when multipoles $2 \leq l \leq l_{\text{max}}$ are included, in comparison with Planck. The oscillation frequency $\omega$ is set to 100 Mpc in all cases. Planck did not have access to the information from modes $l \geq 2000$ , but the CMB-S4 experiments are expected to be able to explore modes up to $l = 4000$ . . . . .	39
4.3	Beam (left) and noise (right) dependences of the forecast error $\sigma_{\text{sin}}^{T+E}$ for $\omega = 2000$ (top) and $\omega = 20$ (bottom). The noise level was set as $1\mu K \cdot \text{arcmin}$ for the first plot, while the second plot had fixed beam FWHM of $1'$ . We obtain less information from using wider beam and noisier sensors, as expected. . . . .	40
4.4	Frequency dependence of the forecast error in comparison to Planck (left). All CMB-S4 specifications would improve constraints on feature models. The most sensitive setup with $1'$ beam and $1\mu K \cdot \text{arcmin}$ noise is expected to yield error bars that are 1.6-2.1 times smaller than Planck. When the Planck results are combined with CMB-S4, we get even stronger constraints (right). . . . .	41
4.5	Frequency dependence of the forecast error from temperature data only, in comparison to Planck (left). The CMB-S4 experiments would perform worse than Planck when only the temperature map is concerned. After the addition of Planck data the error bars improve only marginally (right). This shows that polarisation data is crucial for constraining feature models. . . . .	42

4.6	Improvements on the forecast error when including E-mode polarisation data. Constraints from the CMB-S4 experiments would improve significantly from addition of the polarisation data. The improvement is maximised around $\omega \approx 200$ Mpc. . . . .	43
4.7	The maximum amplitude of oscillations detected in fractional variations of the projected power spectrum $C_l^{TT}$ and $C_l^{EE}$ , when extra oscillations $\sin(2\omega k)$ and $\cos(2\omega k)$ were imposed on the primordial power spectrum. Heuristically this shows that E-mode polarisation is more sensitive to the primordial oscillations, especially in the $\omega$ range of 70 to 300. Some peaks near $\omega = 70$ and 140 arise from resonances with Baryonic Acoustic Oscillations. . . . .	44
5.1	Tetrapyd domain in which the shape functions are defined. Left: the full region specified by triangle inequalities and an upper bound $k_{max}$ . Right: one sixth slice of the tetrapyd from which shape functions are uniquely determined by symmetry in the $k$ 's. Edges representing the equilateral, flattened and squeezed configurations are annotated. . . . .	54
5.2	Examples of our Legendre basis functions, evaluated on the sliced tetrapyd domain shown in Figure 5.1. Functions are defined as $Q_{p_1 p_2 p_3}(k_1, k_2, k_3) := P_{p_1}(k_1)P_{p_2}(k_2)P_{p_3}(k_3)$ , where $P_l(k)$ are Legendre polynomials. Here we plot $p_1 = p_2 = p_3 = p$ , where $p$ equals (a) 0, (b) 1, (c) 2, (d) 3, (e) 4, and (f) 5. A single colour map is used across plots: red and blue correspond to +1 and -1, respectively. . . . .	55
5.3	Cache block optimisation . . . . .	67
5.4	Map-by-map comparison of $f_{NL}$ estimates for standard templates, evaluated using each of the KSW and Legendre basis sets. Planck 2018 CMB map and 140 FFP10 simulations have been used, each representing a single point on the scatter plot shown left. Details of the linear best-fit to data (red dashed) is annotated below. On the right hand side shows a plot of $f_{NL}$ values for each map. In the ideal case where the two basis sets yield identical results, we should see all the points on $y = x$ for the left plot, and exactly overlapping graphs for the right. For more information on each of the three theoretical templates used, see e.g., [47]. . . . .	70



- 5.5 Map-by-map comparison of  $f_{NL}$  estimates for standard templates using the Legendre basis with different number of modes:  $p_{max} = 29$  and 30. The two results agree with error less than  $O(10^{-5})$ , as can be seen from the scatter plots (left) and map-by-map plots (right). This confirms that our expansion using Legendre polynomials has completely converged for these bispectrum shapes. . . . . 71
- 5.6 Map-by-map comparison of  $f_{NL}$  estimates for standard templates from the KSW and Legendre basis sets, similar to Figure 5.4. Here, the Legendre basis has a wider  $k$  domain:  $k_{max}/k_{min} = 2000$  instead of the usual 1000. Number of modes ( $p_{max}$ ) has been reduced to 10 instead of 30 for simplicity. We see that additional information from large scales (low  $k$ ) fixes the small scatter present in  $f_{NL}^{local}$  of the previous plot. . . . . 74
- 5.7 Contributions to the total  $f_{NL}$  from each point in the line-of-sight integral over  $r$  for standard templates. On the left hand side, we plot contributions from the cubic, linear, and lensing-ISW bias, as well as the total  $f_{NL}$ . Shown in blue is the  $1\sigma$  interval obtained from corresponding terms in 140 FFP10 Gaussian simulations. We focus on the  $r$  interval around recombination where most of the signal comes from. Plots on the right hand side show  $f_{NL}$  contributions over the whole  $r$  range in log scale. ISW effect, reionisation, and recombination are responsible for the three most noticeable peaks in all three plots. . . . . 76
- 5.8 Map-by-map comparison of the  $f_{NL}$  estimates obtained from CMB-BEst's Legendre basis set against the Modal estimator results for Planck 2018 analysis [49]. The first 140 FFP10 simulations are used. On the left hand side are scatter plots where each simulation is represented by a point according to  $f_{NL}$  estimates of standard templates. Their linear best fit lines are shown in dashed red. Results from the two routines are shown map by map on the right hand side. Overall, CMB-BEst and Modal are in good agreement, without any significant systematic errors. . . . . 79
- 5.9 Estimated  $f_{NL}$ 's for feature models with shape  $S(k_1, k_2, k_3) = \sin(\omega(k_1 + k_2 + k_3))$ , obtained using the Legendre basis with (blue) and Planck's Modal (black). Left: direct comparison of  $f_{NL}$  for different values of  $\omega$ . Error bars indicate the expected standard deviation in the estimator, calculated using 140 Gaussian simulations. Right: measured signal-to-noise  $f_{NL}/\sigma$ , again for a range of  $\omega$  values. Shaded in blue are the  $1\sigma$  and  $2\sigma$  levels. We see that the two approaches yield coherent estimates overall. . . . . 80

5.10	Correlations between feature model templates $S(k_1, k_2, k_3) = \sin(\omega(k_1 + k_2 + k_3) + \phi)$ with different $\omega$ values, for $\phi = 0$ (top two) and $\phi = \pi/2$ (bottom two). Results are from Legendre basis. ‘Sample’ correlations are obtained from the $f_{NL}$ estimates from 140 Gaussian simulations, while ‘theory’ correlations come from the inner product induced by $\Gamma_{p_1 p_2 p_3, p_1 p_2 p_3}$ matrix in (5.11). Large non-diagonal correlations appear around $\omega \approx 300$ , after which oscillations in the shape are no longer resolved by polynomials of degree up to $p_{max}$ . . . . .	81
5.11	Theoretical correlations between feature model templates with different frequency $\omega$ s, as described in Figure 5.10. The phase $\phi$ is set to zero in both cases, while the right plot is obtained from Legendre basis with a different $k$ range. The maximum $l$ value is reduced from 2500 to 2000, shifting $(k_{min}, k_{max})$ by a factor of $2000/2500 = 0.75$ . Having smaller $k$ range means fewer oscillations within the $k$ interval for same $\omega$ , which provides better effective resolution. The right plot does indeed show smaller non-diagonal correlations at high frequencies. . . . .	83
5.12	Constraints for the resonance shape $S(k_1, k_2, k_3) = \sin(\omega \log(k_1 + k_2 + k_3) + \phi)$ with varying $\omega$ s and $\phi$ set to 0 (left) and $\pi/2$ (right). Results are obtained using CMB-BEst’s Legendre basis (blue) and Planck’s Modal estimator (black). Top: signal-to-noise significance of the estimated $f_{NL}$ s with $1\sigma$ and $2\sigma$ levels shaded in blue. Bottom: standard deviations of the $f_{NL}$ estimates against frequency $\omega$ , calculated from the $f_{NL}$ s of 140 simulations (sample) and the $\Gamma$ matrix (theory). . . . .	84
5.13	Ratio between sample and theoretical variances obtained from Legendre basis for resonance shapes. Sampled variance is calculated from $f_{NL}$ estimates of 140 Gaussian simulations. $1\sigma$ and $2\sigma$ intervals are chosen based on a $\chi^2$ -distribution, which accurately describes sample variances as long as the $f_{NL}$ s are normally distributed. Results are statistically consistent with random fluctuations except potentially one at $\omega = 20$ , discussed in the main text. . . . .	85
5.14	Correlations between resonance model templates $S(k_1, k_2, k_3) = \sin(\omega \log(k_1 + k_2 + k_3) + \phi)$ with different $\omega$ values, for (a) $\phi = 0$ and (b) $\phi = \pi/2$ . ‘Sample’ correlations are obtained from the Legendre basis $f_{NL}$ estimates from 140 Gaussian simulations. ‘Theory’ correlations come from the inner product induced by $\Gamma$ matrix as shown in (5.36). . . . .	86
5.15	DBI sound speed scan . . . . .	87

# List of tables

1.1	Cosmic inventory. The fractional density values are quoted from Planck CMB analysis [50]. . . . .	9
1.2	Evolution of the universe. Ranges for the scale factor are computed from the cosmological parameters estimated in [50]. . . . .	12
4.1	Forecasts on the estimation errors of $f_{NL}$ for the constant model . . . . .	43
4.2	Expected improvement ratios of the $f_{NL}$ estimation errors for the CMB-S4 1' beam, $1\mu K$ arcmin setup, for various bispectrum templates. The local, equilateral and orthogonal results are quoted from [18]. . . . .	45
4.3	Expected improvements on the estimation errors of $f_{NL}$ for each combination of Planck / CMB-S4 temperature (T) and polarisation (E) data. Here the CMB-S4 assumes 1' beam and $1\mu K$ arcmin noise. For feature model the oscillation frequency $\omega = 200$ and phase $\phi = 0$ . The sky fraction $f_{sky} = 0.4$ for all cases except for Planck T + Planck E, for which $f_{sky} = 0.76$ . . . . .	45
5.1	Our index conventions for discretised arrays and their sizes. . . . .	58
5.2	Three levels of parallelism utilised in CMB-BEst. The levels and characteristics are chosen based on [29]. . . . .	65
5.3	Comparison of the sample and theoretical variances obtained from $f_{NL}$ estimates of standard shapes, computed using each of the KSW and Legendre basis sets. Sample variances are within $1\sigma$ interval from theoretical values assuming that the 140 individual $f_{NL}$ 's from simulated maps are normally distributed. This is statistically consistent with optimality of our bispectrum estimator. . . . .	72

---

5.4	Constraints on $f_{NL}$ for the standard shapes from the KSW and Legendre basis of CMB-BEst, in comparison with the Planck 2018 analysis [49]. Only the temperature data from the SMICA foreground-cleaned map and FFP10 simulations were used for the analysis. Values shown are after the lensing bias subtraction, with uncertainties at 68% CL. . . . .	77
5.5	Bias to $f_{NL}$ of standard shapes originating from the lensing bispectrum. We compare CMB-BEst's two different basis sets and the Planck 2018 analysis [49], using SMICA map and FFP10 simulations. . . . .	78

# Chapter 1

## Introduction

TODO:

- Last bit of Chapter 5
- First introduction in Chapter 1
- CMB anisotropy review in Chapter 2
- Bispectrum review in Chapter 3
- Explicitly mention which work is my own. Clarify work with Philip
- Add more references
- Include declaration
- Write dedication
- Typo checks

### 1.1 From background to foreground

New outline: - GR. Statistical homogeneity and isotropy -> FLRW metric. No static solution.

- Hubble's results. Expanding universe -> Big Bang.
- Discovery of CMB. CMB is a key prediction of Big Bang theory
- Big Bang theory's problem with initial conditions. Inflation. Quantum fluctuations as seeds for inhomogeneities of the universe.
- CMB anisotropy, 1 in  $10^5$ . Consistent with inflationary predictions.

- Observational evidence for dark energy and dark matter. Emergence of inflationary LCDM.

- LCDM successful. Planck CMB power spectrum -> consistent and measures parameters to percent level. Era of precision cosmology.

- Quick summary of CMB's usefulness! Its existence, anisotropy and spectrum all contributed... CMB probes initial conditions, growth of the universe and matter distribution (through lensing).

- Next big question - inflation's mechanism? Primordial non-Gaussianity is a robust prediction of many models. Three-point correlation function as a key statistic for differentiation.

- CMB bispectrum. Planck gave a lot of insight. No detection, but oscillatory models are of interest. Main challenge - computational complexity.

- Next generation of CMB experiments upcoming. Polarisation sensitivity improved, higher resolution. Need for development of new, improved pipeline capable of dealing with high resolution data.

- Thesis organisation.

Radio astronomers Arno Penzias and Robert Wilson were calibrating their 50-foot-long horn antenna when they found a mysterious background noise. The measurements were independent of time and location in the sky and persisted after the removal of various potential contaminants. After the theoretical work of Robert Dicke, Jim Peebles, and David Wilkinson was brought forward [16], Penzias and Wilson identified the noise as cosmic microwave background radiation (CMB): ancient light from the early universe reaching us after billions of years [44]. The discovery provided us with one of the most valuable probes of the physical universe, leading to major development in observational cosmology.

On the theoretical side, modern mathematical formulation of cosmology owes to Einstein's work on general relativity in 1915. Using his framework, Friedmann, Lemaître, Robertson, and Walker contributed to writing down the unique metric for spatially homogeneous and isotropic universe. The FLRW metric dictates growth of the universe from the Big Bang to present day. Such expansion of the universe was supported by Edwin Hubble's measurements of Cepheid variables and redshift (add year), as well as the aforementioned discovery of CMB. What is widely accepted to be the standard model of modern cosmology, the  $\Lambda$ CDM model, appeared only in the late 1990s. The six-parameter model assumes presence of cold dark matter and dark energy, in addition to baryons and radiation, as main contributors to the total energy density of the universe.

The  $\Lambda$ CDM model has been extremely successful in explaining modern cosmological observations. CMB measurements from *Planck* satellite, in particular, show exceptional agreement with the model. Planck was a space observatory developed by the European

Space Agency. The Planck satellite observed the CMB in nine frequency bands from 2009 to 2013, with resolution and sensitivity substantially improved compared to its predecessor - the Wilkinson Microwave Anisotropy Probe (WMAP). Able to resolve CMB anisotropy in much smaller scale, Planck placed one of the most stringent bounds on the theoretical parameters of  $\Lambda$ CDM so far.

How does CMB contain so much information about the universe? The answer is twofold. First is due to the fact that CMB anisotropy originates from primordial perturbations. Statistical properties of the initial fluctuations can be deduced from analysing correlation functions of the CMB, letting us constrain the early universe physics. Second reason is that CMB tracks history of the universe as it travels from the background to our foreground. CMB photons scatter with baryons before free-streaming all the way to our foreground, which then experience both growth of the universe and gravitational potential of matter perturbations. These signatures are engraved in CMB anisotropy spectrum, redshift, and weak lensing.

The CMB anisotropy is observed to be nearly Gaussian distributed. Statistical characteristics of a Gaussian random field can be summarised entirely using two-point correlation functions, or their Fourier counterpart: power spectrum. The CMB power spectra have been thoroughly studied to constrain various cosmological parameters. Meanwhile, higher-order statistics such as three-point correlation functions (bispectrum in Fourier space) also contain valuable information about our universe. They probe non-Gaussian statistics of the CMB arising from both primordial origin and late-time effects.

Primordial non-Gaussianity is a key statistic for studying physics of the early universe. The theory of inflation has been successful in describing the observed data, but its exact mechanism is yet undetermined. Currently there are numerous viable inflationary models with well-founded physical motivations. Non-Gaussian signatures of primordial fluctuations are robust predictions of various models, and measuring their shape and amplitude allows us to constrain inflationary scenario. CMB bispectrum analysis from Planck yielded the most precise measurements of primordial non-Gaussianity to date. So far, no statistically significant amount of non-Gaussianity has been detected.

In the near future, we expect several new major CMB experiments. Simons Observatory (SO) is a ground-based experiment currently under construction in the Atacama Desert of Chile. SO is expected to measure both CMB temperature and polarisation to unprecedented precision, largely improved compared to Planck. The first light from SO is planned to be observed in early 2022. Many more CMB Stage-4 (CMB-S4) experiments are proposed, brightening future prospects for CMB. In particular, the upcoming measurements will allow us to constrain primordial non-Gaussianity further, providing discovery potential.

This thesis is organised as follows. In Chapter 1, we review the standard formulation of cosmology, deriving the form of scale factor in homogeneous universe. Motivation and formalism of slow-roll inflation is also presented here. Chapter 2 details cosmological perturbation theory, with a focus on the CMB anisotropy. We summarise methods for computing the transfer function of CMB, and introduce the concept of CMB polarisation. Next, in Chapter 3 we define bispectrum and discuss how it can be used to probe primordial non-Gaussianity. An example of single-field inflation with non-canonical kinetic term will be provided to demonstrate computation of non-Gaussianity using the in-in formalism.

Chapters 4 and 5 contain my original work, based on research conducted in collaboration with my supervisor James Fergusson. Chapter 4 contains the forecast for future CMB-S4 surveys on the primordial non-Gaussianity parameter  $f_{NL}$ . SO experiment specifications and expected CMB-S4 setup were used to predict their improved constraints via Fisher information analysis. We focussed on models with oscillatory features, where steep enhancement in polarisation sensitivity greatly benefit constraining power.

Motivated by the positive prospects from forecasts detailed in Chapter 4, we worked on developing a high-resolution bispectrum estimation pipeline suitable for future surveys. Chapter 5 contains formulation and development details of the developed program, as well as consistency checks from the thorough verification process. We outline the benefits of new pipeline compared to conventional methods and present some working examples. Lastly, Chapter 6 concludes the thesis by summarising and presenting plans for future research.

## 1.2 The homogeneous universe

In this section we review the standard cosmological formulation for the homogeneous universe, neglecting any perturbations. What we derive here will serve as a background solution for the full perturbative result discussed in the next chapter. We assume general relativity to be an accurate theory of gravity for relevant scales.

### 1.2.1 Geometry

In general relativity, spacetime is represented by a 4-dimensional Lorentzian manifold equipped with a metric. Distance measure in curved spacetime is given by the metric tensor  $g$ ;

$$ds^2 = g_{\mu\nu} dx^\mu dx^\nu, \quad (1.1)$$



where the Greek letters  $\mu, \nu = 0, 1, 2, 3$  represent time (0) and spatial (1, 2, 3) indices of local coordinates. Flat spacetime has metric  $g_{\mu\nu} = \eta_{\mu\nu} = \text{diag}\{-1, 1, 1, 1\}$ , also known as the Minkowski metric. Throughout this thesis we adopt the sign convention  $(-, +, +, +)$  and work in units where  $c = 1$ . Unless specified otherwise, the Einstein summation convention is assumed.

In curved spacetime, free particles follow a trajectory given by the geodesic equation;

$$\frac{d^2 x^\mu}{ds^2} + \Gamma_{\nu\rho}^\mu \frac{dx^\nu}{ds} \frac{dx^\rho}{ds} = 0, \quad (1.2)$$

with  $s$  an affine parameter parametrising the trajectory, and  $\Gamma_{\nu\rho}^\mu$  the Christoffel symbol representing metric connection. Its value is given in terms of the metric tensor by

$$\Gamma_{\nu\rho}^\mu = \frac{1}{2} g^{\mu\sigma} (\partial_\rho g_{\nu\sigma} + \partial_\nu g_{\rho\sigma} - \partial_\sigma g_{\nu\rho}). \quad (1.3)$$

Here and throughout this thesis,  $\partial_\mu$  denote the partial derivative with respect to local coordinate  $x^\mu$ . Note  $g^{\nu\sigma}$  is the inverse metric satisfying  $g^{\mu\nu} g_{\nu\rho} = \delta_\rho^\mu$ .

Defining tangent vector as  $U^\mu = dx^\mu/ds$ , the equation can be rewritten in a covariant form given by

$$(\nabla_U U)^a = U^b \nabla_b U^a = 0. \quad (1.4)$$

We follow the convention where Roman letters are used for abstract indices. Note that in terms of local coordinates, the covariant derivative of a vector field is defined as  $\nabla_\nu U^\mu = \partial_\nu U^\mu + \Gamma_{\nu\rho}^\mu U^\rho$ .

Distance between two geodesics that are initially parallel may change in curved spacetime. Such geometric information is encapsulated within the Riemann curvature tensor  $R_{bcd}^a$ .<sup>1</sup> From  $R_{bcd}^a$  we can evaluate the Ricci curvature tensor  $R_{ab}$ , the Ricci scalar  $R$ , and finally the Einstein tensor  $G_{ab}$ . They are defined as follows.

$$R_{\nu\rho\sigma}^\mu := \partial_\rho \Gamma_{\nu\sigma}^\mu - \partial_\sigma \Gamma_{\nu\rho}^\mu + \Gamma_{\nu\sigma}^\tau \Gamma_{\tau\rho}^\mu - \Gamma_{\nu\rho}^\tau \Gamma_{\tau\sigma}^\mu \quad (1.5)$$

$$R_{\mu\nu} := R_{\mu\rho\nu}^\rho \quad (1.6)$$

$$R := g^{\mu\nu} R_{\mu\nu} \quad (1.7)$$

$$G_{\mu\nu} := R_{\mu\nu} - \frac{1}{2} g_{\mu\nu} R \quad (1.8)$$

<sup>1</sup>Consider a 1-parameter family of geodesics  $\gamma(s, t)$ , where  $t$  is an affine parameter. The geodesic deviation equation states  $T^\rho \nabla_\rho (T^\nu \nabla_\nu S^\mu) = R_{\nu\rho\sigma}^\mu T^\nu T^\rho S^\sigma$ , where tangent vectors  $T = \partial/\partial t$ ,  $S = \partial/\partial s$ .

The Einstein tensor is symmetric, i.e.  $G_{\mu\nu} = G_{\nu\mu}$ . It is also important to note that its divergence vanishes;  $\nabla^\mu G_{\mu\nu} = 0$ , which can be proven using the contracted Bianchi identity.

### 1.2.2 The FLRW universe

On very large scales, our universe is observed to be uniform in space (homogeneous) and not have a favoured direction (isotropic). Spatial part of the homogeneous and isotropic metric has constant curvature and can be categorised into three: spherical ( $\mathbb{S}^3$ ), Euclidean ( $\mathbb{E}^3$ ), and hyperbolic ( $\mathbb{H}^3$ ). They are induced from embedding  $\mathbb{R}^3$  into submanifolds of  $\mathbb{R}^4$  equipped with the Euclidean metric, defined as  $K|\mathbf{x}|^2 + u^2 = 1$ . Here  $K = 1, 0, -1$  for  $\mathbb{S}^3$ ,  $\mathbb{E}^3$ , and  $\mathbb{H}^3$ , respectively. Writing the embedding as  $f : x^i = (x, y, z) \mapsto X^I = (x, y, z, \sqrt{1 - K(x^2 + y^2 + z^2)})$ , the induced metric

$$\gamma_{ij} := \frac{\partial X^I}{\partial x^i} \frac{\partial X^J}{\partial x^j} \delta_{IJ} = \delta_{ij} + \frac{x_i x_j}{1 - K x_k x^k}. \quad (1.9)$$

The spatial line element is therefore given by

$$dl^2 = \gamma_{ij} dx^i dx^j = d\mathbf{x} \cdot d\mathbf{x} + \frac{K(\mathbf{x} \cdot d\mathbf{x})^2}{1 - K(\mathbf{x} \cdot \mathbf{x})} \quad (1.10)$$

$$= \frac{1}{1 - Kr^2} dr^2 + r^2 d\Omega^2, \quad (1.11)$$

where the angular line element  $d\Omega^2 = d\theta^2 + \sin^2 \theta d\phi^2$ .

We may now write down the form of the metric describing our universe in large scales;

$$ds^2 = -dt^2 + a(t)^2 \left( \frac{1}{1 - Kr^2} dr^2 + r^2 d\Omega^2 \right). \quad (1.12)$$

This is known as the FLRW metric, named after independent researchers who worked on the topic. Function  $a(t)$  is called the scale factor and it dictates the growth of universe over time. Note that the metric is invariant under rescaling  $a \rightarrow \lambda a$ ,  $r \rightarrow r/\lambda$ , and  $K \rightarrow k := \lambda^2 K$ . Hence we may set the scale factor to be  $a(t_0) = 1$  at present time, at the cost of replacing  $K \in \{-1, 0, 1\}$  by  $k \in \mathbb{R}$ .

Levi-Civita connection corresponding to the FLRW metric can be computed using the definition (1.3). Its non-zero components are given as follows.

$$\Gamma_{ij}^0 = \frac{\dot{a}}{a} \gamma_{ij}, \quad (1.13)$$

$$\Gamma_{j0}^i = \Gamma_{0j}^i = \frac{\dot{a}}{a} \delta_j^i, \quad (1.14)$$

$$\Gamma_{jk}^i = \frac{1}{2a^2} \gamma^{il} (\partial_k \gamma_{jl} + \partial_j \gamma_{kl} - \partial_l \gamma_{jk}). \quad (1.15)$$

Overdot denotes time derivative  $(\dot{\phantom{x}}) := \partial/\partial t$  here and for the rest of this thesis. Indices for  $\gamma$  are raised and lowered using  $\gamma$ , not  $g$ .

Note that a path defined by  $t(\tau) = \tau$  and  $\mathbf{x}(\tau) = \text{const}$  is a timelike geodesic satisfying the geodesic equations (1.2). *Comoving* observers who follow these paths continue to perceive the expanding universe to be isotropic. Meanwhile, they find themselves drift apart, as the physical distance  $r_{\text{phys}} = a(t)r$  grows in time.

Ricci curvature and Einstein tensor of the FLRW metric follows from definitions (1.5-1.8);

$$R_{00} = -\frac{3\ddot{a}}{a} \quad (1.16)$$

$$R_{ij} = \left[ \frac{\ddot{a}}{a} + 2 \left( \frac{\dot{a}}{a} \right)^2 + \frac{2k}{a^2} \right] a^2 \gamma_{ij}, \quad (1.17)$$

$$R = 6 \left[ \frac{\ddot{a}}{a} + \left( \frac{\dot{a}}{a} \right)^2 + \frac{k}{a^2} \right], \quad (1.18)$$

$$G_{00} = 3 \left[ \left( \frac{\dot{a}}{a} \right)^2 + \frac{k}{a^2} \right], \quad (1.19)$$

$$G_{ij} = \left[ -\frac{2\ddot{a}}{a} - \left( \frac{\dot{a}}{a} \right)^2 - \frac{k}{a^2} \right] a^2 \gamma_{ij}. \quad (1.20)$$

While deriving (1.17) we used the fact that the Ricci tensor of three-dimensional spatial metric  $\gamma$  is equal to  $2k\gamma_{ij}$ .<sup>2</sup> Also note that components  $G_{0i}$  vanish and  $G_{ij} \propto g_{ij}$ , which is expected for a spatially homogeneous and isotropic spacetime.

### 1.2.3 Cosmic inventory

According to general relativity, spacetime is curved by its contents. Particles interact with gravity through the energy-momentum tensor  $T_{\mu\nu}$ , which encapsulates their energy, mo-

<sup>2</sup>In general, the Ricci tensor of any  $n$ -dimensional constant-curvature space with metric  $g_{ij}$  is given by  $R_{ij} = (n-1)\kappa g_{ij}$ . Here  $\kappa$  denotes sectional curvature of the space, which is equal to  $k$  for  $\gamma$  defined in (1.9).

momentum flux, and stress. Thanks to spatial homogeneity and isotropy, components of the homogenous universe can be modelled as *perfect* fluids; they are completely characterised by their rest frame energy density and isotropic pressure. Defining the 4-velocity to be  $U^\mu = dx^\mu/ds$ <sup>3</sup>, the energy-momentum tensor of a perfect fluid is given by

$$T_{\mu\nu} = (\rho + P)U_\mu U_\nu + P g_{\mu\nu}, \quad (1.21)$$

where the energy density  $\rho$  and pressure  $P$  only depends on time. For an observer comoving with the fluid,  $T = \text{diag}\{\rho, P, P, P\}$ .

Divergence of the energy-momentum tensor vanishes for a perfect fluid;

$$\nabla_\nu T^{\mu\nu} = (\rho + P)\nabla_\nu (U^\mu U^\nu) + P\nabla_\mu g^{\mu\nu} \quad (1.22)$$

$$= (\rho + P) (U^\mu \nabla_\nu U^\nu + U^\nu \nabla_\mu U^\nu) + \nabla_\mu g^{\mu\nu} \quad (1.23)$$

$$= 0. \quad (1.24)$$

The first term in (1.23) vanishes because the fluid's 4-velocity satisfies the geodesic equation (1.2). Incompressibility implies that  $\nabla_\nu U^\nu = 0$ , and we see the second term also vanishes. The last term is zero since the Levi-Civita connections are *metric*; i.e.,  $\nabla g = 0$ .

Using connections of the FLRW metric computed in the previous section, the  $\mu = 0$  component of (1.24) yields the continuity equation;

$$\dot{\rho} + \frac{3\dot{a}}{a}(\rho + P) = 0. \quad (1.25)$$

Further imposing a constant equation of state  $w = P/\rho$ ,

$$\frac{\dot{\rho}}{\rho} + 3(1+w)\frac{\dot{a}}{a} = 0, \quad (1.26)$$

$$\rho \propto a^{-3(1+w)}. \quad (1.27)$$

The universe contains a number of different components, but all known particles can be broadly categorised into three: radiation, matter, and dark energy.

Radiation consists of photons and neutrinos. The energy-momentum tensor of radiation is traceless, fixing the equation of state to be  $w = 1/3$ . While the number density of photons decrease as  $\propto a^{-3}$ , their energy density scales as  $\propto a^{-4}$  instead because their wavelength

---

<sup>3</sup>Here  $s$  is an affine parametrisation of geodesic followed by the fluid. It is equal to proper time  $\tau$  for massive particles geodesics, and  $g_{\mu\nu}U^\mu U^\nu = -1$ . Massless particles such as photons follow null trajectory, and  $s$  is chosen so that  $g_{\mu\nu}U^\mu U^\nu = 0$ .

gets stretched out as the universe expands. We define the *redshift*  $z$  to quantify this effect;

$$1 + z := \frac{1}{a}. \quad (1.28)$$

Hence, a photon with original wavelength  $\lambda_0$  gets redshifted by  $\Delta\lambda = z\lambda_0$ . Note that the redshift is directly related to the scale factor  $a(t)$ . It can be used to parametrise time, as well as distance to a light source. Neutrinos show similar behaviours to photons since they remain ultra-relativistic.

Matter includes cold dark matter, electrons and protons. The latter two are often grouped as baryons, even though electrons are not technically baryonic. Pressure from non-relativistic matter is negligible, and  $w = 0$ . Their number density scales  $\propto a^{-3}$  as the universe expands, and so does their energy density. Cold dark matter constitutes about 85% of the matter and a significant proportion of the total energy density today.

Dark energy is perhaps the most mysterious of the three, despite having the largest contribution to the total energy density at present time. First evidence of its existence came from Type Ia supernovae measurements which implied that the universe's expansion is accelerating. Subsequent observations of CMB and baryonic acoustic oscillations provided further proof. Exact physical mechanism for dark energy is not yet known, but potential explanations include the cosmological constant and quintessence. For purposes of the  $\Lambda$ CDM model, dark energy has negative pressure ( $w = -1$ ), hence its energy density is independent of the scale factor.

Table 1.1 summarises the species of the universe and their properties discussed above. The last column contains fractional energy density of particles and shows how abundant each species are at present time. Precise definition of fractional density is to follow in the next section.

Table 1.1 Cosmic inventory. The fractional density values are quoted from Planck CMB analysis [50].

	Examples	Equation of State	Density Growth	Fractional Density Today
Radiation ( $r$ )	Photon ( $\gamma$ )	$w = 1/3$	$\rho \propto a^{-4}$	$\Omega_\gamma \approx 1 \times 10^{-4}$
	Neutrino ( $\nu$ )			$\Omega_\nu < 2 \times 10^{-2}$
Matter ( $m$ )	Cold dark matter ( $c$ )	$w = 0$	$\rho \propto a^{-3}$	$\Omega_c \approx 0.27$
	Baryon ( $b$ )			$\Omega_b \approx 0.05$
Dark Energy ( $\Lambda$ )		$w = -1$	$\rho = \text{const}$	$\Omega_\Lambda \approx 0.68$

### 1.2.4 Evolution of the universe

We are now ready to calculate the time evolution of the homogeneous universe. The Einstein field equation of general relativity reads

$$G_{\mu\nu} = 8\pi G T_{\mu\nu}, \quad (1.29)$$

where  $G$  is the Newtonian constant of gravitation.<sup>4</sup> Substituting in the Einstein tensor for the FLRW metric from (1.19-1.20) and the energy-momentum tensor from (1.21), we obtain

$$3 \left[ \left( \frac{\dot{a}}{a} \right) + \frac{k}{a^2} \right] = 8\pi G \rho, \quad (1.30)$$

$$-\frac{2\ddot{a}}{a} - \left( \frac{\dot{a}}{a} \right)^2 - \frac{k}{a^2} = 8\pi G P. \quad (1.31)$$

Rearranging above yields the Friedmann equations;

$$\left( \frac{\dot{a}}{a} \right)^2 = \frac{8\pi G}{3} \rho - \frac{k}{a^2}, \quad (1.32)$$

$$\frac{\ddot{a}}{a} = -\frac{4\pi G}{3} (\rho + 3P). \quad (1.33)$$

Note that the continuity equation (1.25) can be obtained from (1.33) and the time derivative of (1.32).

The Hubble parameter is defined as  $H := \dot{a}/a$ . From (1.32) we may compute the critical energy density for which the curvature  $k$  vanishes;

$$\rho_{\text{crit},0} := \frac{3H_0^2}{8\pi G}. \quad (1.34)$$

Subscripts 0 indicate that they are evaluated at present time  $t = t_0$ , where  $a(t_0) = 1$ .

In reality, energy density and pressure appearing in the Friedmann equations are sums of contributions from different fluid components. Fractional density of a given fluid X is defined as

$$\Omega_X := \frac{\rho_X}{\rho_{\text{crit},0}}. \quad (1.35)$$

In previous section we derived how each fluid's energy density depends on the scale factor. Quoting results summarised in Table 1.1, the Friedmann equations can be rewritten as

---

<sup>4</sup>Constant  $G$  is not to be confused with the Einstein tensor  $G_{\mu\nu}$  on the left hand side.

follows;

$$\dot{a}^2 = H_0^2 \left( \frac{\Omega_{r,0}}{a^2} + \frac{\Omega_{m,0}}{a} + \Omega_{\Lambda,0} a^2 \right) - k, \quad (1.36)$$

$$\ddot{a} = H_0^2 \left( -\frac{\Omega_{r,0}}{a^3} - \frac{\Omega_{m,0}}{2a^2} + \Omega_{\Lambda,0} a \right). \quad (1.37)$$

These equations dictate the growth (or shrinking) of the universe given curvature and energy density composition today. For  $k \leq 0$ , the right hand side of (1.36) is always positive regardless of fractional density value. In this case, the fact that universe is currently expanding suffices to show that scale factor  $a$  has been increasing monotonically. The universe began with the Big Bang at  $a = 0$ .

When  $k > 0$ ,  $\dot{a}$  vanishes at one or two values of  $a$ . There are multiple scenarios in this case, including the Einstein's Static Universe (ESU) where  $\dot{a} = \ddot{a} = 0$ . The ESU is however unstable; perturbing around the static solution as  $a(t) = a_{\text{ESU}}(1 + \xi(t))$  in (1.37) gives  $\ddot{\xi} > 0$  to leading order, which implies that there exists a growing solution for  $\xi$ . In fact, there are no stable static solutions to the Friedmann equations, rendering such models implausible. Another possibility is a closed universe, where the scale factor grows until it hits the maximum and then decreases. This scenario requires  $\ddot{a} < 0$  at all times. Measurements of Type Ia supernovae strongly suggest that the universe is in an accelerating phase, ruling out this option as well. Lastly, there is the bouncing universe model. The scale factor starts large, drops to a minimum value, and bounces back to an accelerating growth. This model has been disregarded due to the need for introduction of various new physics in the early universe, but has recently regained popularity as an alternative to inflation.

Constraints from modern cosmological observations indicate that our universe is extremely flat, with  $k \approx 0$ . For the rest of this thesis we set the curvature  $k = 0$  and follow a standard Big Bang theory.

Note the different powers of the scale factor  $a$  are associated with each component of the universe in (1.36). According to the CMB measurements  $\Omega_{r,0} \ll \Omega_{m,0} < \Omega_{\Lambda,0}$ . The energy density is therefore dominated by a single component at a time, resulting in three different eras:

- Radiation domination (RD) where  $0 < a < \Omega_{r,0}/\Omega_{m,0}$ ,
- Matter domination (MD) with  $\Omega_{r,0}/\Omega_{m,0} < a < (\Omega_{m,0}/\Omega_{\Lambda,0})^{1/3}$ , and
- Dark energy domination ( $\Lambda$ D) for  $a > (\Omega_{m,0}/\Omega_{\Lambda,0})^{1/3}$ .

When the universe consists mainly of a single fluid component  $X$ , we can simplify the Friedmann equations as follows;

$$\dot{a}^2 = H_0^2 \Omega_{X,0} a^{-1-3w_X}, \quad (1.38)$$

$$a \propto t^{\frac{2}{3(1+w_X)}}, \text{ if } w_X \neq -1. \quad (1.39)$$

Note that the scale factor grows exponentially for  $\Lambda$ D as  $w_\Lambda = -1$ ;  $a \propto \exp(Ht)$ .

It is often convenient to consider *conformal* time defined as  $\tau := \int_{t_i}^t (1/a(t')) dt'$ , for some initial time reference  $t_i$ . As  $dt = a d\tau$ , the flat FLRW metric is given in terms of conformal time by

$$ds^2 = -dt^2 + a(t)^2 d\mathbf{x}^2 = a(t)^2 [-d\tau^2 + d\mathbf{x}^2]. \quad (1.40)$$

Rewriting (1.38) with  $da/d\tau = a\dot{a}$ , we obtain

$$a \propto \tau^{\frac{2}{3w_X+1}}. \quad (1.41)$$

Calculations in this section are summarised in Table 1.2.

Table 1.2 Evolution of the universe. Ranges for the scale factor are computed from the cosmological parameters estimated in [50].

Era	Scale Factor	Growth (comoving)	Growth (conformal)
Radiation Domination	$a < 2.9 \times 10^{-4}$	$a \propto t^{1/2}$	$a \propto \tau$
Matter Domination	$2.9 \times 10^{-4} < a < 0.77$	$a \propto t^{2/3}$	$a \propto \tau^2$
Dark Energy Domination	$a > 0.77$	$a \propto e^{Ht}$	$a \propto -1/\tau$

### 1.3 Inflation

Soon after the quantitative formulation of Big Bang cosmology, several issues with the initial conditions were raised. The CMB was observed to be nearly homogeneous, even though many parts of it should have been causally disconnected at the time. Curvature of the universe is extremely close to zero, while  $k = 0$  is an unstable stationary point. The standard Big Bang cosmology provided little justification for such initial smoothness and fine-tuning.



The theory of cosmic inflation not only resolved most of these problems successfully, but also provided a physical mechanism for the generation of inhomogeneities in the universe. Quantum fluctuations of the inflationary field seeds the initial conditions, whose statistical properties are consistent with current observations. Inflation has therefore become the most widely accepted theory of the early universe to date.

In this section we formulate the puzzles which led to the introduction of inflation (1.3.1) and outline the basic inflationary paradigm (1.3.2).

### 1.3.1 The horizon problem

According to relativity, information cannot travel faster than the speed of light. It is therefore possible to have two different points in spacetime that are causally disconnected; their lightcones do not intersect, so no events since the Big Bang could have affected both. Physical properties at such two points are independent of each other. The aim of this section is to compute the size of causally disjoint regions at the epoch of recombination, when most of the CMB photons start free-streaming.

Consider a photon travelling in a straight line. Writing the radial part of  $d\mathbf{x}^2$  as  $d\chi^2$ , our spacetime metric (1.40) becomes

$$ds^2 = a(\tau)^2(-d\tau^2 + d\chi^2). \quad (1.42)$$

Photons follow null geodesics, meaning  $ds^2 = 0$  along their trajectories. Thus  $\chi(\tau) = \tau + \text{const}$  or  $\chi(\tau) = -\tau + \text{const}$ . They appear to be straight and diagonal lines on the  $\chi$ - $\tau$  plane, as shown in Figure 1.1. The distance light travels starting from some initial time  $\tau_i$  to  $\tau_f$  is then given by

$$\chi_{\text{PH}} := \tau_f - \tau_i = \int_{a_i}^{a_f} \frac{d\tau}{da} da = \int_{a_i}^{a_f} \frac{1}{a\dot{a}} da. \quad (1.43)$$

Here,  $\chi_{\text{PH}}$  is called the particle horizon. No particles could have travelled further than this distance since the initial time  $\tau_i$ .

Suppose that the universe is dominated by a single perfect fluid  $X$  in between  $a_i$  and  $a_f$ . The simplified Friedmann equation (1.38) then gives

$$\chi_{\text{PH}} = \int_{a_i}^{a_f} \frac{a^{(3w_X-1)/2}}{H_0 \sqrt{\Omega_{X,0}}} da = \frac{2}{(3w_X+1)H_0 \sqrt{\Omega_{X,0}}} \left( a_f^{(3w_X+1)/2} - a_i^{(3w_X+1)/2} \right). \quad (1.44)$$

Note that the particle horizon is bounded as  $a_i \rightarrow 0$  if and only if  $3w_X + 1 > 0$ .

According to the conventional big bang cosmology, the universe begins at  $a_i = 0$  with radiation contributing the most to energy density. The CMB last scattering surface lies around redshift  $z \sim 1090$  (or  $a_{\text{rec}} = 9.17 \times 10^{-4}$ ) in matter domination era. Quoting cosmological parameters from tables 1.1 and 1.2, as well as treating radiation and matter domination separately in the integral, we get  $\chi_{\text{CMB}} \approx 340$  Mpc.

Conformal distance to the last scattering surface  $\chi_*$  can also be computed using the same formula (1.44), now integrating from  $a_{\text{rec}}$  to  $a_0 = 1$ . Approximating again by separating matter and dark energy domination era,  $\chi_* \approx 15000$  Mpc. This is much larger than  $\chi_{\text{PH}}$ !

As shown in Figure 1.1, CMB photons at two different opposite sides of the sky had no causal contact at all; their particle horizons have zero overlap. Furthermore,  $\chi_{\text{CMB}}/\chi_* \approx 1.3$  degrees. Every disjoint 1.3deg patch in the sky were causally unrelated at the time of recombination. There is no obvious reason for cosmological parameters in these patches to be similar. Despite this fact, the observed CMB is isotropic everywhere in temperature to order  $O(10^{-5})$ . This is the horizon problem; the universe at recombination is too homogeneous considering the small particle horizon then.

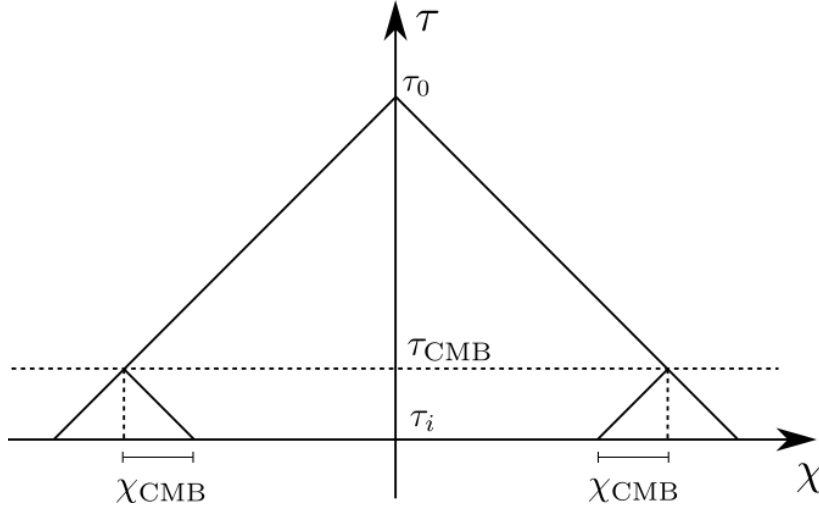


Fig. 1.1 The horizon problem. According to the conventional big bang cosmology, different regions of the CMB we observe today have had no overlap in their particle horizon. Yet, the CMB is measured close to uniform everywhere.

To resolve this issue, we need the particle horizon at recombination to be larger. The theory of cosmic inflation achieves this by having a period in the early universe where  $3w + 1 < 0$ . In this case, we see from (1.44) that  $\chi_{\text{PH}}$  is unbounded as  $a_i \rightarrow 0$ . The initial conformal time  $\tau_i \rightarrow -\text{inf}$ , allowing enough proper time for the particle horizon growth. Then even the two opposite regions of the CMB we see can have had causal contact in the past, as depicted in Figure 1.2.

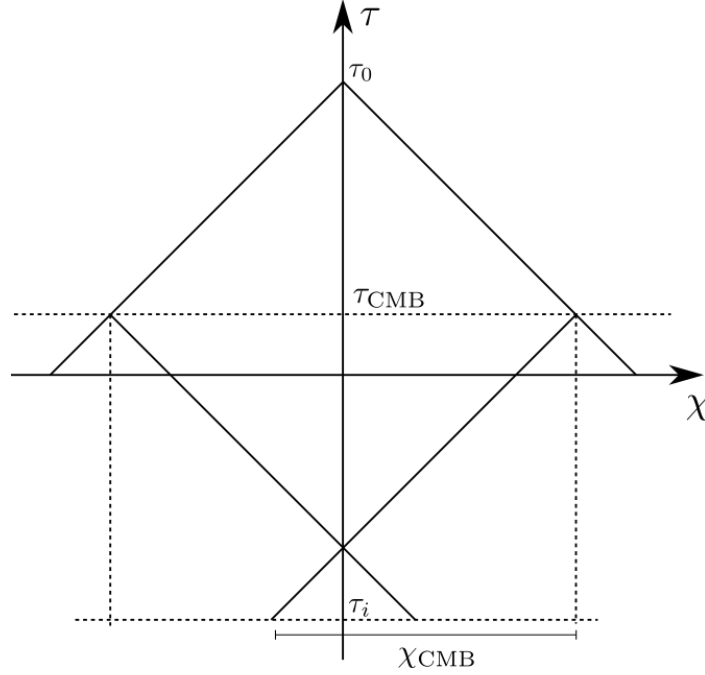


Fig. 1.2 Solution to the horizon problem. Inflation allows more conformal time for different regions to have been in causal contact before recombination.

Inflation can alternatively be characterised using the comoving hubble radius defined as

$$\mathcal{H}^{-1} := \frac{1}{aH}. \quad (1.45)$$

Note that the particle horizon can then be expressed in terms of the comoving hubble radius as

$$\chi_{\text{PH}} = \int_{a_i}^{a_f} \frac{1}{a\dot{a}} da = \int_{\ln a_i}^{\ln a_f} \mathcal{H}^{-1} d \ln a. \quad (1.46)$$

The particle horizon represents the distance where objects could have *ever* talked to each other. On the other hand, the comoving hubble radius is a scale for how far information can reach *now*.<sup>5</sup> As can be seen from (1.44),  $\mathcal{H}^{-1} \propto a^{(3w_X+1)/2}$ , which is  $\propto a$  for radiation domination and  $\propto a^{1/2}$  during matter domination.

Inflation explains homogeneity of the observed CMB by requiring  $\mathcal{H}^{-1}$  to have shrunk rapidly in early times;  $d\mathcal{H}^{-1}/d \ln a < 0$ . We find that  $\ddot{a} > 0$ , so the universe undergoes

<sup>5</sup>Two points  $\mathcal{H}^{-1}$  apart drifts away with relative physical velocity  $v_{\text{phys}} = \dot{a}\mathcal{H}^{-1} = 1$ , which is equal to  $c$  in our units. It is difficult for such points to have causal interaction right now, especially within Hubble time  $H^{-1}$ .

accelerated expansion. Steep decrease in  $\mathcal{H}^{-1}$  is expressed using a ‘slow-roll’ parameter

$$\varepsilon := -\frac{d \ln H}{d \ln a} = -\frac{\dot{H}}{H^2} \ll 1. \quad (1.47)$$

Inflation also needs to last long enough for the particle horizon to grow sufficiently large. We define another parameter to denote this constraint;

$$\eta := \frac{d \ln \varepsilon}{d \ln a} = \frac{\dot{\varepsilon}}{\varepsilon H} \ll 1. \quad (1.48)$$

### 1.3.2 Slow-roll inflation

The simplest model of inflation consists of a single scalar field  $\phi$ . The action for a real scalar field with canonical kinetic term and potential  $V(\phi)$  is given by

$$S_\phi = \int dt d^3 \mathbf{x} \sqrt{-g} \left[ -\frac{1}{2} g^{\mu\nu} \partial_\mu \phi \partial_\nu \phi - V(\phi) \right], \quad (1.49)$$

where  $g := \det g$ . Denoting the integrand as the Lagrangian density  $\mathcal{L}[t, \mathbf{x}, \phi, \partial_\mu \phi]$ , the energy-momentum tensor can be expressed using functional derivatives as

$$T_{\mu\nu} = \frac{-2}{\sqrt{-g}} \frac{\delta \mathcal{L}}{\delta g^{\mu\nu}} = -2 \frac{\delta \mathcal{L}}{\delta g^{\mu\nu}} + g_{\mu\nu} \mathcal{L}. \quad (1.50)$$

Here, we used the identity  $\delta \sqrt{-g} = -(1/2) \sqrt{-g} g_{\mu\nu} \delta g^{\mu\nu}$ . Substituting (1.49),

$$T_{\mu\nu} = (\partial_\mu \phi) (\partial_\nu \phi) + g_{\mu\nu} \left( -\frac{1}{2} g^{\rho\sigma} \partial_\rho \phi \partial_\sigma \phi - V(\phi) \right). \quad (1.51)$$

Now suppose that  $\phi$  drives inflation in the FLRW background. Due to the symmetries present in homogeneous and isotropic metric, the inflation field can only depend on time;  $\phi(\mathbf{x}, t) = \bar{\phi}(t)$ . We can read off the inflation field’s energy density and pressure from the energy-momentum tensor.

$$\rho_{\bar{\phi}} = -T_0^0 = \frac{1}{2} \dot{\bar{\phi}}^2 + V(\bar{\phi}), \quad (1.52)$$

$$P_{\bar{\phi}} \delta_j^i = T_j^i = \delta_j^i \left( \frac{1}{2} \dot{\bar{\phi}}^2 - V(\bar{\phi}) \right). \quad (1.53)$$

The two terms  $\frac{1}{2}\dot{\bar{\phi}}^2$  and  $V(\bar{\phi})$  can be interpreted as the kinetic and potential energy of inflation field, respectively. The equation of state is also expressed in terms of the two;

$$w_{\bar{\phi}} = \frac{P_{\bar{\phi}}}{\rho_{\bar{\phi}}} = \frac{\frac{1}{2}\dot{\bar{\phi}}^2 + V(\bar{\phi})}{\frac{1}{2}\dot{\bar{\phi}}^2 - V(\bar{\phi})}. \quad (1.54)$$

It follows that  $\bar{\phi}$  satisfies the condition  $3w_{\bar{\phi}} + 1 < 0$  required for inflation, as long as the potential energy dominates over kinetic energy.

The classical equations of motion follows from the Euler-Lagrange equation. After some calculations we obtain

$$\ddot{\bar{\phi}} + 3H\dot{\bar{\phi}} = -V'(\bar{\phi}). \quad (1.55)$$

Even though  $\bar{\phi}$  is a field, its dynamics given in (1.55) are identical to those of a particle rolling down an one-dimensional potential. Its movement should be slow for the kinetic energy to be much smaller than the potential, and hence the name ‘slow-roll’ inflation.

The Friedmann equations (1.32-1.33) can now be expressed in terms of the background inflationary field.

$$H^2 = \frac{8\pi G}{3} \left( \frac{1}{2}\dot{\bar{\phi}}^2 + V(\bar{\phi}) \right) \approx \frac{8\pi G}{3} V(\bar{\phi}), \quad (1.56)$$

$$\frac{\ddot{a}}{a} = -\frac{8\pi G}{3} \left( \dot{\bar{\phi}}^2 - \frac{1}{2}V(\bar{\phi}) \right) \approx \frac{8\pi G}{3} V(\bar{\phi}), \quad (1.57)$$

where the slow-roll approximations have been used in the last step. Taking derivative of (1.56) gives us  $3H\dot{\bar{\phi}} \approx -V'$ . The parameters defined as

$$\varepsilon_V := \frac{1}{16\pi G} \left( \frac{V'}{V} \right)^2, \quad \eta_V := \frac{1}{8\pi G} \frac{V''}{V}, \quad (1.58)$$

can then shown to be small. Therefore the slow roll parameters from (1.47-1.48) satisfy

$$\varepsilon \approx \varepsilon_V \ll 1, \quad \eta \approx -2\eta_V + 4\varepsilon_V \ll 1. \quad (1.59)$$

We see that as long as the potential  $V(\phi)$  is chosen such that  $\varepsilon_V, \eta_V \ll 1$ , the field  $\phi$  can drive a period of accelerated expansion. Here,  $\bar{\phi}(t)$  acts as a clock; it measures the progress of inflation, until  $\varepsilon$  eventually grows comparable to 1 and inflation ends.

### 1.3.3 Quantum fluctuations

So far our considerations on the inflation field  $\phi$  has been entirely classical. Moving on to quantum theory, field values are no longer fixed at each point in spacetime. The goal of this section is to quantify statistical properties of these quantum fluctuations.

For simplicity, we assume that the metric remains unperturbed. In reality, gravity is coupled with perturbations of the inflation field, but this approximation still allows us to derive most of the crucial results. We further neglect any terms suppressed by slow-roll parameters.

We write the inflation field as a sum of the classical solution and perturbation;

$$\phi(\mathbf{x}, t) = \bar{\phi}(t) + \frac{v(\mathbf{x}, t)}{a(t)}, \quad (1.60)$$

where the factor of  $1/a$  has been introduced for later convenience. First rewriting the scalar field action (1.49) in terms of conformal time,

$$S_\phi = \int d\tau d^3\mathbf{x} a(\tau)^2 \left[ \frac{1}{2}(\phi')^2 - \frac{1}{2}(\nabla\phi)^2 - a(\tau)^2 V(\phi) \right]. \quad (1.61)$$

When we include perturbations, terms linear in  $v$  vanish from the equations of motion of  $\bar{\phi}$ . Further removing terms with derivatives of  $V(\phi)$  using slow-roll condition,

$$\delta S_\phi = \int d\tau d^3\mathbf{x} \left[ \frac{1}{2} \left( v' - \frac{a'}{a} v \right)^2 - \frac{1}{2} (\nabla v)^2 \right] \quad (1.62)$$

$$= \int d\tau d^3\mathbf{x} \left[ \frac{1}{2} (v')^2 + \frac{1}{2} \frac{a''}{a} v^2 - \frac{1}{2} (\nabla v)^2 \right]. \quad (1.63)$$

Integration by parts has been used to obtain the last line. The equations of motion for  $v$  follows;

$$v'' - \frac{a''}{a} v - \nabla^2 v = 0. \quad (1.64)$$

Defining Fourier transforms of  $v$  as

$$v(\mathbf{x}, \tau) = \int \frac{d^3\mathbf{k}}{(2\pi)^3} e^{i\mathbf{k}\cdot\mathbf{x}} \tilde{v}(\mathbf{k}, \tau), \quad (1.65)$$

we obtain the Mukhanov-Sasaki equation;

$$v'' + (k^2 - \frac{a''}{a})v = 0 \quad (1.66)$$

Tildes above  $v$  have been omitted for brevity. Each  $\mathbf{k}$  mode of the perturbative field  $v(\mathbf{k}, \tau)$  evolves independently from each other. During slow-roll inflation  $a \propto -1/\tau$ , and  $a''/a = 2/\tau^2$ . General form of the solution is given by the *mode functions*  $v_k(\tau)$ .

$$v_k(\tau) = c_+ \left(1 - \frac{i}{k\tau}\right) e^{-ik\tau} + c_- \left(1 + \frac{i}{k\tau}\right) e^{ik\tau}. \quad (1.67)$$

We would like to canonically quantise the field  $v(\mathbf{k}, \tau)$ . To achieve this goal, we first convert from the Lagrangian to Hamiltonian formalism.

$$\pi := \frac{\partial \mathcal{L}}{\partial v'} = v', \quad (1.68)$$

$$\mathcal{H} := v' \frac{\partial \mathcal{L}}{\partial v'} - \mathcal{L} = \frac{1}{2} \pi^2 + \frac{1}{2} (\nabla v)^2 - \frac{1}{2} \frac{a''}{a} v^2. \quad (1.69)$$

We now promote classical fields  $v(\mathbf{k}, \tau)$ ,  $\pi(\mathbf{k}, \tau)$  to operators  $\hat{v}_{\mathbf{k}}(\tau)$ ,  $\hat{\pi}_{\mathbf{k}}(\tau)$  satisfying equal-time commutation relations <sup>6</sup>

$$[\hat{v}_{\mathbf{k}_1}(\tau), \hat{\pi}_{\mathbf{k}_2}(\tau)] = (2\pi)^3 \delta^{(3)}(\mathbf{k}_1 + \mathbf{k}_2), \quad (1.70)$$

$$[\hat{v}_{\mathbf{k}_1}(\tau), \hat{v}_{\mathbf{k}_2}(\tau)] = [\hat{\pi}_{\mathbf{k}_1}(\tau), \hat{\pi}_{\mathbf{k}_2}(\tau)] = 0. \quad (1.71)$$

Defining operators  $\hat{a}_{\mathbf{k}}$  and  $\hat{a}_{\mathbf{k}}^\dagger$  appropriately, we may write

$$\hat{v}_{\mathbf{k}}(\tau) = v_k(\tau) \hat{a}_{\mathbf{k}} + v_k(\tau)^* \hat{a}_{-\mathbf{k}}^\dagger, \quad (1.72)$$

$$\hat{\pi}_{\mathbf{k}}(\tau) = v'_k(\tau) \hat{a}_{\mathbf{k}} + v'_k(\tau)^* \hat{a}_{-\mathbf{k}}^\dagger. \quad (1.73)$$

As long as we normalise the mode functions  $v_k(\tau)$  so that its Wronskian  $W := v_k v'_k{}^* - v_k^* v'_k = i$  (purely imaginary since  $v_k$  is real), we obtain

$$[\hat{v}_{\mathbf{k}_1}(\tau), \hat{\pi}_{\mathbf{k}_2}(\tau)] = i [\hat{a}_{\mathbf{k}_1}, \hat{a}_{\mathbf{k}_2}^\dagger], \quad (1.74)$$

$$[\hat{a}_{\mathbf{k}_1}, \hat{a}_{\mathbf{k}_2}^\dagger] = (2\pi)^3 \delta^{(3)}(\mathbf{k}_1 - \mathbf{k}_2). \quad (1.75)$$

---

<sup>6</sup>This follows from its Fourier equivalent:  $[\hat{v}(\mathbf{x}_1, \tau), \hat{\pi}(\mathbf{x}_2, \tau)] = i \delta^{(3)}(\mathbf{x}_1 - \mathbf{x}_2)$ .

Constructed  $\hat{a}$  and  $\hat{a}^\dagger$  are analogous to the creation and annihilation operators of quantum harmonic oscillator. Our next step is to compute the Hamiltonian operator;

$$\hat{H} = \int d^3\mathbf{x} \left[ \frac{1}{2} \hat{\pi}^2 + \frac{1}{2} (\nabla \hat{v})^2 - \frac{1}{2} \frac{a''}{a} \hat{v}^2 \right] \quad (1.76)$$

$$= \int d^3\mathbf{x} \frac{d^3\mathbf{k}_1}{(2\pi)^3} \frac{d^3\mathbf{k}_2}{(2\pi)^3} \frac{1}{2} e^{i(\mathbf{k}_1 + \mathbf{k}_2) \cdot \mathbf{x}} \left[ \hat{\pi}_{\mathbf{k}_1} \hat{\pi}_{\mathbf{k}_2} - (\mathbf{k}_1 \cdot \mathbf{k}_2) \hat{v}_{\mathbf{k}_1} \hat{v}_{\mathbf{k}_2} - \frac{a''}{a} \hat{v}_{\mathbf{k}_1} \hat{v}_{\mathbf{k}_2} \right] \quad (1.77)$$

$$= \int \frac{d^3\mathbf{k}}{(2\pi)^3} \frac{1}{2} \left[ \hat{\pi}_{\mathbf{k}} \hat{\pi}_{-\mathbf{k}} + k^2 \hat{v}_{\mathbf{k}} \hat{v}_{-\mathbf{k}} - \frac{a''}{a} \hat{v}_{\mathbf{k}} \hat{v}_{-\mathbf{k}} \right] \quad (1.78)$$

$$= \int \frac{d^3\mathbf{k}}{(2\pi)^3} \left[ E_k \left( \hat{a}_{\mathbf{k}} \hat{a}_{\mathbf{k}}^\dagger + \hat{a}_{-\mathbf{k}}^\dagger \hat{a}_{-\mathbf{k}} \right) + F_k \hat{a}_{\mathbf{k}} \hat{a}_{-\mathbf{k}} + F_k^* \hat{a}_{\mathbf{k}}^\dagger \hat{a}_{-\mathbf{k}}^\dagger \right], \quad (1.79)$$

where

$$\omega_k^2 := k^2 - \frac{a''}{a}, \quad E_k := \frac{1}{2} (|v'_k|^2 + \omega_k^2 |v_k|^2), \quad F_k := \frac{1}{2} (v_k'^2 + \omega_k^2 v_k^2). \quad (1.80)$$

Defining the vacuum state

Note that we are currently in Heisenberg picture where the operators depend on time. Our mode functions have two degrees of freedom:  $c_+$  and  $c_-$ . One of them has been fixed by the normalisation condition  $W = 2ik(|c_+|^2 - |c_-|^2) = i$ . The other degree of freedom remains, availing us one-parameter family of possible initial mode functions. Note that  $\hat{a}_{\mathbf{k}}^\dagger$  are defined in terms of  $\hat{v}_{\mathbf{k}}$  and  $\hat{\pi}_{\mathbf{k}}$ . Fixing  $\hat{a}_{\mathbf{k}}$  is thus equivalent to choosing  $\hat{v}_{\mathbf{k}}$ .

We define the vacuum  $|\mathbf{0}\rangle$  to be the state satisfying  $\hat{a}_{\mathbf{k}}|\mathbf{0}\rangle = 0$  for all  $\mathbf{k} \in \mathbb{R}^3$ . The expected energy of the vacuum state is given by

$$\langle \mathbf{0} | \hat{H} | \mathbf{0} \rangle = \int \frac{d^3\mathbf{k}}{(2\pi)^3} E_k \langle \mathbf{0} | [\hat{a}_{\mathbf{k}}, \hat{a}_{\mathbf{k}}^\dagger] | \mathbf{0} \rangle \quad (1.81)$$

$$= \int d^3\mathbf{k} E_k \delta^{(3)}(0), \quad (1.82)$$

where the divergence  $\delta^{(3)}(0)$  arises only because we are integrating over the whole space. Removing this factor, we may interpret  $E_k$  as the vacuum energy density for mode  $k$ .

We now ask the vacuum state to be a ground state of the Hamiltonian. Minimising the energy density  $E_k$  while keeping normalisation condition  $W = i$ , we obtain the *Bunch-Davies* mode function;

$$v_{\mathbf{k}}(\tau) = \frac{1}{\sqrt{2k}} \left( 1 - \frac{i}{k\tau} \right) e^{-ik\tau}. \quad (1.83)$$



For this choice of mode function and vacuum,  $E_k \rightarrow \hbar\omega_k/2$  as  $\tau \rightarrow -\infty$ .<sup>7</sup> This is analogous to the case of quantum harmonic oscillator.

Lastly, we compute the zero-point fluctuation of the inflation field. By definition,

$$\hat{v}(\mathbf{x}, \tau) = \int \frac{d^3\mathbf{k}}{(2\pi)^3} \left[ v_k \hat{a}_{\mathbf{k}} + v_k^* \hat{a}_{\mathbf{k}}^\dagger \right] e^{i\mathbf{k}\cdot\mathbf{x}}, \quad (1.84)$$

and we have

$$\langle |\hat{v}(\mathbf{x}, \tau)|^2 \rangle = \int \frac{d^3\mathbf{k}_1}{(2\pi)^3} \frac{d^3\mathbf{k}_2}{(2\pi)^3} \langle \mathbf{0} | v_{k_1} \hat{a}_{\mathbf{k}_1} v_{k_2}^* \hat{a}_{\mathbf{k}_2}^\dagger | \mathbf{0} \rangle \quad (1.85)$$

$$= \int \frac{d^3\mathbf{k}_1}{(2\pi)^3} \frac{d^3\mathbf{k}_2}{(2\pi)^3} v_{k_1} v_{k_2}^* \langle \mathbf{0} | [\hat{a}_{\mathbf{k}_1}, \hat{a}_{\mathbf{k}_2}^\dagger] | \mathbf{0} \rangle \quad (1.86)$$

$$= \int \frac{d^3\mathbf{k}}{(2\pi)^3} |v_k|^2 \quad (1.87)$$

$$= \int d(\ln k) P_v(k, \tau). \quad (1.88)$$

The dimensionless power spectrum is defined as

$$P_v(k, \tau) := \frac{k^3}{2\pi^2} |v_k(\tau)|^2. \quad (1.89)$$

Recall that perturbations in  $\phi$  is given by  $\delta\phi = v/a$  from (1.60). The *dimensionless power spectrum* for fluctuations in  $\phi$  is therefore

$$P_{\delta\phi}(k, \tau) = \frac{P_v(k, \tau)}{a(\tau)^2} = \left( \frac{H}{2\pi} \right)^2 (1 + (k\tau)^2), \quad (1.90)$$

where we used the fact that  $a(\tau) = -1/H\tau$  during slow-roll inflation. For scales larger than the comoving Hubble radius we have  $k\tau \ll 1$ . In this limit,  $P_{\delta\phi} \rightarrow (H/2\pi)^2$  which is nearly constant. This is a key prediction from our simplistic model of inflation; we expect a near scale-invariant power spectrum of perturbations.

---

<sup>7</sup> $\hbar$  has been reinstated here for clarity.



# Chapter 2

## Cosmic Microwave Background Anisotropy

- Explain recombination and CMB, without talking about detailed thermal history
- CMB perfectly follows blackbody spectrum. Borrow a figure of intensity vs wavelength from Planck
- Existence of temperature anisotropy. Maps from COBE, WMAP and Planck
- Explain goal: obtain theoretical derivations for CMB anisotropy and introduce statistical formulation for comparing with measurements.

### 2.1 The inhomogeneous universe

#### 2.1.1 Perturbation theory

- Definitions for perturbation theory
- SVT theorem, only consider scalar perturbations
- Gauge problem. use Newtonian gauge
- Perturbed Einstein equations
- Definition of  $\zeta$  and its conservation in superhorizon scales

### 2.1.2 Boltzmann Equations

- Define photon anisotropy
- Boltzmann equation and Thompson scattering cross-section (quote)
- Decomposition using multipole moments
- Briefly talk about Boltzmann hierarchy. Mention that numerical solutions gives us transfer functions, defined as  $\Delta_l(k) = \Theta_l(k, \eta_0)/\Phi(k, \eta_i)$ .

### 2.1.3 CMB anisotropy

- Late time  $a_{lm}$ s. Derive expression using transfer functions. (Written)
- Derive form for  $C_l$ 's. (Written)
- Borrow Planck 2018 analysis picture. Briefly discuss bayesian stuff.

## 2.2 Bispectrum

### 2.3 CMB Bispectrum

- Derive form for  $B$ 's. Gaunt integral, wigner 3j symbols, etc. (Written)

### 2.4 CMB polarisation

# Chapter 3

## Bispectrum and Primordial Non-Gaussianity

### 3.1 Bispectrum

Bispectrum definition. Form. Different configurations.

### 3.2 Primordial non-Gaussianity

### 3.3 CMB bispectrum estimation

Existence of non-vanishing bispectrum at the end of inflation due to primordial non-Gaussianity leaves imprints on the statistics of CMB anisotropy.

#### 3.3.1 CMB bispectrum

Consider the three-point correlation function of the spherical harmonic coefficients  $a_{lm}^X$ s from (TODO: reference alm definition here).

$$\left\langle a_{l_1 m_1}^{X_1} a_{l_2 m_2}^{X_2} a_{l_3 m_3}^{X_3} \right\rangle = (4\pi)^3 (-i)^{l_1 + l_2 + l_3} \left\langle \int \prod_{j=1}^3 \left[ \frac{d^3 \mathbf{k}_j}{(2\pi)^3} \zeta(\mathbf{k}_j) \Delta_{l_j}^{X_j}(k_j) Y_{l_j m_j}^*(\hat{\mathbf{k}}_j) \right] \right\rangle. \quad (3.1)$$

Here  $X_j$ s can be either  $T$  or  $E$ , corresponding to temperature and E-mode polarisation of CMB anisotropy. The transfer functions  $\Delta_l^X(k)$  depend only on  $k = \|\mathbf{k}\|$  and incorporates all information about the evolution of primordial perturbations  $\zeta$ .

We may take everything but  $\zeta(\mathbf{k}_j)$ s outside the brackets  $\langle \cdot \rangle$ . From the definition of bispectrum, we have

$$\langle \zeta(\mathbf{k}_1)\zeta(\mathbf{k}_2)\zeta(\mathbf{k}_3) \rangle = (2\pi)^3 \delta^{(3)}(\mathbf{k}_1 + \mathbf{k}_2 + \mathbf{k}_3) B(k_1, k_2, k_3) \quad (3.2)$$

$$= \int d^3\mathbf{r} e^{-i\mathbf{r} \cdot (\mathbf{k}_1 + \mathbf{k}_2 + \mathbf{k}_3)} B(k_1, k_2, k_3). \quad (3.3)$$

where an integral expression is substituted for the Dirac  $\delta$ -function in the second line. At the cost of introducing an extra integral, we managed to express the  $\delta$ -function in a separable form:  $\exp(\mathbf{r} \cdot (\mathbf{k}_1 + \mathbf{k}_2 + \mathbf{k}_3)) = \exp(\mathbf{r} \cdot \mathbf{k}_1) \exp(\mathbf{r} \cdot \mathbf{k}_2) \exp(\mathbf{r} \cdot \mathbf{k}_3)$ . Remaining exponentials are rewritten using the plane wave expansion;

$$e^{-i\mathbf{k} \cdot \mathbf{r}} = \sum_{l=0}^{\infty} (2l+1)(-i)^l j_l(kr) P_l(\hat{\mathbf{k}} \cdot \hat{\mathbf{r}}) \quad (3.4)$$

$$= \sum_{l=0}^{\infty} \sum_{m=-l}^l 4\pi (-i)^l j_l(kr) Y_{lm}(\hat{\mathbf{k}}) Y_{lm}^*(\hat{\mathbf{r}}). \quad (3.5)$$

Legendre polynomial  $P_l(\hat{\mathbf{k}} \cdot \hat{\mathbf{r}})$  has been expanded using the spherical harmonic addition theorem on the last line. Now  $\mathbf{k}$  and  $\mathbf{r}$  mix only through their amplitudes and spherical bessel function:  $j_l(kr)$ .

fNL form, analogy to linear regression.

Review of KSW, Modal and Binned estimators.

# Chapter 4

## CMB Stage-4 Forecast

We present forecasts on the primordial non-Gaussianity parameter  $f_{\text{NL}}$  of feature models for the future Cosmic Microwave Background Stage-4 (CMB-S4) experiments. The Fisher matrix of the bispectrum estimator was computed using noise covariances expected for preliminary CMB-S4 specifications including ones for the Simons Observatory. We introduce a novel method that improves the computation by orthonormalising the covariance matrix. The most sensitive CMB-S4 experiment with  $1'$  beam and  $1\mu K$ -arcmin noise would yield a factor of 1.7-2.2 times more stringent constraints compared to Planck. Under the Simons Observatory baseline conditions the improvement would be about 1.3-1.6 times to Planck. We also thoroughly studied the effects of various model and experimental parameters on the forecast. Detailed analysis on the constraints coming from temperature and E-mode polarisation, in particular, provided some insight into detecting oscillatory features in the CMB bispectrum.

### 4.1 Background

The Cosmic Microwave Background (CMB) radiation is one of our most valuable probes of the primordial universe. The temperature and polarisation of this ancient light contains rich statistical information both about the primordial perturbations created during inflation and also their subsequent evolution until now. This allows us to test our inflationary theories and also the history of our universe. The recent Planck CMB experiments have provided stringent tests on various models of inflation through the estimation of cosmological parameters and via primordial non-Gaussianity [48, 49].

The simplest model of inflation involves a single scalar field slowly rolling down a smooth potential. In this case the CMB temperature fluctuations are expected to be Gaussian distributed with only tiny deviations (e.g. [35]). However, many other physically well-motivated models generate larger non-Gaussian signatures at the end of inflation (see reviews

of [11]). Such primordial non-Gaussianities are well constrained by three-point correlation functions of the CMB anisotropies or their Fourier transform, the CMB bispectrum. Different inflationary models predict bispectra with different momentum dependence, or ‘shapes’. We constrain these models by using an optimal estimator for their amplitude parameter,  $f_{\text{NL}}$ , for each specific bispectrum shape (see, e.g, [30, 34] for reviews).

Although all observations to date are consistent with vanishing non-Gaussianity, the models most favoured by the latest Planck CMB analysis were the ones with oscillations in the primordial power spectrum [48]. Among them are feature models, where the oscillations are caused by a sharp feature in either the inflationary potential [53, 2, 13, 3, 26, 17], sound speed [41, 5], or multi-field potentials [1] (see [11, 14] for reviews). The primordial power spectrum then becomes scale dependent, displaying sinusoidal oscillations that are linearly spaced in momentum space. The resulting bispectrum also oscillates and is highly uncorrelated with other popular bispectrum templates [39], therefore allowing us to constrain them independently.

Planck constrained  $f_{\text{NL}}$  for feature models from CMB bispectra, but no signal above  $3\sigma$  significance were found after accounting for the ‘look elsewhere effect’ as introduced in [21]. The multi-peak statistic analysis, however, revealed some non-standard signals up to  $4\sigma$  level that deserves attention [48]. There have been many other searches on signatures of oscillations. Constraints also come from the CMB power spectrum [36, 7, 40, 37, 38, 22], the large scale structure [10, 4], and a combination of the two [27, 6]. We expect stronger constraints on feature models from future LSS experiments [12]. This paper covers the prospects of upcoming CMB experiments in constraining  $f_{\text{NL}}$  for feature models.

Currently there are two implementations of the optimal estimator for constraining  $f_{\text{NL}}$  for feature type models. The Planck analysis adopted the Modal estimator for which the given bispectrum is expanded using a separable basis [23, 20]. This method is efficient and can flexibly account for various oscillatory shapes and can easily constrain all frequencies simultaneously. However, when the oscillation frequency is large the modal basis fails to converge within reasonable number of basis elements, making the method impractical. The other approach using the Komatsu-Spergel-Wandelt (KSW) estimator is viable for various shapes including the feature model [31, 42]. Although this method only applies to models with separable bispectra, even highly oscillatory templates can reliably be computed. This method is however more expensive as each frequency must be dealt with separately. We present further optimisations to the fast KSW estimator introduced in [56] and apply it on feature models for forecasts in this paper.

The next generation of CMB experiments, CMB Stage-4, consists of many exciting proposed experiments located at the South Pole, the Atacama Desert in Chile, and perhaps



space [18, 55, 54]. One of the main goals of these experiments is to measure the polarisation signal in the CMB to the cosmic variance limit. Preliminary specifications have been released for these experiments [18, 55] and these have been used to produce some forecasts for the standard  $f_{NL}$  templates but not yet for feature type models. In this paper we address this by presenting the Fisher forecasts on  $f_{NL}$  for feature models based on these specifications and observe that feature type models receive larger improvements from the extra polarisation information than the standard templates justifying this analysis.

The paper is organised as follows. First we briefly review the theory of CMB bispectrum in Section 4.2. Bispectrum template for the feature model is defined and computed here. In Section 4.3 we formulate the bispectrum estimator and introduce a new method to further optimise its computation. The technique is applied to the case of feature model to yield equations for the Fisher forecast of  $f_{NL}$ . We also briefly discuss implementation details. In Section 4.4 we present our forecast results and their dependence on model and experimental parameters. In particular, forecasts for the Simons observatory are compared with the Planck results. The results are summarised in Section 4.5.

## 4.2 Feature model bispectrum

### 4.2.1 CMB bispectrum

One of the main subjects of primordial NG studies is the 3-point correlation function of the primordial perturbations which is defined by;

$$\langle \Phi(\mathbf{k}_1)\Phi(\mathbf{k}_2)\Phi(\mathbf{k}_3) \rangle = (2\pi)^3 \delta^{(3)}(\mathbf{k}_1 + \mathbf{k}_2 + \mathbf{k}_3) B_\Phi(k_1, k_2, k_3), \quad (4.1)$$

where we have assumed statistical homogeneity and isotropy. The primordial bispectrum  $B_\Phi$  vanishes for Gaussian perturbations, but more general inflation models predict non-zero bispectra with various shapes. In order to constrain these models we re-parameterise the bispectrum into an amplitude parameter and a normalised shape part;

$$B_\Phi(k_1, k_2, k_3) = f_{NL} B_\Phi^{(f_{NL}=1)}(k_1, k_2, k_3). \quad (4.2)$$

Constraining  $f_{NL}$  from the CMB measurements allows to determine how well the particular shape under consideration aligns with the data which we can translate into constraints on the model itself.

In order to compare the theory with measurements we first need to relate the primordial perturbations to spherical multipole modes of the late-time CMB anisotropies.

$$a_{lm}^X = 4\pi(-i)^l \int \frac{d^3\mathbf{k}}{(2\pi)^3} \Phi(\mathbf{k}) \Delta_l^X(k) Y_{lm}(\hat{\mathbf{k}}). \quad (4.3)$$

Here the index  $X$  is either  $T$  or  $E$ , representing CMB temperature and E-mode polarisation, respectively. The linear CMB radiation transfer function  $\Delta_l^X(k)$  can be computed from the Boltzmann solvers like CAMB [33].

Three point correlation function of  $a_{lm}^X$ 's yield the reduced bispectrum  $b_{l_1 l_2 l_3}$  times a geometrical factor  $\mathcal{G}_{m_1 m_2 m_3}^{l_1 l_2 l_3}$  named the Gaunt integral. After some algebraic manipulations we obtain the following useful formula for the reduced bispectrum;

$$b_{l_1 l_2 l_3}^{X_1 X_2 X_3} = \left(\frac{2}{\pi}\right)^3 \int_0^\infty r^2 dr \int_{\gamma_k} d^3\mathbf{k} (k_1 k_2 k_3)^2 B_\Phi(k_1, k_2, k_3) \prod_{i=1}^3 \left[ j_{l_i}(k_i r) \Delta_{l_i}^{X_i}(k_i) \right], \quad (4.4)$$

where  $j_l$  is the spherical Bessel function arising from the Rayleigh expansion formula. Using this equation, we can compute the projected bispectrum from any given primordial bispectrum. Direct computation of this four-dimensional integral for every  $l$  combination, however, is practically impossible. Not only is the integral in 4D but also the oscillatory integrand requires a large number of sample points in each of  $k_i$ , making the full calculation for every  $l_i$  triple prohibitively expensive. All bispectrum estimators get around this problem by expanding  $B_\Phi$  as a sum of *separable* terms. This will be explained in more detail later using the feature model template as an example.

## 4.2.2 Feature model

We follow the works of [42, 21, 22, 48] and assume the following template for the bispectrum of feature models;

$$B_\Phi^{\text{feat}}(k_1, k_2, k_3) = \frac{6A^2}{(k_1 k_2 k_3)^2} \sin(\omega K + \phi), \quad (4.5)$$

where  $K = k_1 + k_2 + k_3$ ,  $A$  represents the primordial power spectrum amplitude, and  $\phi$  is a phase. The oscillation ‘frequency’  $\omega$  is associated with the location and scale of feature in the inflationary potential. It is often written in terms of the oscillation scale  $k_c$  as  $\omega = 2\pi/3k_c$ .  $\omega$  is measured in Mpc but we omit the unit for notational conveniences.

The feature model template has two free parameters that need to be fixed before we can constrain the model: the frequency  $\omega$  and phase  $\phi$ . The phase can be easily dealt with from

observing that

$$B_{\Phi}^{\text{feat}}(k_1, k_2, k_3) = \cos \phi B_{\Phi}^{\text{sin}}(k_1, k_2, k_3) + \sin \phi B_{\Phi}^{\text{cos}}(k_1, k_2, k_3). \quad (4.6)$$

Here  $B_{\Phi}^{\text{sin}}$  and  $B_{\Phi}^{\text{cos}}$  correspond to feature models with  $\phi = 0, \pi/2$  respectively. Non-zero phase simply corresponds to a linear combination of the sine and cosine templates. As we will see later these two shapes are in fact highly uncorrelated, and therefore they can be constrained independently from each other.

On the other hand, one still has a complete freedom of choice on the oscillation frequency. Such freedom dramatically expands size of the parameter space. In practice we constrain  $f_{\text{NL}}$  for each fixed value of oscillation frequency, which yields hundreds of estimates. Since there are so many estimates we are looking at, there is a good chance that we find notable signals by sheer luck. Accounting for this ‘look elsewhere effect’ has been resolved using methods in [21] and subsequently applied to the Planck analysis [48, 22]. The look-elsewhere-adjusted statistics used in the literature can be employed for the future CMB-S4 data analysis. This work, however, focuses on forecasting the ‘raw’ estimates and comparing them with those of Planck.

### 4.2.3 Separability

The bispectrum template of feature models (4.5) is an example of separable shape. It can be expressed as a sum of terms in the form  $f(k_1)g(k_2)h(k_3)$  for some functions  $f$ ,  $g$  and  $h$ , dramatically simplifying the computation of reduced bispectrum  $b_{l_1 l_2 l_3}$ . The three-dimensional integral over the  $k$  space in (4.4) splits into three individual one-dimensional integrals for separable shapes. Feature models for example has

$$\begin{aligned} b_{l_1 l_2 l_3}^{X_1 X_2 X_3, \text{feat}} &= 6A^2 \left(\frac{2}{\pi}\right)^3 \int_0^\infty r^2 dr \int_{\gamma_k} d^3 \mathbf{k} e^{i\omega(k_1+k_2+k_3)} \prod_{i=1}^3 \left[ j_{l_i}(k_i r) \Delta_{l_i}^{X_i}(k_i) \right] \\ &= 6A^2 \left(\frac{2}{\pi}\right)^3 \int_0^\infty r^2 dr \prod_{i=1}^3 \left[ \int_0^\infty dk_i e^{i\omega k_i} j_{l_i}(k_i r) \Delta_{l_i}^{X_i}(k_i) \right]. \end{aligned} \quad (4.7)$$

Here the real and imaginary parts of  $b^{\text{feat}}$  correspond to the bispectra of cosine and sine feature models, respectively. Now define

$$s_l^X(r) := \frac{2A^{2/3}}{\pi} \int_0^\infty dk \sin(\omega k) j_l(kr) \Delta_l^X(k) \quad (4.8)$$

$$c_l^X(r) := \frac{2A^{2/3}}{\pi} \int_0^\infty dk \cos(\omega k) j_l(kr) \Delta_l^X(k). \quad (4.9)$$

These are analogous to  $\alpha_i^X(r)$  and  $\beta_i^X(r)$  in the usual Komatsu-Spergel-Wandelt (KSW) estimator for local non-Gaussianity. Then (4.7) reduces to

$$\begin{aligned} b_{l_1 l_2 l_3}^{X_1 X_2 X_3, \text{feat}} &= 6 \int_0^\infty r^2 dr \left( c_{l_1}^{X_1} c_{l_2}^{X_2} c_{l_3}^{X_3} - c_{l_1}^{X_1} s_{l_2}^{X_2} s_{l_3}^{X_3} - s_{l_1}^{X_1} c_{l_2}^{X_2} s_{l_3}^{X_3} - s_{l_1}^{X_1} s_{l_2}^{X_2} c_{l_3}^{X_3} \right) \\ &\quad + 6i \int_0^\infty r^2 dr \left( s_{l_1}^{X_1} c_{l_2}^{X_2} c_{l_3}^{X_3} + c_{l_1}^{X_1} s_{l_2}^{X_2} c_{l_3}^{X_3} + c_{l_1}^{X_1} c_{l_2}^{X_2} s_{l_3}^{X_3} - s_{l_1}^{X_1} s_{l_2}^{X_2} s_{l_3}^{X_3} \right). \\ &= b_{l_1 l_2 l_3}^{X_1 X_2 X_3, \cos} + i b_{l_1 l_2 l_3}^{X_1 X_2 X_3, \sin} \end{aligned} \quad (4.10)$$

## 4.3 Efficient computation of the estimator with polarisation

### 4.3.1 Estimator

The optimal estimator for a given bispectrum in the weak non-Gaussian limit is [31, 30];

$$\begin{aligned} S_i = \frac{1}{6} \sum_{l_j, m_j} \sum_{X_j} \mathcal{G}_{m_1 m_2 m_3}^{l_1 l_2 l_3} b_{l_1 l_2 l_3}^{X_1 X_2 X_3, (i)} (C_{l_1 m_1, l_4 m_4}^{-1})^{X_1 X_4} (C_{l_2 m_2, l_5 m_5}^{-1})^{X_2 X_5} (C_{l_3 m_3, l_6 m_6}^{-1})^{X_3 X_6} \\ \left[ a_{l_4 m_4}^{X_4} a_{l_5 m_5}^{X_5} a_{l_6 m_6}^{X_6} - \left( C_{l_4 m_4, l_5 m_5} a_{l_6 m_6}^{X_6} + 2 \text{ cyclic} \right) \right]. \end{aligned} \quad (4.11)$$

Computing this form involves an inversion of the full covariance matrix which is very computationally expensive. As a result we will follow the diagonal covariance approximation in [56] for the inverse covariances, so  $C_{l_1 l_4 m_1 m_4}^{-1} \approx 1/C_{l_1} \delta_{l_1 l_4}^D \delta_{m_1 - m_4}^D$ ; and approximate the covariance in the linear term by an ensemble average of realistic simulations  $C_{l_4 l_5 m_4 m_5}^{X_1 X_2} \approx \langle a_{l_1 m_1}^{X_1} a_{l_2 m_2}^{X_2} \rangle$ . With these the estimator takes the form;

$$\hat{f}_i = \sum_j (F^{-1})_{ij} S_j, \quad (4.12)$$

where

$$\begin{aligned} S_i = \frac{1}{6} \sum_{l_j, m_j} \sum_{X_j, X'_j} \mathcal{G}_{m_1 m_2 m_3}^{l_1 l_2 l_3} b_{l_1 l_2 l_3}^{X_1 X_2 X_3, (i)} (C_{l_1}^{-1})^{X_1 X'_1} (C_{l_2}^{-1})^{X_2 X'_2} (C_{l_3}^{-1})^{X_3 X'_3} \\ \left[ a_{l_1 m_1}^{X'_1} a_{l_2 m_2}^{X'_2} a_{l_3 m_3}^{X'_3} - \left( \langle a_{l_1 m_1}^{X'_1} a_{l_2 m_2}^{X'_2} \rangle a_{l_3 m_3}^{X'_3} + 2 \text{ cyclic} \right) \right]. \end{aligned} \quad (4.13)$$

Here summations are over  $l_j$ ,  $m_j$ ,  $X_j$  and  $X'_j$  for each  $j = 1, 2, 3$ . The spherical multipole moments  $a_{lm}^X$ 's are computed from either observations or simulations. The covariance matrix

$C_l$  is a  $2 \times 2$  matrix consisting of values  $C_l^{TT}$ ,  $C_l^{TE}$ ,  $C_l^{ET}$  and  $C_l^{EE}$ .<sup>1</sup> The linear terms (the second in square brackets) are required to account for anisotropies induced by masking and anisotropic noise. The bracket  $\langle \cdot \rangle$  denotes averaging over Monte Carlo simulations of Gaussian realisations.

The Fisher matrix of the estimator is given by

$$F_{ij} = \frac{f_{\text{sky}}}{6} \sum_{\text{all } X, X'} \sum_{\text{all } l} h_{l_1 l_2 l_3}^2 b_{l_1 l_2 l_3}^{X_1 X_2 X_3, (i)} (C_{l_1}^{-1})^{X_1 X'_1} (C_{l_2}^{-1})^{X_2 X'_2} (C_{l_3}^{-1})^{X_3 X'_3} b_{l_1 l_2 l_3}^{X'_1 X'_2 X'_3, (j)}. \quad (4.14)$$

Here  $f_{\text{sky}}$  denotes the fraction of the sky covered by the experiment, and  $h_{l_1 l_2 l_3}^2 := \sum_{m_j} \left( \mathcal{G}_{m_1 m_2 m_3}^{l_1 l_2 l_3} \right)^2$ . Since the estimator  $\hat{f}_i$  in (4.12) is nearly optimal, its 68% confidence ( $1\sigma$ ) interval can be computed from the Fisher matrix as  $\sigma_i := \Delta f_{NL}^{(i)} = (F^{-1})_{ii}$ .

Note that most CMB-S4 experiments are ground-based, so they can probe smaller fraction of the sky compared to Planck. Having a smaller fraction of the sky leads to increased uncertainties for the estimator. Current estimate is that the new experiments will cover 40% of the sky, significantly less than the 74% of Planck. The error bars will thus increase by a factor of 1.38 from the decrease in  $f_{\text{sky}}$  alone. This will can be reduced by combining Planck data for unobserved pixels in these experiments

### 4.3.2 Orthonormalising the covariance matrix

In [20] it was noted that orthogonalising the multipoles of temperature and polarisation maps dramatically reduces the number of terms in computation of the Modal estimators. This technique can also be applied to KSW estimators, or indeed any optimal bispectrum estimator, which is yet to be done to the authors' knowledge.

In both (4.13) and (4.14) there are summations over indices  $X$  and  $X'$  to account for correlations between the CMB temperature and E-mode polarisation. This can be simplified by essentially making a change of basis in  $X$  space for each  $l$  so that every  $C_l$  becomes orthonormal. Perform a Cholesky decomposition on  $C_l$  and invert the matrix. Then  $C_l^{-1} = L_l^T L_l$ , where  $L_l$  is a lower triangular matrix given by

$$L_l = \begin{pmatrix} \frac{1}{\sqrt{C_l^{TT}}} & 0 \\ -\frac{C_l^{TE}}{\sqrt{C_l^{TT}}} & \frac{C_l^{TT}}{\sqrt{C_l^{TT} C_l^{EE} - C_l^{TE2}}} \end{pmatrix} \quad (4.15)$$

<sup>1</sup>Note that this is equivalent to having a  $2l \times 2l$  matrix with diagonal  $l \times l$  block matrices  $C^{TT}$ ,  $C^{TE}$ ,  $C^{ET}$  and  $C^{EE}$  as in other literatures including [20].

Now let

$$\tilde{\Delta}_l^X(k) = \sum_{X'} L_l^{XX'} \Delta_l^{X'}(k), \quad \text{and} \quad \tilde{a}_{lm}^X = \sum_{X'} L_l^{XX'} a_{lm}^{X'}. \quad (4.16)$$

When  $a_{lm}$ 's are generated from simulations, the second transformation is not required as long as the new transfer function  $\tilde{\Delta}_l^X$  is used in the process.

Defining  $\tilde{b}_{l_1 l_2 l_3}$  to be the corresponding reduced bispectrum, (4.13) and (4.14) simplify to

$$S_i = \frac{1}{6} \sum_{l_j, m_j} \sum_{X_j} \mathcal{G}_{m_1 m_2 m_3}^{l_1 l_2 l_3} \tilde{b}_{l_1 l_2 l_3}^{X_1 X_2 X_3, (i)} \left[ \tilde{a}_{l_1 m_1}^{X_1} \tilde{a}_{l_2 m_2}^{X_2} \tilde{a}_{l_3 m_3}^{X_3} - \left( \langle \tilde{a}_{l_1 m_1}^{X_1} \tilde{a}_{l_2 m_2}^{X_2} \rangle \tilde{a}_{l_3 m_3}^{X_3} + 2 \text{ cyclic} \right) \right] \quad (4.17)$$

$$F_{ij} = \frac{f_{\text{sky}}}{6} \sum_{\text{all } X} \sum_{\text{all } l} h_{l_1 l_2 l_3}^2 \tilde{b}_{l_1 l_2 l_3}^{X_1 X_2 X_3, (i)} \tilde{b}_{l_1 l_2 l_3}^{X_1 X_2 X_3, (j)}. \quad (4.18)$$

Using this method not only is mathematically concise, but also halves the number of terms involved in the summation. Linear transformations (4.16) only need to be done once in the beginning of the program and cost little compared to the main computation. We also found it easier to optimise the code using instruction level vectorisations after this simplification.

The only downside of this method is that we no longer can get breakdowns of signal from each of  $TTT$ ,  $TTE$ ,  $TEE$  and  $EEE$  bispectrum since our new modes are linear combinations of  $T$  and  $E$  modes. However in most cases we are interested in either  $T$ -only or  $T + E$  results, and this method works perfectly well in these cases.

### 4.3.3 Estimator for feature models

We apply general estimator to the case of feature models. The method is similar to the one seen in [42] except that now the polarisation is included and the covariance matrices are trivial thanks to the orthonormalisation process outlined above.

Consider the bispectrum shape of

$$B_\Phi(k_1, k_2, k_3) = f_{NL}^{\text{sin}} B^{\text{sin}}(k_1, k_2, k_3) + f_{NL}^{\text{cos}} B^{\text{cos}}(k_1, k_2, k_3), \quad (4.19)$$

for a fixed value of oscillation frequency  $\omega$ . Here  $B^{\text{sin}}$  and  $B^{\text{cos}}$  correspond to reduced bispectra  $b^{\text{sin}}$  and  $b^{\text{cos}}$  defined in (4.10). The Fisher matrix  $F$  is  $2 \times 2$  but its off-diagonal entries are 2-3 orders of magnitude smaller than diagonal ones in most cases as will be presented in the next section. Thus, the two shapes are assumed to be uncorrelated and constrained individually. Here we present detailed computations for  $f_{NL}^{\text{sin}}$  only but the cosine one can be computed similarly.

From (4.10) and the definition of Gaunt integral  $\mathcal{G}_{m_1 m_2 m_3}^{l_1 l_2 l_3} = \int d\hat{\mathbf{n}} Y_{l_1 m_1}(\hat{\mathbf{n}}) Y_{l_2 m_2}(\hat{\mathbf{n}}) Y_{l_3 m_3}(\hat{\mathbf{n}})$  it follows that

$$S^{\text{cub}} = \int_0^\infty r^2 dr \int d^2 \hat{\mathbf{n}} [-M_s^3 + 3M_s M_c^2] \quad \text{and} \quad (4.20)$$

$$S^{\text{lin}} = -3 \int_0^\infty r^2 dr \int d^2 \hat{\mathbf{n}} [-M_s \langle M_s^2 \rangle + M_s \langle M_c^2 \rangle + 2M_c \langle M_s M_c \rangle], \quad (4.21)$$

where

$$\begin{aligned} M_s(r, \hat{\mathbf{n}}) &= \sum_X \sum_{lm} \tilde{s}_l^X(r) \tilde{a}_{lm}^X Y_{lm}(\hat{\mathbf{n}}), \\ M_c(r, \hat{\mathbf{n}}) &= \sum_X \sum_{lm} \tilde{c}_l^X(r) \tilde{a}_{lm}^X Y_{lm}(\hat{\mathbf{n}}). \end{aligned} \quad (4.22)$$

The sum of  $S^{\text{cub}}$  and  $S^{\text{lin}}$  gives the final value of  $S$  for sine feature model.

For efficient Fisher matrix calculation we follow [52] and deploy the identity

$$h_{l_1 l_2 l_3}^2 = \frac{(2l_1 + 1)(2l_2 + 1)(2l_3 + 1)}{8\pi} \int_{-1}^1 d\mu P_{l_1}(\mu) P_{l_2}(\mu) P_{l_3}(\mu), \quad (4.23)$$

where  $P_l(\mu)$  represents the Legendre polynomial. Then,

$$F = \frac{3}{4\pi} \int r^2 dr \int r'^2 dr' \int d\mu [P_{ss}^3 + 3P_{ss}P_{cc}^2 - 3P_{cs}^2P_{ss} - 3P_{sc}^2P_{ss} + 6P_{cs}P_{sc}P_{cc}]. \quad (4.24)$$

where we have defined

$$\begin{aligned} P_{ss}(r, r', \mu) &:= \sum_X \sum_l (2l + 1) \tilde{s}_l^X(r) \tilde{s}_l^X(r') P_l(\mu) \\ P_{sc}(r, r', \mu) &:= \sum_X \sum_l (2l + 1) \tilde{s}_l^X(r) \tilde{c}_l^X(r') P_l(\mu). \end{aligned} \quad (4.25)$$

and similarly  $P_{cs}$  and  $P_{cc}$ .

Calculation of (4.22) and (4.25) are two of the most computationally expensive steps. If we did not orthonormalise the covariance matrix, there would be extra summations over  $X'$  and some  $2 \times 2$  matrix computations involving  $(C_l^{-1})^{XX'}$  in these steps.

#### 4.3.4 Probing beam and instrumental noise

In an ideal experiment where measurements are made on each point of the sky perfectly, the covariance matrices  $C_l^{XX'}$  in (4.13) and (4.14) consists purely of the signal. In reality, however, the probing beam has finite width and the sensors are noisy. These effects can be

incorporated by modifying the covariance matrices and bispectra as follows.

$$C_l^{X_1 X_2} \rightarrow W_l^{X_1} W_l^{X_2} C_l^{X_1 X_2} + N_l^{X_1 X_2}, \quad b_{l_1 l_2 l_3}^{X_1 X_2 X_3} \rightarrow W_{l_1}^{X_1} W_{l_2}^{X_2} W_{l_3}^{X_3} b_{l_1 l_2 l_3}^{X_1 X_2 X_3}, \quad (4.26)$$

where  $W_l^X$  and  $N_l^{X_1 X_2}$  represent the beam window function and the noise covariance matrix, respectively. When substituted into KSW estimator, these changes are equivalent to modifying

$$\begin{aligned} C_l^{X_1 X_2} &\rightarrow C_l^{X_1 X_2} + \left(W_l^{X_1} W_l^{X_2}\right)^{-1} N_l^{X_1 X_2} \\ &= (C_l^{\text{sig}})^{X_1 X_2} + (C_l^{\text{noise}})^{X_1 X_2}, \end{aligned} \quad (4.27)$$

while keeping the bispectra same. Here we have defined the effective (beam-corrected) noise covariance matrix  $C_l^{\text{noise}}$ . Modes for which  $C_l^{\text{noise}}$  is much larger than  $C_l^{\text{sig}}$  contribute little to the  $f_{NL}$  estimator.

For forecasting purposes we assume Gaussian beam and white uncorrelated noise until more detailed experiment specifications become available. Under these assumptions, the effective noise covariances reduce to [43]

$$C_l^{\text{noise}, TT} = \exp(l(l+1)\sigma_{\text{beam}}^2) N_{\text{white}}, \quad C_l^{\text{noise}, EE} = 2 C_l^{\text{noise}, TT}, \quad C_l^{\text{noise}, TE} = 0. \quad (4.28)$$

The factor of two for  $EE$  mode is comes from measuring two Stokes parameters  $Q$  and  $U$ . The Gaussian beam profile is usually specified by its FWHM (full width at half maximum) in  $\text{arcmin}$ , which is then converted to standard deviations in radians for  $\sigma_{\text{beam}}$ . The noise level often comes in the units of  $\mu K \cdot \text{arcmin}$ . This is then divided by  $T_{\text{CMB}} = 2.725 K$ , converted to radians and squared to get  $N_{\text{white}}$ .

For the Planck experiment, using 5 arcmin FWHM beam and the  $47 \mu K \cdot \text{arcmin}$  noise level gives good approximations to the post-component-separation noise covariances. For CMB-S4 experiments the details are not confirmed, but the beam FWHM is expected to lie between 1-5 arcmin, while the noise level will range from 1 to  $9 \mu K \cdot \text{arcmin}$ . [18]

In real measurements there exist extra contaminations in large angular scales due to  $1/f$  noises and the component separation process. Though most of our analysis assumes simpler form of noise covariances elaborated above, for the Simons Observatory forecasts we follow [55] and model  $1/f$  noise as  $N_l = N_{\text{red}}(l/l_{\text{knee}})^{\alpha_{\text{knee}}} + N_{\text{white}}$ . The noise curves from each channel were then put together using the inverse variance method. This is a good approximation for the E mode polarisation but not for temperature, since extra degradations occur during the component separation process. Still, because dominant contributions to the feature model signal comes from polarisation data, this would be a reasonable approximation



for our forecast. For Planck the full post-component-separation noise curves are available and hence used for computations.

### 4.3.5 Implementation and validation

We implemented the pipeline outlined above using the C programming language and parallelised using hybrid MPI + openMP. The code was then run in the COSMOS super-computing system.

The transfer functions are generated from the CAMB code [33]. Bessel function values were pre-computed using recursion relations and stored in a file, while the Legendre function values were computed on the fly using the GNU scientific library. The angular power spectrum data was generated from  $\Lambda$ CDM parameters estimated in the Planck 2015 results.

Numerical integration for variables  $k$ ,  $r$  and  $r'$  were done using simple trapezoidal methods, as they can be easily vectorised for optimisation. On the other hand, integration of  $\mu$  required more care because the Legendre polynomials are highly oscillatory. We adopted the Gauss-Legendre quadrature rule with  $1.5l_{\text{max}} + 1$  points which can integrate polynomials up to order  $3l_{\text{max}}$  exactly. The weights and nodes were computed in the beginning using the QUADPTS code [25].

Various checks have been done to ensure that the code runs correctly. First we used the code to reproduce the Planck results, which agreed within 3% error. The code was then used to compute bispectrum for the constant model, corresponding to the case where  $\omega = \phi = 0$ . There exists an approximate analytic form in this case [23] which we were able to reproduce accurately. We also performed convergence tests on  $r$  and  $r'$  integration by doubling the number of points for each of them. The grid was chosen to be very dense around recombination and quite dense near reionisation. We confirmed that changes in the integral are less than 0.5% for each value of  $\omega$ .

## 4.4 CMB-S4 forecast results

### 4.4.1 Phase dependence

We now present the CMB-S4 forecast on the error bars of primordial non-Gaussianity parameter for feature models. For notational convenience we denote the error bars for sine and cosine feature models by  $\sigma_{\text{sin}}$  and  $\sigma_{\text{cos}}$ . Superscripts  $T$  and  $T + E$  are also put to distinguish temperature-only analysis from the full polarisation ones.

First of all, we check that the sine and cosine bispectrum templates defined in 4.7 are indeed uncorrelated and can be constrained separately. Equivalently, we can see if the Fisher

matrix of feature models is robust to changes in the phase for different  $\omega$  values of interest. Feature model bispectra with a specific phase  $\phi$  can be represented as a sum of sine and cosine ones as in (4.6). Hence, its Fisher matrix is given by

$$F(\omega, \phi) = \cos^2 \phi F_{ss}(\omega) + \sin^2 \phi F_{cc}(\omega) + 2 \cos \phi \sin \phi F_{sc}(\omega), \quad (4.29)$$

where  $F_{ss}$  is the element  $F_{ij}$  of the Fisher matrix in (4.14) with reduced bispectra  $b^{(i)} = b^{(j)} = b^{\sin}$ , and so on. Correlation between sine and cosine templates can be expressed as  $F_{sc}/(F_{ss}F_{cc})^{1/2}$ , and this value can be learned from analysing the  $\phi$  dependence of  $F(\omega, \phi)$ .

Figure 4.1 shows forecast error bars for the full phase range  $[0, \pi]$  in the most sensitive experiment specification of  $1'$  beam and  $1\mu K \cdot \text{arcmin}$  noise. The forecast  $\sigma$  varies within 1% level for every  $\omega \geq 20$ . In terms of the Fisher matrix, the cross term  $F_{sc}$  was 2-3 orders of magnitude smaller than  $F_{ss}$  and  $F_{cc}$  for all cases. In other words, correlation between the sine and cosine templates was smaller than 1%. This justifies our previous choice of constraining  $f_{NL}^{\sin}$  and  $f_{NL}^{\cos}$  separately. We now focus our attention to  $\sigma_{\sin}$  in future discussions.

For smaller values of  $\omega$ , the phase affects the error bar primarily through modulating the amplitude of the acoustic oscillations of the CMB itself. The radiation transfer functions are non-zero for  $k$  values in  $0 - 0.8 \text{ Mpc}^{-1}$ . The argument  $\omega k$  covers less than two full periods in this  $k$  range if  $\omega \leq 10 \text{ Mpc}$ , and phase has direct influence on the amplitude of the acoustic peaks. In the extreme case of  $\omega = 0$ , bispectrum vanishes completely for the sin feature model. Variations in the overall bispectrum amplitude therefore result in varying Fisher information for low frequencies.

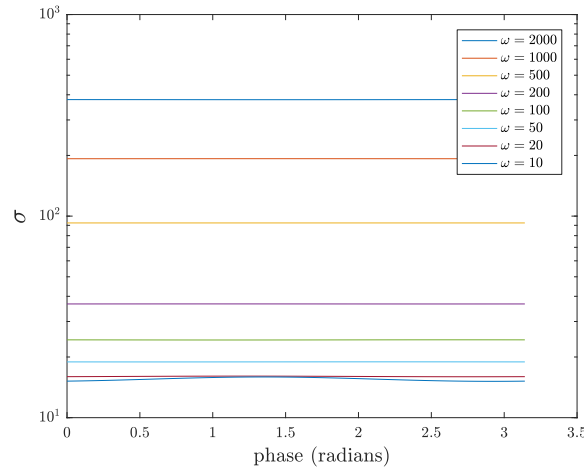


Fig. 4.1 Forecast error bars  $\sigma^{T+E}$  versus the phase  $\phi$ . Apart from the smallest frequency  $\omega = 10$ , the error bar remains almost constant. This implies that the sine ( $\phi = 0$ ) and cosine ( $\phi = \pi/2$ ) feature models can be constrained independently.

#### 4.4.2 $l_{max}$ dependence

Figure 4.2 shows the graph of forecast error bar  $\sigma_{\sin}^{T+E}$  as we increase  $l_{max}$ . The forecasts were done within angular scale range  $2 \leq l \leq l_{max}$ , the oscillation frequency  $\omega$  set to 100, and assuming 1' beam and  $1\mu K \cdot \text{arcmin}$  noise. The Planck noise curves were approximated by ones for 5' beam and  $47\mu K \cdot \text{arcmin}$  noise for this plot only, since we extend  $l_{max}$  to 4000 here.

The Planck error bar essentially stalls out when  $l_{max}$  reaches 2000. The forecast error bar, on the other hand, keeps decreasing until  $l_{max} = 4000$  thanks to the improved sensitivity in measuring small scales (and large  $l$ 's). Despite the information loss due to smaller sky coverage  $f_{sky}$ , the forecast error bar reduces to about 42% of Planck by  $l_{max} = 4000$ . This corresponds to a factor of 2.4 times improvement to measurement precision on  $f_{NL}$ .

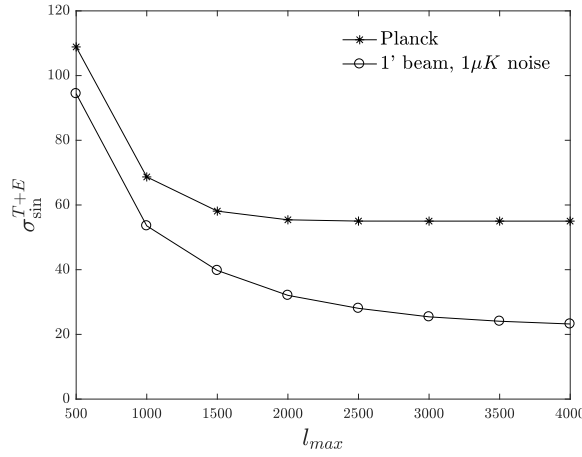


Fig. 4.2 Forecast error bars  $\sigma_{\sin}^{T+E}$  when multipoles  $2 \leq l \leq l_{max}$  are included, in comparison with Planck. The oscillation frequency  $\omega$  is set to 100 Mpc in all cases. Planck did not have access to the information from modes  $l \geq 2000$ , but the CMB-S4 experiments are expected to be able to explore modes up to  $l = 4000$ .

#### 4.4.3 Beam and noise dependence

Now we explore the effects of different beam width and noise levels on the forecast error bars. Figure 4.3 shows forecast  $\sigma_{\sin}^{T+E}$  for ranges of beam and noise levels. Their oscillation frequencies are also varied, but only two representatives  $\omega = 20$  and 2000 are chosen here. Forecasts for the other values of  $\omega$  also display similar dependences on beam width and noise levels.

First of all, note that all estimated error bars in the plot are smaller than Planck, for which  $\sigma_{\sin}^{T+E} = 34$  when  $\omega = 20$  and  $\sigma_{\sin}^{T+E} = 610$  when  $\omega = 2000$ . In fact even the least sensitive

CMB-S4 specification of 5' beam and  $9\mu K \cdot \text{arcmin}$  noise is expected to put better bounds on feature models.

Wider beams and noisier detectors provide less signal and thus larger error bars, as expected. In this range of beam width and noise levels, noise has a bigger effect on the forecast; experiments with 1' beam and  $5\mu K \cdot \text{arcmin}$  noise yields larger error bars than the ones with 5' beam with  $1\mu K \cdot \text{arcmin}$  noise. Between the most sensitive specification of 1' beam and  $1\mu K \cdot \text{arcmin}$  and the least sensitive one with 5' beam and  $9\mu K \cdot \text{arcmin}$ ,  $\sigma_{\text{sin}}$  differs by a factor of 1.6.

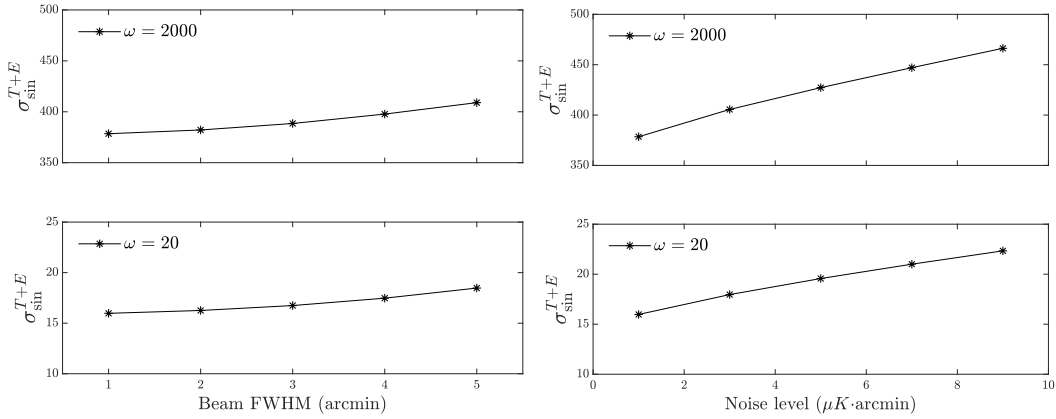


Fig. 4.3 Beam (left) and noise (right) dependences of the forecast error  $\sigma_{\text{sin}}^{T+E}$  for  $\omega = 2000$  (top) and  $\omega = 20$  (bottom). The noise level was set as  $1\mu K \cdot \text{arcmin}$  for the first plot, while the second plot had fixed beam FWHM of 1'. We obtain less information from using wider beam and noisier sensors, as expected.

#### 4.4.4 Oscillation frequency dependence

We present the main results of the forecast. Figure 4.4 summarises the  $\sigma_{\text{sin}}$  forecasts for several different CMB-S4 preliminary specifications, including the Simons Observatory (SO) baseline and goal. Note that the  $1/f$  noise effects are incorporated in SO forecasts but not in other ones. We also provide  $1\sigma$  errors for joint estimators, for which Planck signals from the fraction of the sky not covered by CMB-S4 are combined via  $\sigma_{\text{joint}}^{-2} = \sigma_{\text{CMB-S4}}^{-2} + \sigma_{\text{Planck}}^{-2}$ . This method is not statistically optimal but sufficient to give an idea of the joint estimation power.

The most sensitive setup with 1' beam and  $1\mu K \cdot \text{arcmin}$  noise would yield error bars that are 47-62% of Planck. These correspond to a factor of 1.6-2.1 improvements. Here relatively smaller improvements are made for high oscillation frequencies. They correspond to smaller momentum scales  $k_* = 2\pi/3\omega$ , or larger angular scales, which benefit less from

the increased sensitivity of CMB-S4 experiments. When the results are combined with Planck, the error bar reduces to 45-57% of Planck, or a factor of 1.7-2.2 improvement.

Forecast error bars from the SO baseline specification and the more ambitious one do not differ very much. Quoting in terms of the baseline values,  $\sigma_{\text{sin}}$  lies about 68-86% of that of Planck or equivalently, 1.2-1.5 times smaller than Planck. Numbers change to 62-74% when combined with Planck, so that the overall improvement ratio is about 1.3-1.6.

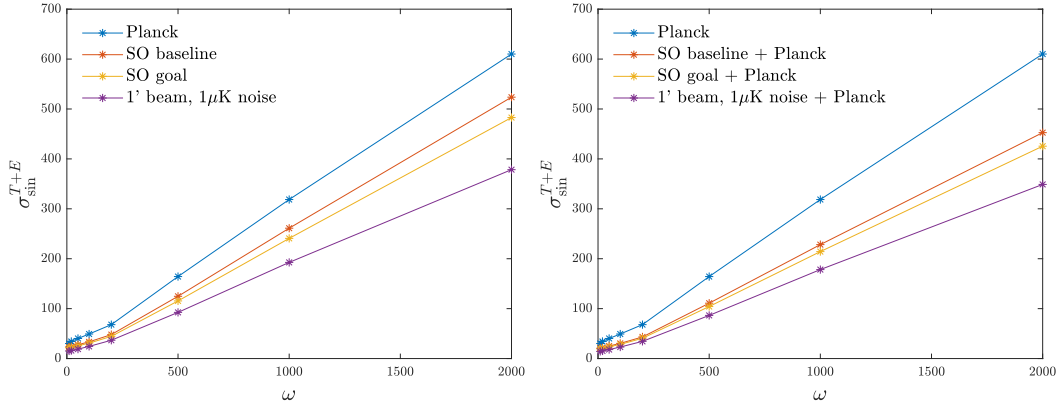


Fig. 4.4 Frequency dependence of the forecast error in comparison to Planck (left). All CMB-S4 specifications would improve constraints on feature models. The most sensitive setup with 1' beam and  $1\mu\text{K}\cdot\text{arcmin}$  noise is expected to yield error bars that are 1.6-2.1 times smaller than Planck. When the Planck results are combined with CMB-S4, we get even stronger constraints (right).

Figure 4.5 shows the results when only the CMB temperature data are used in the forecast. CMB-S4 would in fact be worse than Planck in terms of constraining  $f_{NL}^{\text{feat}}$  for this case. The loss in information due to less sky coverage overwhelms the increased sensitivity. We see again that the real strength of CMB-S4 experiments lies in measuring CMB polarisation.

Then how much information do we actually gain from adding E-mode polarisation? Figure 4.6 shows the ratio of  $\sigma_{\text{sin}}$ s between the temperature-only and polarisation-included analyses. The forecast error bars reduces up to 4.6 times smaller when polarisation information is added, which is much larger than the corresponding Planck value of 2.2. The ratio decreases overall when the joint statistics with Planck are considered. An intriguing feature of this plot is that the ratio is maximised around  $\omega = 200$  before it starts dropping again.

In order to gain insight on this behaviour, we performed some simplified computations using the power spectrum. We imposed oscillations on the primordial power spectrum as  $P'(k) = P(k)(1 + \sin(2\omega k + \phi))$ , which is just like our feature model bispectrum template but with  $\omega(k_1 + k_2 + k_3)$  replaced by  $\omega(k + k)$ .  $P'(k)$  is then projected to the late-time harmonic

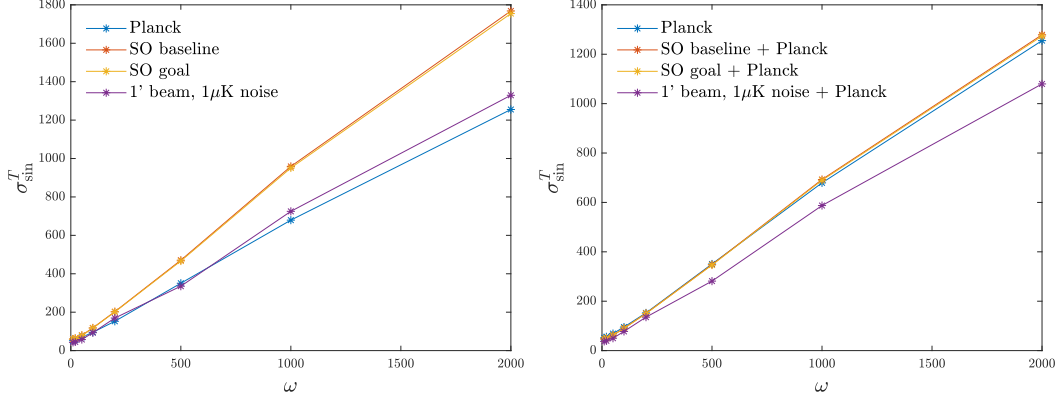


Fig. 4.5 Frequency dependence of the forecast error from temperature data only, in comparison to Planck (left). The CMB-S4 experiments would perform worse than Planck when only the temperature map is concerned. After the addition of Planck data the error bars improve only marginally (right). This shows that polarisation data is crucial for constraining feature models.

space using the transfer functions;

$$C_l'^{X_1 X_2} = \frac{2}{\pi} \int k^2 dk P'(k) \Delta_l^{X_1}(k) \Delta_l^{X_2}(k). \quad (4.30)$$

We observed that the fractional variation  $(C_l' - C_l)/C_l$  displays some oscillations in  $l$ , and the largest contribution comes from a term  $\propto \sin(2\omega l/\Delta\tau)$  where  $\Delta\tau$  represents the conformal distance to last scattering surface. This fact can be explained by approximating the transfer function as  $\Delta_l(k) \approx (1/3)j_l(k\Delta\tau)$  and noting that the spherical Bessel function has a sharp peak at  $l$  for large  $l$ 's. The integral in (4.30) therefore picks up a term proportional to  $\sin(2\omega l/\Delta\tau)$ .

The amplitude of these ‘maximal’ oscillations in  $(C_l' - C_l)/C_l$  were then computed using discrete Fourier transform for different values of oscillation scale  $\omega$  and two different phases  $\phi = 0, \pi/2$  (i.e. sine and cosine). The results are shown in Figure 4.7. Some extra wiggles to the graph come from the phase of oscillations imposed; we indeed see that graphs of sine and cosine oscillate between each other. Some peak features near  $\omega \approx 70$  and 140 arise from resonances with Baryonic Acoustic Oscillations.

We can think of the computed amplitude as a measure of information  $C_l$ 's contain about primordial oscillations. First of all, note that the amplitude in all four plots generally decreases as  $\omega$  grows. Previously in Figure 4.4 we saw that the amount of information obtained from the CMB is smaller for larger  $\omega$ 's, consistent with what can be said from the amplitude analysis. Moreover, the amplitudes for the EE mode are generally larger than the TT mode ones, and their difference is the largest in the  $\omega$  range of 70 to 300. This could

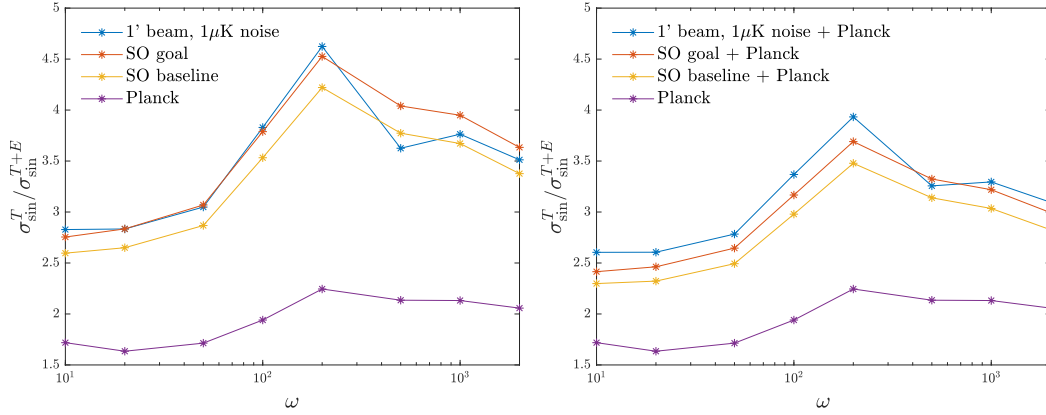


Fig. 4.6 Improvements on the forecast error when including E-mode polarisation data. Constraints from the CMB-S4 experiments would improve significantly from addition of the polarisation data. The improvement is maximised around  $\omega \approx 200$  Mpc.

serve as a heuristic explanation for the improvement in forecast error bars from including polarisation data being maximised around  $\omega = 200$ , as depicted in Figure 4.6.

#### 4.4.5 Comparison to scale invariant models

Our pipeline for forecasting  $f_{NL}^{\text{feat}}$  also yields forecasts for  $f_{NL}$  of the constant model. Constant models are scale invariant and have trivial shape, so that  $B(k_1, k_2, k_3) \propto (k_1 k_2 k_3)^{-2}$ . Forecasts on  $f_{NL}^{\text{const}}$  follow from our pipeline by simply setting the oscillation frequency  $\omega = 0$  and phase  $\phi = \pi/2$ . Table 4.1 summarises the forecast results for several different CMB-S4 specifications mentioned before, using both T and E data and in combination with Planck data from the regions of the sky not covered by CMB-S4. For the 1' beam and  $1\mu\text{K}$ -arcmin noise setup, the error bar is expected to be reduced by a factor of 2.3 compared to Planck.

	Planck	SO baseline + Planck	SO goal + Planck	1' beam, $1\mu\text{K}$ noise + Planck
$\sigma(f_{NL}^{\text{const}})$	23.4	14.9	14.0	10.4

Table 4.1 Forecasts on the estimation errors of  $f_{NL}$  for the constant model

The latest Planck constraints on  $f_{NL}$  of some popular bispectrum templates are given by  $f_{NL}^{\text{local}} = 2.5 \pm 5.7$ ,  $f_{NL}^{\text{equil}} = -16 \pm 70$ , and  $f_{NL}^{\text{ortho}} = -34 \pm 33$  [48]. CMB-S4 experiments are expected to yield better estimates on these as well. Table 4.2 summarises the forecast improvement ratio given in [18] together with the constant and feature model ratios computed in this work.

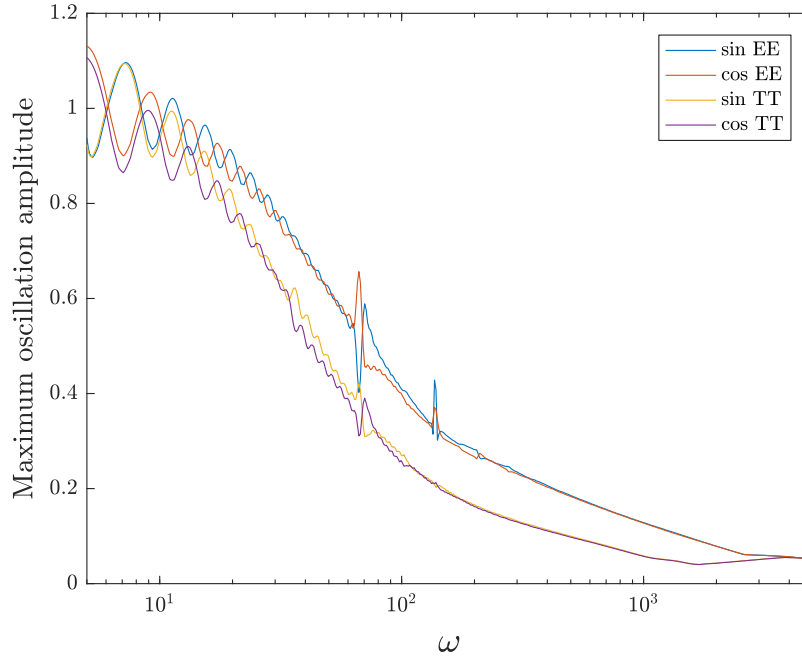


Fig. 4.7 The maximum amplitude of oscillations detected in fractional variations of the projected power spectrum  $C_l^{TT}$  and  $C_l^{EE}$ , when extra oscillations  $\sin(2\omega k)$  and  $\cos(2\omega k)$  were imposed on the primordial power spectrum. Heuristically this shows that E-mode polarisation is more sensitive to the primordial oscillations, especially in the  $\omega$  range of 70 to 300. Some peaks near  $\omega = 70$  and 140 arise from resonances with Baryonic Acoustic Oscillations.

To the authors' surprise, the estimation error for feature models does not improve as much as other templates. Feature models benefit much more from polarisation data than other scale independent shapes; for example,  $\sigma^T / \sigma^{T+E} = 4.6$  for the feature models with  $\omega = 200$  in CMB-S4 while the value equals 2.8 for the constant models. Because CMB-S4 would have significantly enhanced polarisation measurement sensitivity, we originally expected the feature models to be constrained significantly better than Planck.

In order to investigate this lack of improvement, we performed a breakdown analysis on the improvements gained from CMB-S4 temperature and polarisation; we computed  $\sigma(f_{\text{NL}})$  for the constant and feature models using each of the four combinations of Planck / CMB-S4 noise curves for temperature / polarisation (e.g. Planck T + CMB-S4 E). The results are summarised in Table 4.3.

We see that the constraints on feature models improve by a factor of 1.7 when swapping Planck polarisation noises with the CMB-S4 ones. This factor is indeed larger than the one for constant model, which equals 1.6. The difference is however not significant. It seems that the amount of feature signals in polarisation data left unexplored by Planck is not



	Local	Equilateral	Orthogonal	Constant	Feature ( $\omega = 200$ )
$\sigma^{\text{Planck}} / \sigma^{\text{CMB-S4}}$	2.5	2.1	2.4	2.3	2.0

Table 4.2 Expected improvement ratios of the  $f_{\text{NL}}$  estimation errors for the CMB-S4 1' beam,  $1\mu\text{K}$  arcmin setup, for various bispectrum templates. The local, equilateral and orthogonal results are quoted from [18].

$\sigma(f_{\text{NL}}^{\text{const}})$		E		$\sigma(f_{\text{NL}}^{\text{feat}})$		E	
improvements		Planck	CMB-S4	improvements		Planck	CMB-S4
T	Planck	1.0	1.6	T	Planck	1.0	1.7
	CMB-S4	1.1	2.2		CMB-S4	0.9	1.9

Table 4.3 Expected improvements on the estimation errors of  $f_{\text{NL}}$  for each combination of Planck / CMB-S4 temperature (T) and polarisation (E) data. Here the CMB-S4 assumes 1' beam and  $1\mu\text{K}$  arcmin noise. For feature model the oscillation frequency  $\omega = 200$  and phase  $\phi = 0$ . The sky fraction  $f_{\text{sky}} = 0.4$  for all cases except for Planck T + Planck E, for which  $f_{\text{sky}} = 0.76$ .

tremendously large compared to the constant model. The feature model improves less than the constant model when the temperature measurements are enhanced. In fact, for feature models the signal loss from smaller sky fraction  $f_{\text{sky}}$  eclipses the signal gain from more sensitive temperature measurements. This lack of improvements from temperature causes the full CMB-S4 constraints on the feature model not to improve as much as the constant model overall.

## 4.5 Discussion

Upcoming CMB Stage-4 experiments will provide an opportunity to measure CMB temperature and polarisation with greater precision. The estimation of primordial non-Gaussianity parameters would greatly benefit from the improvement in measurement sensitivity. In this research we made forecasts on  $f_{\text{NL}}$  for the feature models, which have not been done so far despite the growing interests on inflation models with primordial oscillations. For efficient forecasts we simplified the bispectrum estimator for  $f_{\text{NL}}$  by orthonormalising the covariance matrix, further optimising the computation. When the most sensitive CMB Stage-4 experiment specification of 1' beam and  $1\mu\text{K}$  arcmin noise is concerned, we expect a factor

of 1.7-2.2 times more stringent constraints compared to Planck. Under realistic Simons Observatory conditions the improvement would be about 1.3-1.6 to Planck.

Although this is not a massive boost in the estimation power, we can hope to verify current  $4\sigma$ -level signals found in the 2015 Planck analysis. It is also worth noting that the CMB-S4 experiments would allow us to explore modes  $l > 2000$ , especially since localised oscillations in this range are currently unconstrained. Moreover, though we have only considered linearly spaced oscillations in this work, we expect even better improvements on the models inducing logarithmically spaced oscillations. Higher  $l$  modes would promote the constraining power, since the oscillation slows down in small scales for this type of models and therefore gets less suppressed by the transfer functions. Lastly, cross-validation using these new statistically independent modes would be useful.

We also extensively studied how the forecasts depend on various parameters. Frequency dependences of the ratio between T and T+E forecasts were particularly illuminating - the improvement from adding polarisation information is maximised around  $\omega = 200$ . Some simplified calculations were presented to heuristically address this fact. Even though the estimation power on feature models massively benefit from the polarisation data, overall expected improvements compared to Planck are quite underwhelming. Breakdown analysis on temperature and polarisation contribution revealed that the feature models would indeed improve more than other scale-independent models if only the polarisation measurement sensitivity is enhanced to the CMB-S4 standards. However, boosts in the temperature measurements affect scale-independent models more so that they gain more information overall.

## Chapter 5

# High-Resolution CMB Bispectrum Estimator

Despite their major role in constraining a wide range of inflation models, there are only a few implementations of the CMB bispectrum estimator due to computational challenges. The Planck collaboration mainly utilised three independent approaches for their bispectrum analysis [48, 49]: KSW [31], Binned [8], and Modal [23]. Standard bispectrum templates for Local, Equilateral and Orthogonal shapes have been constrained using all three methods independently, while other more specific ones were covered by only a subset of them.

Some of the most challenging models to handle are those with oscillatory behaviour. Numerous theoretically well-motivated models fall into this category. Feature models, as discussed in the previous chapter, often predict linearly spaced oscillations in the bispectrum. Resonance models such as Axion monodromy, ones with varying speed of sound, ... all produce log-spaced oscillations modulated with various envelopes. (CHECK! NBD, DBI? PUT LOTS OF REFS HERE). Constraining such models are difficult since wobbles in the bispectra degrade numerical stability of the integrals involved.

Several simple models with oscillations have been studied in the latest Planck analysis using Modal and some specific KSW-type estimators introduced in [42]. Modal estimator covers wide range of oscillatory models, with and without envelopes, thanks to versatility of its mode expansion. It is however difficult to constrain models with high-frequency oscillations using generic mode functions. Modal code allows choosing a more tailored set of modes for this purpose, but the fact that there are *two* independent sets of mode functions - primordial and late-time - complicates targeted analyses. For each specific selection of mode functions in primordial ' $k$ ' domain, a suitable choice of basis has to be made in late-time ' $l$ ' space. Rapidly oscillating signals may also get lost during the projection from one to the other and cause some numerical issues.

On the other hand, adapted KSW-type estimators ([42], PUT ONE MORE FOR SIN-LOG!) may probe models with arbitrarily fast modulations in their bispectra. They exploit separability of specific oscillatory templates to obtain accurate constraints in model-by-model basis. However, this method is not applicable for any model with slightly more complicated bispectra. Even in cases where some clever mathematical trick enables calculation, it may not be always straightforward to modify the code accordingly. This was one of the main motivations behind this research project; can we have a bispectrum estimator which has the efficiency and versatility of Modal, but also benefits from the flexibility of KSW formalism for targeted analysis?

We developed a novel CMB bispectrum estimation pipeline CMB-BEst.<sup>1</sup> CMB-BEst has two main strengths over former methods. First of all, it is implemented for completely general basis sets, which allows broad analyses on inflationary models. In fact, the conventional KSW estimator is equivalent to a specific choice of basis in *CMB-BEst*. CMB-BEst can cover any model KSW estimator can, and does more; it can simultaneously constrain general bispectrum shapes through primordial mode expansion, just like Modal.

Secondly, CMB-BEst is designed to be able to handle complex and highly oscillatory signals. It does not require a separate set of basis functions for late-time  $l$  space, in contrary to Modal. More diverse and specialised choice of basis can therefore be made. The code will be used on numerous inflation models with complex oscillations yet to be investigated due to lack of resolution from previous methods. Potential choices of targeted basis for this purpose will be discussed in Section 5.1.2.

Every good thing comes at a price. For CMB-BEst, the price is computational cost. Combining the best of Modal and KSW estimators, CMB-BEst's formalism is more numerically demanding than both of them. Naïvely speaking, running CMB-BEst for one set of basis functions is equivalent to computing thousands of KSW estimators put together. It is prohibitively expensive unless properly and thoroughly optimised.

We invested considerable amount of time and effort on optimising the code. Separable mode expansions and subsequent algorithm design were studied in detail for maximal reduction in computational complexity. We also made full use of parallelisation techniques to exploit modern computing architecture. Improving data locality for efficient memory access yielded an order of magnitude speed-up. We illustrate our optimisation procedure in Section 5.2.

The code was then tested thoroughly both internally and against Planck analysis. We used CMB maps and simulations from the Planck satellite experiment and checked that

---

<sup>1</sup>Short for *CMB Bispectrum Estimator*. The goal of CMB-BEst is to be the best bispectrum estimator with wide applications and great precision.

*CMB-BEst* agrees with previous routines map-by-map for various bispectrum templates. Different choices of basis functions within *CMB-BEst* also yielded consistent results. We dedicate Section 5.3 to present the outcome of these consistency checks.

Lastly, we present some applications of the code which serves as a proof of concept. In particular, we connect CMB-BEst to PRIMODAL, an efficient numerical code for computing bispectra of primordial perturbations from a given single field model [15]. PRIMODAL uses separable modes for its computation, which enables template-free, direct model-to-constraint analysis when combined with CMB-BEst appropriately. Section 5.3.3 highlights some results from the combined pipeline. We also identify rooms for improvement and discuss future research direction.

Upcoming surveys will provide major improvements to constraints on primordial non-Gaussianity. Inflationary models with oscillations would also greatly benefit from the enhanced sensitivity, as we discussed in the previous chapter. It is therefore crucial to have a robust and flexible bispectrum estimation routine ready for the future surveys, especially the one which can handle high-frequency oscillations. Having another code independent from the existing ones would also be greatly beneficial for cross validation. We expect CMB-BEst to fill this role in near future.

## 5.1 Formalism

### 5.1.1 CMB-BEst formalism

Recall that the optimal CMB bispectrum estimator for a given template can be written as

$$\hat{f}_{NL} = \frac{1}{N} \sum_{l_j, m_j} \frac{\mathcal{G}_{m_1 m_2 m_3}^{l_1 l_2 l_3} b_{l_1 l_2 l_3}}{C_{l_1} C_{l_2} C_{l_3}} \left[ a_{l_1 m_1} a_{l_2 m_2} a_{l_3 m_3} - \left( \langle a_{l_1 m_1}^G a_{l_2 m_2}^G \rangle a_{l_3 m_3} + 2 \text{ cyc.} \right) \right]. \quad (5.1)$$

Here we omit superscripts  $X$  for temperature and polarisation for notational convenience. Even though the formalism in this section will be presented for CMB temperature data only, the method is general and can easily be extended to include polarisation. For estimation of the full covariance matrix  $C_{l m, l' m'}$  needed for the linear term, we use ensemble average from Gaussian simulations, as denoted by superscripts  $G$  and the bracket  $\langle \cdot \rangle$ .

The normalisation factor is given by

$$N = \sum_{l_j} \frac{h_{l_1 l_2 l_3}^2 b_{l_1 l_2 l_3}^2}{C_{l_1} C_{l_2} C_{l_3}}. \quad (5.2)$$

The core part of our estimation routine is the separable mode expansion of shape function;

$$S(k_1, k_2, k_3) := (k_1 k_2 k_3)^2 B(k_1, k_2, k_3) = \sum_{p_j} \alpha_{p_1 p_2 p_3} q_{p_1}(k_1) q_{p_2}(k_2) q_{p_3}(k_3). \quad (5.3)$$

Choices for the basis functions  $q_p(k)$  are detailed in the next section. Due to the separability, the reduced bispectrum reduces to a compact form of

$$b_{l_1 l_2 l_3} = \sum_{p_j} \alpha_{p_1 p_2 p_3} \int dr \tilde{q}_{p_1}(l_1, r) \tilde{q}_{p_2}(l_2, r) \tilde{q}_{p_3}(l_3, r), \quad (5.4)$$

where the *projected* mode functions are defined as

$$\tilde{q}_p(l, r) := \frac{2r^{\frac{2}{3}}}{\pi} \int dk q_p(k) \Delta_l(k) j_l(kr). \quad (5.5)$$

Radiative transfer functions  $\Delta_l(k)$  and spherical Bessel functions  $j_l(kr)$  are denoted the same way as the previous chapter.

Every term appearing in (5.1) except the Gaunt integral is now separable. Using the definition  $\mathcal{G}_{m_1 m_2 m_3}^{l_1 l_2 l_3} = \int d^2 \mathbf{n} Y_{l_1 m_1}(\mathbf{n}) Y_{l_2 m_2}(\mathbf{n}) Y_{l_3 m_3}(\mathbf{n})$ , we can render it separable at the cost of introducing an extra integral.

We define the filtered maps as

$$M_p^{(i)}(\mathbf{n}, r) := \sum_{l, m} \frac{\tilde{q}_p(l, r)}{C_l} a_{lm}^{(i)} Y_{lm}(\mathbf{n}), \quad (5.6)$$

where  $a_{lm}^{(i)}$ 's represent the spherical harmonic transform of the  $i$ th CMB map. For later convenience, we use a convention where the 0th map corresponds to the observed CMB map. Maps number 1- $N_{sims}$  are Gaussian simulations. Note that without the factors involving  $\tilde{q}$  and  $C_l$ 's,  $M$  is simply equal to the original map in real space. Each mode extracts different anisotropy scales present in the map.

The bispectrum estimator (5.1) reduces to

$$\hat{f}_{NL}^{(i)} = \frac{1}{N} \sum_{p_j} \alpha_{p_1 p_2 p_3} (\beta_{p_1 p_2 p_3}^{cub, (i)} - 3\beta_{p_1 p_2 p_3}^{lin, (i)}), \quad (5.7)$$

where most of the computation required is now contained in the ‘ $\beta$ ’s, given by

$$\beta_{p_1 p_2 p_3}^{cub,(i)} := \int dr \int d^2 \mathbf{n} M_{p_1}^{(i)}(\mathbf{n}, r) M_{p_2}^{(i)}(\mathbf{n}, r) M_{p_3}^{(i)}(\mathbf{n}, r), \quad (5.8)$$

$$\beta_{p_1 p_2 p_3}^{lin,(i)} := \frac{1}{N_{sims}} \sum_{j \neq i} \int dr \int d^2 \mathbf{n} M_{p_1}^{(j)}(\mathbf{n}, r) M_{p_2}^{(j)}(\mathbf{n}, r) M_{p_3}^{(i)}(\mathbf{n}, r). \quad (5.9)$$

Here we evaluate  $f_{NL}$  estimates for each of the Gaussian simulations  $i = 1, \dots, N_{sims}$ . Naturally, they are normally distributed with mean zero. Under the null hypothesis that the initial fluctuations are purely Gaussian and there exist no primordial non-Gaussianity, the value of  $f_{NL}$  estimated from the observed CMB map is also drawn from the same normal distribution. Any statistically significant deviations from zero would therefore allow us to reject the null hypothesis.

It is important to note that the  $\beta$  matrices depends only on the choice of mode functions and input map data, and are independent of the theoretical bispectrum considered. Once  $\beta^{cub}$  and  $\beta^{lin}$  are computed and stored, we may constrain any model of interest by decomposing the template to get  $\alpha$ , and then simply taking a dot product:  $\alpha \cdot \beta / N$ .

The normalisation can also be obtained in a similar fashion;

$$N = \sum_{p_j, p'_j} \alpha_{p_1 p_2 p_3} \Gamma_{p_1 p_2 p_3, p'_1 p'_2 p'_3} \alpha_{p'_1 p'_2 p'_3}, \quad (5.10)$$

or equivalently,  $N = \alpha^T \Gamma \alpha$ . We exploit separability once again to compute the  $\Gamma$  matrix;

$$\Gamma_{p_1 p_2 p_3, p'_1 p'_2 p'_3} := \int dr \int d\mu \mathcal{P}_{p_1 p'_1}(\mu, r, r') \mathcal{P}_{p_2 p'_2}(\mu, r, r') \mathcal{P}_{p_3 p'_3}(\mu, r, r'), \quad (5.11)$$

$$\mathcal{P}_{pp'}(\mu, r, r') := \sum_l \frac{2l+1}{(8\pi)^{1/3} C_l} \tilde{q}_{p'}(l, r) \tilde{q}_p(l, r') P_l(\mu), \quad (5.12)$$

where  $P_l(\mu)$ ’s are the Legendre polynomials.

In summary, CMB-BEst computes the main quantities:  $\beta^{cub}$ ,  $\beta^{lin}$ , and  $\Gamma$ . The most computationally expensive part is the linear term  $\beta^{lin}$  by a couple orders of magnitude in most cases. Considerable effort has been put to optimise corresponding part of the code, which will be detailed in the following sections.

### 5.1.2 Basis functions

One of the greatest strengths of CMB-BEst lies in its flexibility with the choice of mode functions. We decompose given shape as a linear combination mode function in three-dimensional space. Hence, we shall refer to them as ‘basis’ functions. Adopting a specialised

basis set provides optimised results to specific models of interest, while a more general construction of basis allows us to simultaneously constrain a wide range of models.

First, we observe that the KSW estimator [31] is derived from a simple monomial basis in our notation;

$$q_p(k) = k^{p-1}, \quad p = 0, 1, 2, 3. \quad (5.13)$$

All three standard templates - local, equilateral, and orthogonal - can be expressed as a sum of separable terms in the form  $q_{p_1}(k_1)q_{p_2}(k_2)q_{p_3}(k_3)$ . The shape function of the local template, for example, is given by

$$S^{local}(k_1 k_2 k_3) := 2A^2 \left[ \frac{k_1^2}{k_2 k_3} + \frac{k_2^2}{k_3 k_1} + \frac{k_3^2}{k_1 k_2} \right] \quad (5.14)$$

$$= 2A^2 [q_3(k_1)q_0(k_2)q_0(k_3) + q_0(k_1)q_3(k_2)q_0(k_3) + q_0(k_1)q_0(k_2)q_3(k_3)], \quad (5.15)$$

where  $A$  is the primordial power spectrum amplitude. Decomposition coefficients  $\alpha_{p_1 p_2 p_3}$  have three non-zero components:  $\alpha_{300} = \alpha_{030} = \alpha_{003} = 2A^2$ . Coefficients for the equilateral and orthogonal templates can similarly be found.

We set the scalar spectral index  $n_s = 1$  for simplicity above. In the presence of non-unit  $n_s$ , we modify the basis as follows;

$$q_p(k) = k^2 \left[ k_* \left( \frac{k}{k_*} \right)^{(4-n_s)/3} \right]^{p-3}, \quad p = 0, 1, 2, 3. \quad (5.16)$$

The pivot scale  $k_*$  is defined such that the power spectrum evaluates to  $A$  at  $k = k_*$ . Including  $k_*$  here ensures that the  $q_p(k)$ 's have the right units. Note that the prefactor  $k^2$  comes from the definition of shape function and is therefore unaffected by  $n_s$ . We will refer to this choice of mode functions to be the 'KSW' basis.

For studying models with linearly spaced, high-frequency oscillation, a Fourier-like basis

$$q_0(k) = \sin(\omega k), \quad q_1(k) = \cos(\omega k), \quad (5.17)$$

for a fixed  $\omega$  is an appropriate choice. This is in fact equivalent to the method we used to study feature models in Chapter 4. The small size of the basis lets us efficiently constrain theoretical models with given characteristic scale  $\omega$ . By scanning over a range of  $\omega$ , or including modes with different values of  $\omega$  in the basis, we may also perform a more comprehensive analysis of oscillatory features.



Lastly, we introduce a basis which consists of Legendre polynomials.

$$q_p(k) = P_p(\bar{k}), \text{ where } \bar{k} = \frac{2k - k_{\min} - k_{\max}}{k_{\max} - k_{\min}}. \quad (5.18)$$

Here we linearly map the range from  $k \in [k_{\min}, k_{\max}]$  to  $\bar{k} \in [-1, 1]$ , which is the interval where Legendre polynomials are defined. The number of modes are not bounded; the larger the basis, the more complete coverage of theory  $k$  space we get.

The Legendre basis has two main advantages over others. First of all, the mode functions are inherently orthogonal, so that  $\int_{-1}^1 d\bar{k} P_l(\bar{k}) P_{l'}(\bar{k}) = 0$  whenever  $l \neq l'$ . This property allows us to greatly simplify the way of decomposing theoretical templates. We elaborate on the decomposition method in Section 5.1.3.

Secondly, the Legendre basis enables direct connection to some numerical codes for computing bispectra from various inflationary models, most notably PRIMODAL [15]. PRIMODAL is a code for evaluating primordial bispectra from general single-field models. As opposed to other public codes, its output is expressed in terms of the expansion coefficients with respect to the Legendre polynomials. Hence, the result can be directly plugged in to CMB-BEst, creating one fluid pipeline from the model Lagrangian to estimation.

As noted in [15], we may augment the base set of Legendre polynomials with one or more extra functions for better description of some bispectrum templates. One solid choice is to add a mode  $q(k) = k^{n_s-2}$ , orthogonalised with respect to the rest of the basis. This significantly boosts the performance of decomposing local-type bispectra.

Ideally, we would like the  $k$  range used in the definition (5.18) to be as wide as possible so that more information from different scales are incorporated in the estimation process. Wider  $k$  range, however, also results in lower resolving power because the interval can fit more oscillations of given frequency. Polynomials of higher degrees are necessary to handle the same bispectra. We found that  $k_{\max}/k_{\min} = 1000$  is an overall sweet spot for analysing Planck data.

Throughout the rest of this thesis, we refer to a basis with the  $k^{n_s-2}$  mode and the first 29 Legendre polynomials, totalling 30 modes, defined in the  $k$  range with  $(k_{\min}, k_{\max}) = (2.09 \times 10^{-4}, 2.09 \times 10^{-1})$ , as the ‘Legendre’ basis. Any deviation from this set of parameters will be stated explicitly. Note that this is for our convenience during testing only; the code may take any choice of basis.

### 5.1.3 Primordial basis expansion

Our formalism assumes that the bispectrum shape of interest can be accurately represented as a linear combination of chosen basis set;

$$S(k_1, k_2, k_3) = \sum_{p_j} \alpha_{p_1, p_2, p_3} Q_{p_1 p_2 p_3}(k_1, k_2, k_3), \quad (5.19)$$

where the three-dimensional mode functions are defined as

$$Q_{p_1 p_2 p_3}(k_1, k_2, k_3) := q_{p_1}(k_1) q_{p_2}(k_2) q_{p_3}(k_3). \quad (5.20)$$

For some models the coefficients  $\alpha_{p_1 p_2 p_3}$  are obtained analytically. Local shape function with respect to KSW basis is a simple example;  $\alpha_{300} = \alpha_{030} = \alpha_{003} = 2A^2$  and zero otherwise. For other models, the shape function needs to be expanded with respect to the chosen basis.

Shape functions are defined on the same domain as bispectra:  $(k_1, k_2, k_3) \in \mathbb{R}^3$  where  $k_1$ ,  $k_2$ , and  $k_3$  form a triangle. We cannot observe scales smaller than a certain size in practice, which places an upper bound on  $k$ :  $k < k_{max}$ . The resulting domain in three dimensions is shown in Figure 5.1.

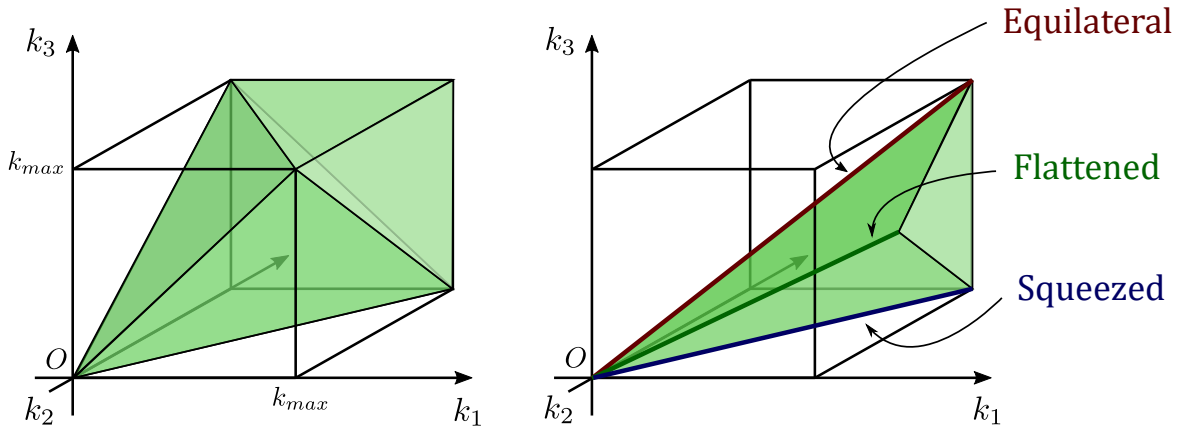


Fig. 5.1 Tetrapyd domain in which the shape functions are defined. Left: the full region specified by triangle inequalities and an upper bound  $k_{max}$ . Right: one sixth slice of the tetrapyd from which shape functions are uniquely determined by symmetry in the  $k$ 's. Edges representing the equilateral, flattened and squeezed configurations are annotated.

We follow [19] and denote this domain consisting of two tetrahedrons glued together as ‘tetrapyd’. Note that all shape functions of interest are symmetric in the  $k$ 's, so we may restrict our interest to a region where  $k_1 \geq k_2 \geq k_3$  (right of Figure 5.1). We dub the resulting tetrahedron with one sixth the original volume ‘the sliced’ tetrapyd, somewhat unoriginally. The three main types of triangle configurations correspond to three edges of the sliced

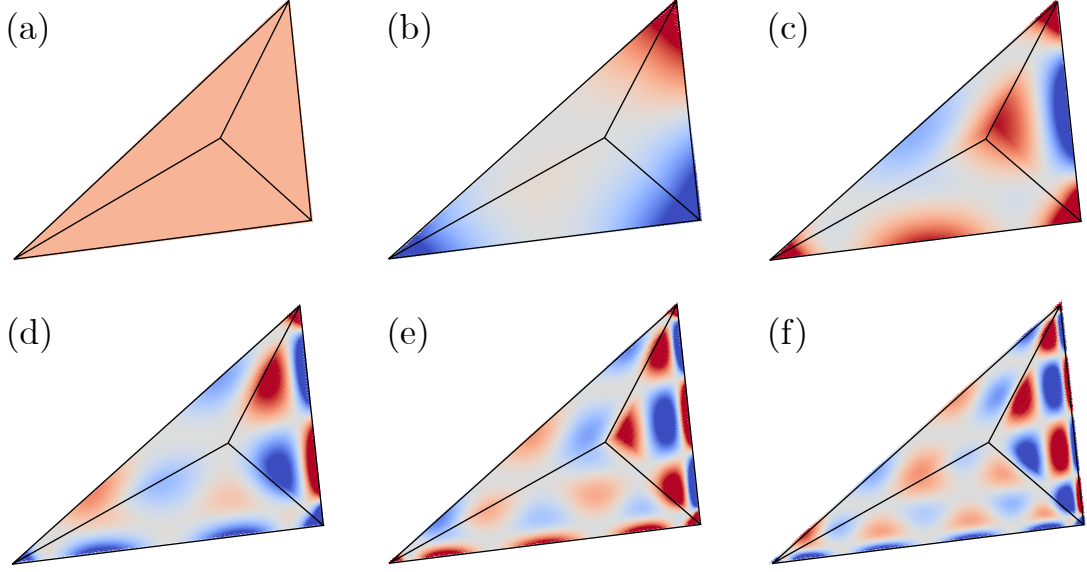


Fig. 5.2 Examples of our Legendre basis functions, evaluated on the sliced tetrapyd domain shown in Figure 5.1. Functions are defined as  $Q_{p_1 p_2 p_3}(k_1, k_2, k_3) := P_{p_1}(k_1)P_{p_2}(k_2)P_{p_3}(k_3)$ , where  $P_l(k)$  are Legendre polynomials. Here we plot  $p_1 = p_2 = p_3 = p$ , where  $p$  equals (a) 0, (b) 1, (c) 2, (d) 3, (e) 4, and (f) 5. A single colour map is used across plots: red and blue correspond to  $+1$  and  $-1$ , respectively.

tetrapyd: equilateral ( $k_1 = k_2 = k_3$ ), flattened ( $k_1 = k_2 + k_3$ ), and squeezed ( $k_1 = k_2 \gg k_3$ ).<sup>2</sup> Figure 5.2 shows some of the Legendre basis functions plotted in three dimensions.

Let  $V_{\mathbf{k}}$  be the subset of  $\mathbb{R}^3$  representing the sliced tetrapyd. By choosing a natural inner product

$$\langle S_1, S_2 \rangle = \int_{V_{\mathbf{k}}} d^3\mathbf{k} S_1(\mathbf{k})S_2(\mathbf{k}), \quad (5.21)$$

we restrict our attention to an  $L^2$  space defined on  $V_{\mathbf{k}}$ : a vector space consisting of square-integrable functions.<sup>3</sup> A set of three-dimensional basis functions  $Q_{\mathbf{p}}$  with size  $N$  spans a subspace  $U_Q \subset L^2(V_{\mathbf{k}})$  of dimension at most  $N$ .

<sup>2</sup>To be precise, the edges for flattened represent  $k_1/2 = k_2 = k_3$ , and the squeezed one is defined as  $k_1 = k_2$ ,  $k_3 = 0$ . The edges by themselves are unphysical, but points near these lines correspond to the limits described.

<sup>3</sup>Note that the local shape function  $S(k_1, k_2, k_3) = (k_1^2/k_2 k_3 + 2 \text{ cyc.})$  is not in fact square-integrable due to its divergence as  $k_i \rightarrow 0$ . We work around this problem by prescribing a lower bound  $k \geq k_{\min}$ , which is also the case in numerical calculations.

Using this notation, expanding a given shape function  $S$  with respect to a basis set  $Q$  is equivalent to finding its orthogonal projection into  $U_Q$ :

$$S = S^{\parallel} + S^{\perp}, \quad \text{where} \quad (5.22)$$

$$S^{\parallel} \in U_Q \quad \text{and} \quad \langle S^{\perp}, Q' \rangle = 0, \quad \forall Q' \in U_Q. \quad (5.23)$$

As long as  $\|S^{\perp}\| \ll \|S\|$ , we may approximate

$$S \approx S^{\parallel} = \sum_{\mathbf{p}} \alpha_{\mathbf{p}} Q_{\mathbf{p}}. \quad (5.24)$$

The decomposition coefficients  $\alpha$  are obtained by taking inner product with  $Q_{\mathbf{p}}$  on both sides.

$$\langle S, Q_{\mathbf{p}} \rangle = \langle Q_{\mathbf{p}}, Q_{\mathbf{p}'} \rangle \alpha_{\mathbf{p}'}. \quad (5.25)$$

From above, we can compute  $\alpha_{\mathbf{p}}$  by inverting the matrix  $\Gamma_{\mathbf{pp}'} = \langle Q_{\mathbf{p}}, Q_{\mathbf{p}'} \rangle$ . Alternatively, orthonormalising the basis with respect to the inner product  $\langle, \rangle$  turns  $\Gamma$  to an identity matrix, trivialising the inversion process.

We rewrote the formalism using linear analysis language here to emphasize two aspects of our primordial basis expansion. First, even though we choose a simple inner product (5.21) for now, the method is completely general, and we may freely choose a different inner product. For example, non-unit weights  $w(\mathbf{k})$  can be included in the integrand, and/or the domain of integration may be changed. Doing so alters how we decompose shape functions in terms of our basis.

Second, we highlight the fact that basis expansion is in essence a minimisation problem with respect to chosen inner product, which is often oblivious of late-time physics. Orthogonal projection of  $S$  to subspace  $U_Q$  is a point in  $U_Q$  which has minimal distance to  $S$ :  $\|S - S^{\parallel}\|$  is minimised. Obtained  $S^{\parallel}$ , however, is not necessarily the best description of  $S$  when we consider their late-time counterparts in  $l$  space. Some errors with small norm  $\|\Delta S\|$  might get enhanced when convolved with transfer functions, yielding large reduced bispectrum  $\Delta b_{l_1 l_2 l_3}$ . Meanwhile, sometimes large differences in  $S$  are completely unobservable late-time and provide mostly identical constraints on  $f_{NL}$ .

With these points in mind, we define metrics to compare shape functions in primordial space;

$$\text{Corr}(S_1, S_2) := \frac{\langle S_1, S_2 \rangle}{\sqrt{\langle S_1, S_1 \rangle \langle S_2, S_2 \rangle}}, \quad (5.26)$$

$$\varepsilon^2(S_1, S_2) := \frac{\langle S_1 - S_2, S_1 - S_2 \rangle}{\sqrt{\langle S_1, S_1 \rangle \langle S_2, S_2 \rangle}}. \quad (5.27)$$

$\text{Corr}(S_1, S_2)$  measures correlation between the two shapes and is independent of the normalisation.  $\varepsilon(S_1, S_2)$  is the distance between to shapes, which reduces to  $\sqrt{2 - 2 \text{Corr}(S_1, S_2)}$  when  $S_1$  and  $S_2$  have equal amplitude. We use both of these values to test if our primordial basis expansion has converged to target shape function.

Inverting the matrix  $\Gamma_{\mathbf{p}\mathbf{p}'} = \langle Q_{\mathbf{p}}, Q_{\mathbf{p}'} \rangle$  in 5.25 can be tricky in practice. The  $p_{\max}^3 \times p_{\max}^3$  matrix is not only large in size for high  $p_{\max}$ , but also near singular. Some of the three-dimensional mode functions  $Q_{\mathbf{p}}$  become linearly dependent within tetrapyd even if they are constructed from independent modes in one dimension. Presence of such degenerate modes induces severe numerical instability during inversion.

For our Legendre basis, we use a small trick to get around this problem. Motivated by the fact that Legendre polynomials form an orthogonal basis in one dimension, we extend the domain of integral in the inner product 5.21 to a cube containing the tetrapyd instead. Most template shape functions have an analytic form and can easily be extended in this region. As long as  $\int dk q_p(k) q_{p'}(k) = \delta_{pp'}$ , the decomposed coefficients for given  $S$  can be found by

$$\alpha_{p_1 p_2 p_3}^{(t)} = \int dk_1 \int dk_2 \int dk_3 S^{(t)}(k_1, k_2, k_3) q_{p_1}(k_1) q_{p_2}(k_2) q_{p_3}(k_3). \quad (5.28)$$

Note that the three-dimensional integral can now be split into three separate one-dimensional integrals in range  $[k_{\min}, k_{\max}]$ . By performing the three integrals one by one, we obtain a numerically stable algorithm that is fast and memory efficient. Decomposing a shape evaluated on  $1000^3 k$  grid points with respect to  $30^3$  Legendre basis functions only takes a few seconds in our C code.

After we obtain coefficients from (5.28), we evaluate accuracy of the expansion using the inner product defined in tetrapyd because it is the only physical region where our shape function matters. Since the cube includes tetrapyd, good convergence in cube guarantees small error within the tetrapyd in most cases. The only exception is when the target shape function blows up outside tetrapyd. We will see such examples in later sections.

## 5.2 Implementation and optimisation

CMB bispectrum estimation is a numerically challenging task. All existing approaches exploit the separability of multi-dimensional integrals to reduce computational complexity, because it is practically impossible otherwise. Planck analysis provided constraints to primordial non-Gaussianity from various bispectrum templates, but having limited computing resources was what stopped us from exploring further. Numerous shapes such as complex oscillatory models have been outside our reach despite their being theoretically well-motivated.

The CMB-BEst formalism significantly reduces the amount of computation needed for the CMB bispectrum estimation. Obtaining the linear term  $\beta^{lin}$  in (5.9), however, is still prohibitively expensive unless thoroughly optimised. Performance is especially crucial here since it directly affects the breath of models we can cover; the faster the code, the higher number of modes we can have, and the more shapes we can expand in our basis accurately.

In this section, we provide details for various aspects of our optimisation process: algorithm design, parallel computing, and data locality improvements. Final specifications and data files used are outlined at the end.

Throughout this section we will treat the functions of interest as discrete arrays. Our notations for indices and their limits are summarised in Table 5.1. We adopt simple trapezoidal rule for most numerical integrals. For the  $\mu$  integral in (5.11), however, we use Gauss-Legendre quadrature computed from the public code QUADPTS [25] due to highly oscillatory and unstable nature of the integral. Multi-dimensional arrays are stored in the row major order following the C convention for efficiency. We use the HEALPIX library [24] for pixelisation of the sky, which includes LIBSHARP [51] library for Spherical Harmonic Transforms (SHTs).

Table 5.1 Our index conventions for discretised arrays and their sizes.

Index	Range	Description
$r$	$[0, N_r)$	Line-of-sight integral $r$ grid index.
$p, p_j$	$[0, p_{max})$	Mode number. $p_j$ is a shorthand for $(p_1, p_2, p_3)$ .
$i, j$	$[0, N_{sims}]$	Map number. Index $i = 0$ corresponds to the observed CMB map, while $i > 0$ are for simulated Gaussian maps.
$n$	$[0, N_{pix})$	Map pixel number.
$l, m$	$[0, l_{max})$	Spherical harmonic multipole moments. Note $-l \leq m \leq l$ .
$\mu$	$[0, N_\mu)$	Gauss-Legendre quadrature $\mu$ grid index.

### 5.2.1 Algorithm

Our goal is to compute three key quantities:  $\Gamma$  (5.11),  $\beta^{cub}$  (5.8), and  $\beta^{lin}$  (5.9). The matrix  $\Gamma$  allows us to find the normalisation factor  $N$  for a given theoretical template, while the two  $\beta$ 's provide the amplitude of  $f_{NL}$  for each CMB maps and simulations used, up to normalisation.

In most cases of interest, the bottleneck point of our pipeline is computing the linear term  $\beta^{lin}$ . Even though the  $\Gamma$  matrix computation through (5.11) grows more rapidly with the number of basis functions ( $\propto p_{max}^6$ ) than the  $\beta$ 's ( $\propto p_{max}^3$ ), it does not involve operations with high-definition maps and remains subdominant in terms of total cost.

We dedicate this section to explain our algorithm design for  $\beta$  computation in detail. The discretised versions of (5.8-5.9) are given by

$$\beta^{cub}(i, p_1, p_2, p_3) = \sum_r \sum_n M(r, i, p_1, n) \cdot M(r, i, p_2, n) \cdot M(r, i, p_3, n), \quad (5.29)$$

$$\beta^{lin}(i, p_1, p_2, p_3) = \sum_r \sum_{j \neq i} \sum_n M(r, j, p_1, n) \cdot M(r, j, p_2, n) \cdot M(r, i, p_3, n). \quad (5.30)$$

The order of indices are chosen such that later calculations have optimal memory layouts. Some integral weights and factors are absorbed into arrays for brevity.

Note that the data arrays for different values of  $r$  are completely independent to each other. This provides us a natural way to distribute tasks. We compute and save contributions to  $\beta$ 's for each  $r$  separately. The summation over  $r$  is performed in the end. Therefore, throughout the rest of this chapter, we assume that  $r$  is fixed and drop the  $r$  dependence in descriptions of our algorithms.

The filtered map arrays  $M(i, p, n)$  are obtained as follows. A given map  $i$  is first transformed in to spherical harmonic coefficients  $a^{(i)}(l, m)$ s via SHT. We then compute  $\tilde{q}(p, l) * a(i, l, m) / C(l)$  from (5.6), which is fed into reverse SHT to synthesise the filtered maps.

As a rough guide to the size of each summations, we typically have  $N_{sim} \approx 150$  simulations,  $p_{max} = 30$  modes, and  $N_{pix} = 50,331,648$  pixels.<sup>4</sup> Considering the fact that one double-precision array of size  $\sim 50$  million pixels takes about 400MB of memory space, this is indeed a task for supercomputers.

Our first and the most straightforward method of computing  $\beta$ s are outlined in Algorithm 1. Computational complexity of each innermost loop is denoted on the right hand side.

Here, we first obtain the filtered maps  $M(i, p, n)$  via SHT for each map and modes. The full results are stored in memory. Next, we iterate through each map and set of modes  $(p_1, p_2, p_3)$  and sum over each of the map pixels to obtain  $\beta^{cub}$  and  $\beta^{lin}$ . Symmetries in the

<sup>4</sup>This value corresponds to  $N_{side} = 2048$  in Healpix.  $N_{pix} = 12N_{side}^2$

**Algorithm 1** Computing  $\beta$ s: the naïve method

---

```

1: Allocate  $M(i, p, n)$   $\triangleright$  Memory  $\sim N_{sims} \cdot p_{max} \cdot N_{pix}$ 
2:
3: for each map  $i$  do
4:   for each mode  $p$  do  $\triangleright O(N_{sims} \cdot p_{max} \cdot N_{pix}^{3/2})$ 
5:     compute  $M(i, p, n)$  by SHT
6:   end for
7: end for  $\triangleright M(i, p, n)$  ready
8:
9: for each map  $i$  do
10:   for each set of modes  $(p_1, p_2, p_3)$  do
11:     for each pixel  $n$  do  $\triangleright O(N_{sims} \cdot p_{max}^3 \cdot N_{pix})$ 
12:        $\beta^{cub}(i, p_1, p_2, p_3) += M(i, p_1, n) \cdot M(i, p_2, n) \cdot M(i, p_3, n)$ 
13:     end for
14:   end for
15: end for
16:
17: for each map  $i$  do
18:   for each map  $j \neq i$  do
19:     for each set of modes  $(p_1, p_2, p_3)$  do
20:       for each pixel  $n$  do  $\triangleright O(N_{sims}^2 \cdot p_{max}^3 \cdot N_{pix})$ 
21:          $\beta^{lin}(i, p_1, p_2, p_3) += M(j, p_1, n) \cdot M(j, p_2, n) \cdot M(i, p_3, n)$ 
22:       end for
23:     end for
24:   end for
25: end for

```

---



indices are respected; we only loop over  $(p_1, p_2, p_3)$  satisfying  $p_1 \geq p_2$  for the linear terms, and  $p_1 \geq p_2 \geq p_3$  for the cubic ones.

SHT typically scales as  $\propto l_{max}^3$ , where  $l_{max}$  is the maximum degree of spherical harmonic functions used. The total number of pixels  $N_{pix}$  grows  $\propto l_{max}^2$  when chosen appropriately for resolution, hence the SHT costs  $O(N_{sims} \cdot p_{max} \cdot N_{pix}^{3/2})$ . The most expensive part of this algorithm is still the loop where we calculate the linear term, which scales as  $O(N_{sims}^2 \cdot p_{max}^3 \cdot N_{pix})$ .

Our first major optimisation comes from the observation that we may swap the order of summations to reduce the computation. By precomputing  $C(p_1, p_2, n) = \sum_j M(j, p_1, n) \cdot M(j, p_2, n)$ , we require one fewer loop over maps for  $\beta^{lin}$ , leading to a factor of  $N_{sims} \sim 150$  improvement. Algorithm 2 shows a pseudocode for this method.

---

**Algorithm 2** Computing  $\beta$ s: optimised for computation

---

```

1: Allocate  $M(i, p, n)$   $\triangleright$  Memory  $\sim N_{sims} \cdot p_{max} \cdot N_{pix}$ 
2: Allocate  $C(p_1, p_2, n)$   $\triangleright$  Memory  $\sim p_{max}^2 \cdot N_{pix}$ 
3:
4: for each map  $i$  do
5:   for each mode  $p$  do  $\triangleright O(N_{sims} \cdot p_{max} \cdot N_{pix}^{3/2})$ 
6:     compute  $M(i, p, n)$  by SHT
7:   end for
8: end for  $\triangleright M(i, p, n)$  ready
9:
10: for each map  $j$  do
11:   for each pair of modes  $(p_1, p_2)$  do
12:     for each pixel  $n$  do  $\triangleright O(N_{sims} \cdot p_{max}^2 \cdot N_{pix})$ 
13:        $C(p_1, p_2, n) += M(j, p_1, n) \cdot M(j, p_2, n)$ 
14:     end for
15:   end for
16: end for  $\triangleright C(p_1, p_2, n)$  ready
17:
18: for each map  $i$  do
19:   for each set of modes  $(p_1, p_2, p_3)$  do
20:     for each pixel  $n$  do  $\triangleright O(N_{sims} \cdot p_{max}^3 \cdot N_{pix})$ 
21:        $\beta^{cub}(i, p_1, p_2, p_3) += M(i, p_1, n) \cdot M(i, p_2, n) \cdot M(i, p_3, n)$ 
22:        $\beta^{lin}(i, p_1, p_2, p_3) += C(p_1, p_2, n) \cdot M(i, p_3, n)$ 
23:     end for
24:   end for
25: end for

```

---

Note that the resulting sum for  $\beta^{lin}$  includes an unwanted contribution from the case where  $j = i$ , since  $C(p_1, p_2, n)$  is obtained by summing over all maps. Thankfully, this extra

contribution is exactly equal to the cubic term. We just have to subtract  $\beta^{cub}$  from the total sum to get the correct value of  $\beta^{lin}$ .

We shaved off a whole loop at the cost of extra memory usage. For our purposes  $N_{sims} \sim 150 > p_{max} = 30$ , so the additional space required for  $C(p_1, p_2, n)$  is relatively small compared to  $M(i, p, n)$ . The symmetry in  $p_1$  and  $p_2$  also means that we only need to store  $p_{max}(p_{max} + 1)/2$  maps instead of  $p_{max}^2$  for  $C$ .

Our next challenge is the amount of memory required to save  $M(i, p, n)$ . For the parameters mentioned above, this is  $\approx 1.8\text{TB}$ , which is quite significant. Though it is not impossible to find supercomputing systems which can accommodate such large arrays, reduction in memory usage would be highly beneficial. We seek to achieve it while keeping the overall computational complexity to be  $O(N_{sims} \cdot p_{max}^3 \cdot N_{pix})$  as before.

We observe that most summations are done for a single map  $i$ . The array  $C(p_1, p_2, n)$  is required to be computed before the main loop for  $\beta^{lin}$ , but otherwise there are no ‘mixing’ between the maps. We exploited this fact to develop Algorithm 3.

Algorithm 3 dramatically reduces the amount of memory required, at the cost of doubling the SHTs for computing  $M(i, p, n)$ s. The first time through, SHT results from each map are used to find  $C(p_1, p_2, n)$ . After a full loop over maps we have  $C(p_1, p_2, n)$  ready, another set of SHTs for each map allows us to obtain the  $\beta$ ’s.

SHTs have subdominant contribution to the total computation time even after becoming doubled in number. One of the main strengths of Algorithm 3 is that both the memory and computation time scale linearly with the number of simulations used,  $N_{sims}$ . In the future when a larger number of Gaussian simulations are required to acquire a more accurate estimate of the linear term, it is straightforward to adapt our method accordingly.

We choose Algorithm 3 to be our main method of computing  $\beta$ ’s for CMB-BEst.

### 5.2.2 Parallel computing

In order to fully benefit from the modern computer architecture, parallel computing is a must. In this section, we outline how CMB-BEst was parallelised for optimal performance on supercomputers.

Following [29], we discuss parallelism in three different levels: domain, thread, and data. They mostly correspond to nodes, cores, and registers in modern computer clusters. Each level has distinct characteristics which make them ideal for different parallelisation techniques. We make the full use of each level in our methodology.

*Domain* parallelism refers to dividing the task into many domains where each domain entails heavy computation, while having limited data communication between them. Since the domains are largely independent, Message Passing Interface (MPI) is a suitable tool for

**Algorithm 3** Computing  $\beta$ s: fast and memory efficient

---

```

1: Allocate  $m(p, n)$   $\triangleright$  Memory  $\sim p_{max} \cdot N_{pix}$ 
2: Allocate  $C(p_1, p_2, n)$   $\triangleright$  Memory  $\sim p_{max} \cdot p_{max} \cdot N_{pix}$ 
3:
4: for each map  $i$  do
5:   for each mode  $p$  do  $\triangleright O(N_{sims} \cdot p_{max} \cdot N_{pix}^{3/2})$ 
6:     compute  $M(i, p, n)$  by SHT and store in  $m(p, n)$ 
7:   end for
8:
9:   for each pair of modes  $(p_1, p_2)$  do
10:    for each pixel  $n$  do  $\triangleright O(N_{sims} \cdot p_{max}^2 \cdot N_{pix})$ 
11:       $C(p_1, p_2, n) += m(p_1, n) \cdot m(p_2, n)$ 
12:    end for
13:  end for
14: end for  $\triangleright C(p_1, p_2, n)$  ready
15:
16: for each map  $i$  do
17:   for each of mode  $p$  do  $\triangleright O(N_{sims} \cdot p_{max} \cdot N_{pix}^{3/2})$ 
18:     compute  $M(i, p, n)$  by SHT and store in  $m(p, n)$ 
19:   end for
20:
21:   for each set of modes  $(p_1, p_2, p_3)$  do
22:    for each pixel  $n$  do  $\triangleright O(N_{sims} \cdot p_{max}^3 \cdot N_{pix})$ 
23:       $\beta^{cub}(i, p_1, p_2, p_3) += m(p_1, n) \cdot m(p_2, n) \cdot m(p_3, n)$ 
24:       $\beta^{lin}(i, p_1, p_2, p_3) += C(p_1, p_2, n) \cdot m(p_3, n)$ 
25:    end for
26:  end for
27: end for

```

---

parallelisation. MPI is a communication protocol where many instances ('ranks') of the same code may transfer data while running separately from each other. A perfect example of domain parallelism in CMB-BEst would be our line-of-sight integration over  $r$ . Almost no data are shared between different  $r$ s, despite the heavy computational cost from map operations within each domain. CMB-BEst therefore scales well with the number of MPI ranks.

*Thread* parallelism opportunities arise when there are many independent computational tasks on a single set of data. Most modern supercomputers use multi-core processors. Each core, or processing units, can run one or more threads, executing instructions independently from each other while sharing memory space. Note that MPI would not be as effective here due to the large amount of data sharing needed; ranks have to either continuously communicate with each other, or store individual copies of the data. This type of parallelism is extremely common in many applications, including SHTs and map integrations in CMB-BEst. Open Multi-Processing (OpenMP) is one of the most popular implementations of multi-threading publicly available. We utilise the C OpenMP interface in our code.

*Data* parallelism applies when same arithmetic operations are applied to multiple data items, ideally adjacent in memory space. This type of parallel processing is called SIMD: Single Instruction, Multiple Data. Many procedures involving large arrays fall into this category. We use Advanced Vector Extensions (AVX) supported by Intel processors to exploit data parallelism in CMB-BEst, especially for operations involving large (filtered) map arrays. In particular, Intel's Xeon Phi series implement AVX-512, where 512-bit registers hold up to 8 double-precision floating numbers. A single instruction can be applied on all of them at once in a single clock cycle, providing a major boost to computation speed. We explicitly align large arrays in memory for optimal vectorisation performance.

Table 5.2 summarises discussions in this section.

### 5.2.3 Data locality

We implemented Algorithm 3 and profiled using the Intel VTune Amplifier. Our program was found to be memory-bound, which means that its speed is limited mainly by the amount of memory available and the speed of memory access. The CPU speed, rate of the file I/O, and MPI communication all have subdominant contributions in comparison. This is somewhat expected, since our method deals with large map arrays. The number of operations on each data element is small compared to the size of data, causing the CPUs to be 'starved' for data to work on most of the time. Our final set of optimisation focusses on improving memory access patterns.

Table 5.2 Three levels of parallelism utilised in CMB-BEst. The levels and characteristics are chosen based on [29].

	Characteristics	Methods	Utilisation
Domain Parallelism	<ul style="list-style-type: none"> <li>• Limited data communication between domains</li> <li>• Heavy computation within the domain</li> </ul>	MPI	<ul style="list-style-type: none"> <li>• Line of sight <math>r</math> integration split into independent tasks</li> </ul>
Thread Parallelism	<ul style="list-style-type: none"> <li>• Data sharing between threads</li> <li>• High proportion of independent tasks</li> </ul>	OpenMP	<ul style="list-style-type: none"> <li>• SHT</li> <li>• Map patches divided across threads</li> </ul>
Data Parallelism	<ul style="list-style-type: none"> <li>• Same operation applied to multiple data items</li> </ul>	SIMD	<ul style="list-style-type: none"> <li>• Map pixel integration vectorised using AVX-512</li> <li>• Data vectors explicitly aligned in memory for optimal performance</li> </ul>

CPUs of most modern computers contain a small amount of memory attached to them called *cache*. Recently used data and instructions are stored in cache memory so that reusing them is more efficient; accessing cache is much faster than loading from the main, larger memory often shared with other CPUs. Cache is often divided into multiple levels. The smallest and fastest is L1 cache, which is the first level a CPU checks for data. When the required data is not stored in L1 cache, a *cache miss* occurs. The system then has to look further down the cache levels to fetch the wanted data, incurring a large time loss. It is therefore crucial to reuse data as many times as possible before it is lost from cache.

Furthermore, the cache ‘caches’ memory locations in units of cache lines, or chunks of memory containing multiple data elements. Accessing memory locally therefore significantly increases the chance of cache hits, boosting overall performance. Array operations, for example, are optimised when they are stored in consecutive memory locations due to this fact.

CMB-BEst has been modified in two ways to improve data locality and memory performance. The first one was simple yet effective; we made sure to initialise large arrays within the same OpenMP construct as the main computation loop. This guarantees the physical memory of array elements to be allocated near the cores where they are going to be used in. Memory access during the main computation loop is therefore much faster than otherwise. Systems with non-uniform memory access (NUMA) especially benefits from this method. For CMB-BEst, we gained 2 times speed-up compared to when a single master thread initialised the entire array.

The second optimisation centres around *cache blocking*, a technique used to maximise data reuse. Let us focus on the main computation loop in Algorithm 3:

```
for each set of modes  $(p_1, p_2, p_3)$  do
  for each pixel  $n$  do
     $\beta^{cub}(i, p_1, p_2, p_3) += m(p_1, n) \cdot m(p_2, n) \cdot m(p_3, n)$ 
     $\beta^{lin}(i, p_1, p_2, p_3) += C(p_1, p_2, n) \cdot m(p_3, n)$ 
  end for
end for
```

In every loop over the set of modes  $(p_1, p_2, p_3)$ , four large arrays are read from memory:  $m(p_1, \cdot)$ ,  $m(p_2, \cdot)$ ,  $m(p_3, \cdot)$ , and  $C(p_1, p_2, \cdot)$ . Each of them take up around 400MB of memory. Since their size is greater than the cache storage capacity, data in the front of them are gone from cache by the time a loop over  $n$  completes. All four arrays will then have to be loaded from main memory again when the next iteration starts.

Suppose that the map arrays had smaller size and all of them fit in one of the cache levels instead. After one loop iteration over  $n$  for  $(p_1, p_2, p_3)$ , the arrays now remain in cache. Then the next loop on  $(p_1, p_2, p_3 + 1)$  begins, and the arrays  $m(p_1, \cdot)$ ,  $m(p_2, \cdot)$ , and  $C(p_1, p_2, \cdot)$  are required again for computation. They can now be accessed from cache, which saves significant amount of time. We see that each data element is reused multiple times before discarded from cache in this case.

Motivated by these facts, we divide the map array into equally sized blocks so that each patch can now fit inside the cache memory. We restructure the loop as follows.

```
for each block  $b$  do
  for each set of modes  $(p_1, p_2, p_3)$  do
    for each pixel  $n'$  in block do
       $\beta^{cub}(i, p_1, p_2, p_3) += m(p_1, n') \cdot m(p_2, n') \cdot m(p_3, n')$ 
       $\beta^{lin}(i, p_1, p_2, p_3) += C(p_1, p_2, n') \cdot m(p_3, n')$ 
    end for
  end for
end for
```

**end for**

The new pixel numbers are calculated as  $n' = B \cdot b + n$ , where  $B$  is the size of each block and  $0 \leq n < B$ . We have not changed the total number of arithmetic operations required, so the computational complexity remains constant. Meanwhile, data locality within each block is greatly improved, as each of the blocked arrays are now small enough to fit in cache. Each data element is accessed in closer succession temporarily as well.

One caveat here is that having too many blocks may degrade performance. There exist non-negligible overhead coming from an extra *for* loop and the OpenMP construct used over  $n'$ . The block size divided by number of cores should not be smaller than the size of cache lines either. The optimal size of cache blocks depends on the memory architecture of the processor used. This often needs to be found empirically.

Figure (5.3) shows how runtime of a small test code varies with the number of cache blocks used. The code was run on the Intel Gold 6154 processor, which is an 18-core high performance chip with total L1, L2, and L3 cache memory sizes of 1.125MiB, 18MiB, and 24.74MiB, respectively [28]. Even though some parameters such  $N_{sims}$  are tuned down for faster testing, this is representative of the full computation.

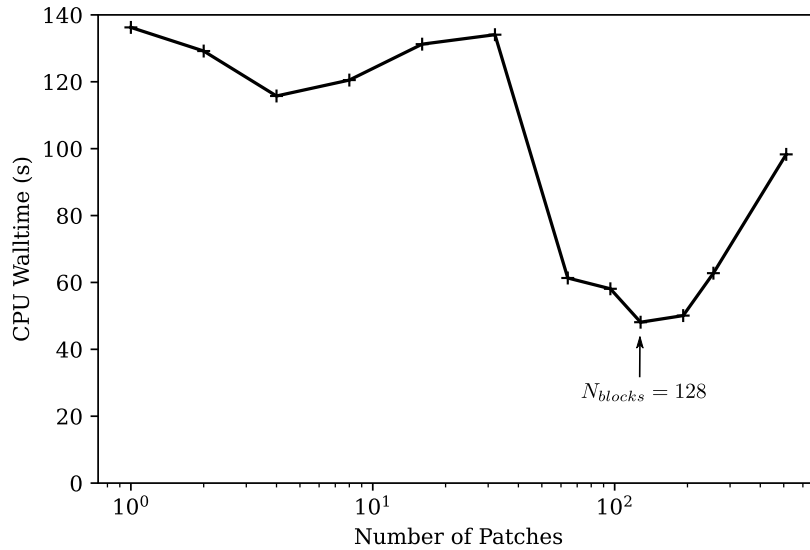


Fig. 5.3 Cache block optimisation. Total wall time of a test code for computing  $\beta$ s was measured while varying the number of cache blocks used. Having 128 blocks is optimal for the 18-core Intel Gold 6154 processor.

We find a significant improvement in performance moving from 32 to 48 blocks when the block size drops from 12MiB to 8MiB. This is precisely when three blocks are allowed

fit in L3 cache (24.7MiB) at the same time. Improved data locality dramatically reduces time spent on memory access as we expected. The optimal number of blocks was found to be 128; each segment contains about 400,000 elements and takes up 3MiB of memory, which is 1/6 and 1/8 of L2 and L3 cache size, respectively. We gain roughly three times speed-up compared to the original code without cache blocking.

Algorithm 4 summarises our final implementation of  $\beta$  computation code, now with cache blocking and OpenMP construct indicators.

---

**Algorithm 4** Computing  $\beta$ s: our final implementation

---

```

1: Allocate  $m(p, n)$ 
2: Allocate  $C(p_1, p_2, n)$ 
3:                                     ▷ Both initialised within OpenMP construct over  $n$ 
4: for each map  $i$  do
5:   for each mode  $p$  do
6:     compute  $M(i, p, n)$  by SHT and store in  $m(p, n)$        ▷ OpenMP within SHT
7:   end for
8:
9:   for each block  $b$  do
10:    for each pair of modes  $(p_1, p_2)$  do
11:      for each pixel  $n'$  in block do                               ▷ OpenMP for construct
12:         $C(p_1, p_2, n') += m(p_1, n') \cdot m(p_2, n')$ 
13:      end for
14:    end for
15:  end for
16: end for                                     ▷  $C(p_1, p_2, n)$  ready
17:
18: for each map  $i$  do
19:   for each of mode  $p$  do
20:     compute  $M(i, p, n)$  by SHT and store in  $m(p, n)$        ▷ OpenMP within SHT
21:   end for
22:
23:   for each block  $b$  do
24:    for each set of modes  $(p_1, p_2, p_3)$  do
25:      for each pixel  $n'$  in block do                               ▷ OpenMP for construct
26:         $\beta^{cub}(i, p_1, p_2, p_3) += m(p_1, n') \cdot m(p_2, n') \cdot m(p_3, n')$ 
27:         $\beta^{lin}(i, p_1, p_2, p_3) += C(p_1, p_2, n') \cdot m(p_3, n')$ 
28:      end for
29:    end for
30:  end for
31: end for

```

---



## 5.3 Validation

CMB bispectrum estimation is not only computationally challenging but also prone to numerical instabilities unless implemented carefully. We invested considerable amount of time after the development of CMB-BEst in validating various aspects of the code. We highlight some of our validation efforts in this section, checking consistency within the program itself (section 5.3.1) and against existing codes such as Modal [23] (section 5.3.2).

### 5.3.1 Internal consistency checks

CMB-BEst is a general code where one can freely choose a set of basis functions. Three of our main options are the ‘KSW’ basis (5.16), ‘Legendre’ basis (5.18, augmented with  $q(k) = k^{n_s-2}$ ) as discussed previously in Section 5.1.2, and Fourier basis (5.17). Both KSW and Legendre basis sets can cover the standard templates: local, equilateral, and orthogonal (see e.g., [47] for definitions). The KSW basis provides an exact form to the three templates by choosing appropriate powers of  $k$  as its basis elements. On the other hand, the templates are expanded in terms of separable Legendre polynomials up to some fixed degree  $p_{max}$  for the Legendre basis. As long as  $p_{max}$  is sufficiently large, most smooth bispectrum shapes can be represented accurately.

Our first consistency check is shown in Figure 5.4, where we compare the  $f_{NL}$  estimates from the Planck 2018 CMB map and 140 full focal plane (FFP10) realistic Gaussian simulations [46]. We use CMB maps obtained through the SMICA component separation method [9, 45]. On the left hand side are scatter plots of  $f_{NL}$  values obtained using each of the two basis sets. In an ideal case where the two estimates are identical for every test maps, all the points would lie on a straight line given by  $y = x$ . Drawn in dashed red line is the best linear fit to the data. Its slope, intercept, and the  $R$ -squared value are annotated below. On the right is a more detailed plot of computed  $f_{NL}$  for each map.

We see that results from the two different sets of basis are in good agreement. The  $R$ -squared value of the linear fit is greater than 0.99 for Local, and 0.999 for Equilateral and Orthogonal shapes. The intercept and sample mean are also near zero. We do not find any systematic discrepancies across the shapes from individual map estimates either.

The fact that results from the KSW and Legendre basis are consistent validates multiple aspects of our pipeline. First of all, we can deduce that the Legendre basis expansion (5.28) accurately represents the bispectrum shapes of interest, especially since the KSW basis is designed to be exact for the three standard shapes. Having  $p_{max} = 30$  modes is more than sufficient. Figure 5.5 explicitly compares results obtained from Legendre bases with  $p_{max} = 29$  and 30, while keeping everything else the same. The two results show absolute

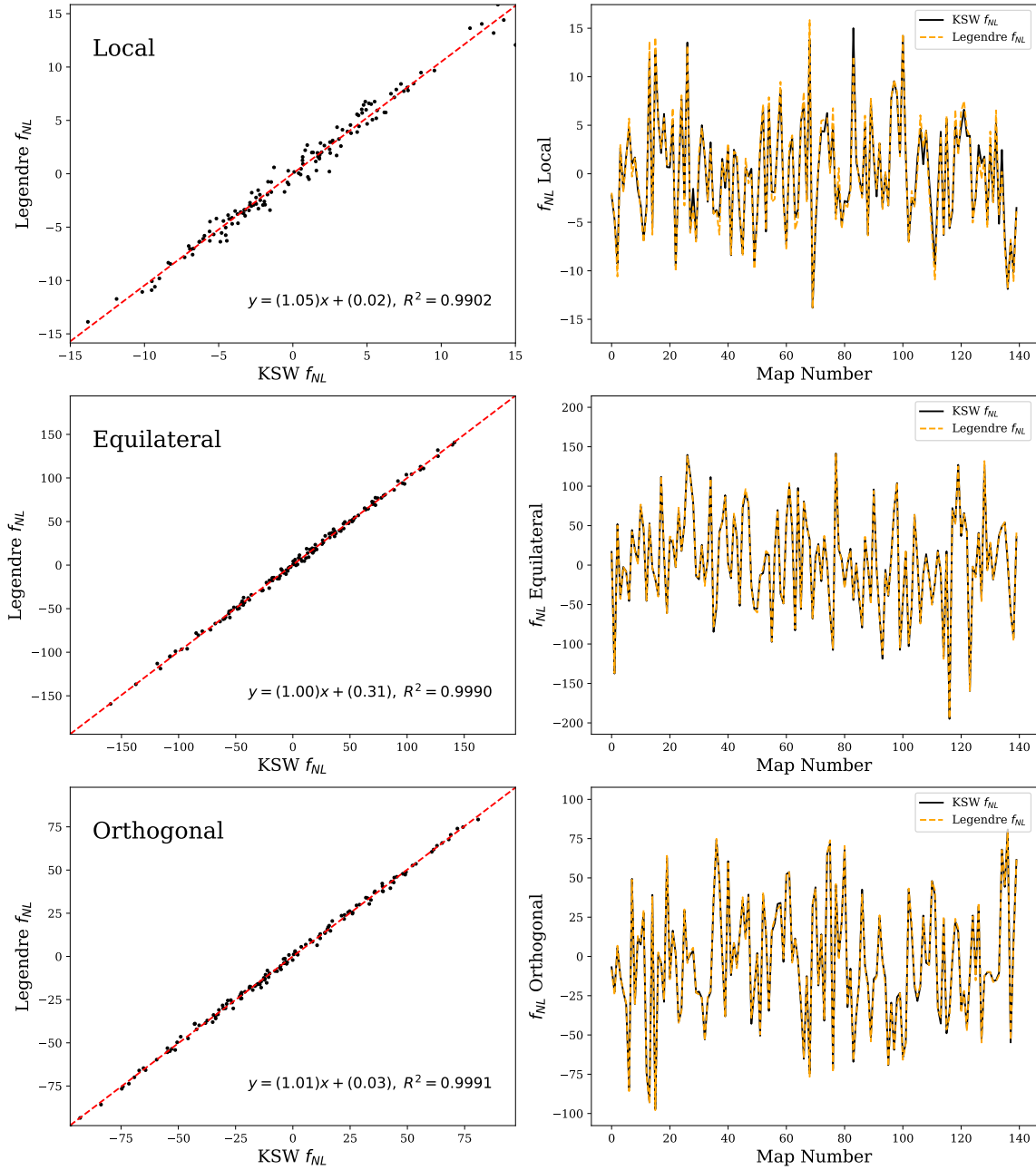


Fig. 5.4 Map-by-map comparison of  $f_{NL}$  estimates for standard templates, evaluated using each of the KSW and Legendre basis sets. Planck 2018 CMB map and 140 FFP10 simulations have been used, each representing a single point on the scatter plot shown left. Details of the linear best-fit to data (red dashed) is annotated below. On the right hand side shows a plot of  $f_{NL}$  values for each map. In the ideal case where the two basis sets yield identical results, we should see all the points on  $y = x$  for the left plot, and exactly overlapping graphs for the right. For more information on each of the three theoretical templates used, see e.g., [47].

agreement, the largest of errors less than  $O(10^{-5})$ . This further confirms that our expansion using Legendre polynomials have completely converged.

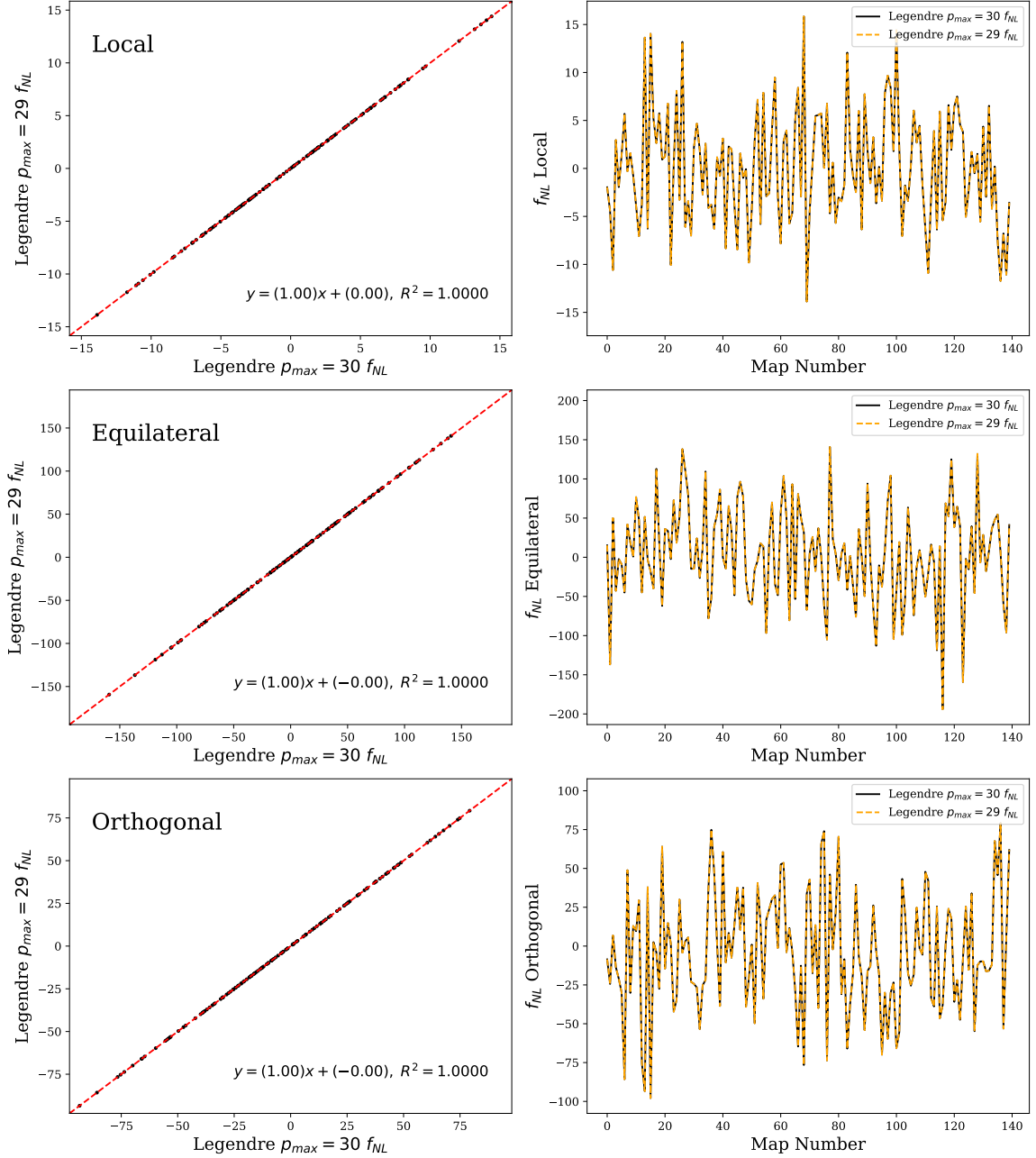


Fig. 5.5 Map-by-map comparison of  $f_{NL}$  estimates for standard templates using the Legendre basis with different number of modes:  $p_{max} = 29$  and  $30$ . The two results agree with error less than  $O(10^{-5})$ , as can be seen from the scatter plots (left) and map-by-map plots (right). This confirms that our expansion using Legendre polynomials has completely converged for these bispectrum shapes.

Secondly, we validated the accuracy of linear term and lensing-ISW bias calculations through sample mean of  $f_{NL}$  estimates from lensed simulations. When we exclude either of the two, we find the sample mean to be far from zero. The error is especially large for Local template. Linear term accounts for the anisotropy introduced by masking parts of the observed sky. The squeezed limit contribution to bispectrum comes from couplings between a pair of small-scale modes and a large-scale one, making it more susceptible to bias from partial coverage. Presence of sky masks therefore offsets the  $f_{NL}$  estimates from Local shape which has large squeezed limit. Lensing-ISW bias is also the largest in squeezed configurations and affects Local  $f_{NL}$ . The fact that our lensed Gaussian simulations have  $f_{NL}$ s fluctuate around 0 validates our bias subtractions.

Lastly, we check that CMB-BEst accurately preserves optimality of the CMB bispectrum estimator. In the weak non-Gaussian limit, the estimator (5.1) saturates the Cramer-Rao bound. Its expected variance is the lowest amongst all possible unbiased bispectrum estimators of  $f_{NL}$ . Heuristically speaking, the estimator extracts as much information about non-Gaussianity as possible from the CMB bispectrum. As we discussed in Chapter 4, this bound only depends on the Fisher information determined from normalisation;  $Var[\hat{f}_{NL}] = F^{-1} = 6/N$ . We refer to this value as the *theoretical* variance (the best possible from theory). Meanwhile, individual  $f_{NL}$  estimates from simulated maps and independent and normally distributed. Sample variance obtained from  $N_{sims}$  simulations should therefore approach the theoretical variance as  $N_{sims} \rightarrow \infty$ . Table 5.3 summarises calculated values of the two types of variances discussed.

Table 5.3 Comparison of the sample and theoretical variances obtained from  $f_{NL}$  estimates of standard shapes, computed using each of the KSW and Legendre basis sets. Sample variances are within  $1\sigma$  interval from theoretical values assuming that the 140 individual  $f_{NL}$ 's from simulated maps are normally distributed. This is statistically consistent with optimality of our bispectrum estimator.

Template	Basis	Sample Variance	Theoretical Variance	(Sample)/(Theory)
Local	KSW	5.5	5.3	1.04
	Legendre	5.9	5.7	1.04
Equilateral	KSW	61.2	67.7	0.90
	Legendre	61.7	67.7	0.91
Orthogonal	KSW	37.7	33.7	1.12
	Legendre	38.0	33.9	1.12

Note that the numbers do not match up exactly between sample and theoretical variances. The estimator for sample variance  $\hat{S}^2 = (\sum_i (f_{NL}^{(i)})^2) / N_{sims}$  follows chi-squared distribution with  $N_{sims} - 1$  degrees of freedom under our assumptions. Standard deviation corresponding to the (normalised) distribution equals  $\sqrt{2/(N_{sims} - 1)}$ , which is  $\approx 0.12$  for  $N_{sims} = 140$ . It is therefore not surprising to see our sample variances differ up to 12% from the theoretical ones.

We performed further checks to ensure that this discrepancy is due to statistical fluctuations rather than systematic errors. The ratio between sample and theoretical variances remained nearly constant across the KSW and Legendre basis from CMB-BEst, as well as Planck's Modal pipeline on the same set of simulated maps. Meanwhile, sample variances evaluated from independent sets of simulations do fluctuate around the theoretical value. A closer check has been done for each of the mode sets  $(p_1, p_2, p_3)$  in the Legendre basis. The decomposition coefficient  $\alpha$  is set to be 1 at  $(p_1, p_2, p_3)$  and its permutations, while vanishing everywhere else. Substituting into (5.7 and (5.10), we get

$$f_{NL}^{(i)} = \frac{1}{N} \left[ \left( \beta_{p_1 p_2 p_3}^{cub, (i)} - 3\beta_{p_1 p_2 p_3}^{lin, (i)} \right) + 5 \text{ cyc.} \right], \quad (5.31)$$

$$N = 6 (\Gamma_{p_1 p_2 p_3, p_1 p_2 p_3} + \Gamma_{p_1 p_2 p_3, p_1 p_3 p_2} + \cdots + \Gamma_{p_1 p_2 p_3, p_3 p_2 p_1}). \quad (5.32)$$

Here we assumed that  $p_1, p_2, p_3$  are distinct for convenience. Corresponding sample and theoretical variances have been compared for each of the modes. Overall, they are found to be statistically consistent as before.

While Figure 5.4 shows excellent agreement between results from the KSW and Legendre basis sets overall, there are small but noticeable scatters in the plot for Local shape. The slope of linear best fit is also slightly above 1, meaning that  $f_{NL}$  estimates from Legendre routine tend to vary 5% more than the KSW ones. Larger variance means less information extracted. Our first hypothesis was that Legendre polynomials are losing small fraction of information due to their fixed  $k$  range in their definition (5.18). We test this by increasing the range by changing  $k_{max}/k_{min} = 1000$  to 2000. The results are shown in Figure 5.6.

Our main focus of this figure lies on Local template results. Estimates from the KSW and Legendre basis sets match almost perfectly now. When altering the ratio  $k_{max}/k_{min}$ , we fixed the  $k_{max}$  and lowered  $k_{min}$ . Including more small- $k$ , or large scale modes provides extra information in the bispectrum. Local shape is especially affected by this, since squeezed configurations including one of these extra large scale modes have a more significant contribution to the total estimate. Also note that  $k_{max}/k_{min} = 2000$  is comfortably larger than the equivalent ratio in harmonic space  $l_{max}/l_{min} = 2500/2$ .

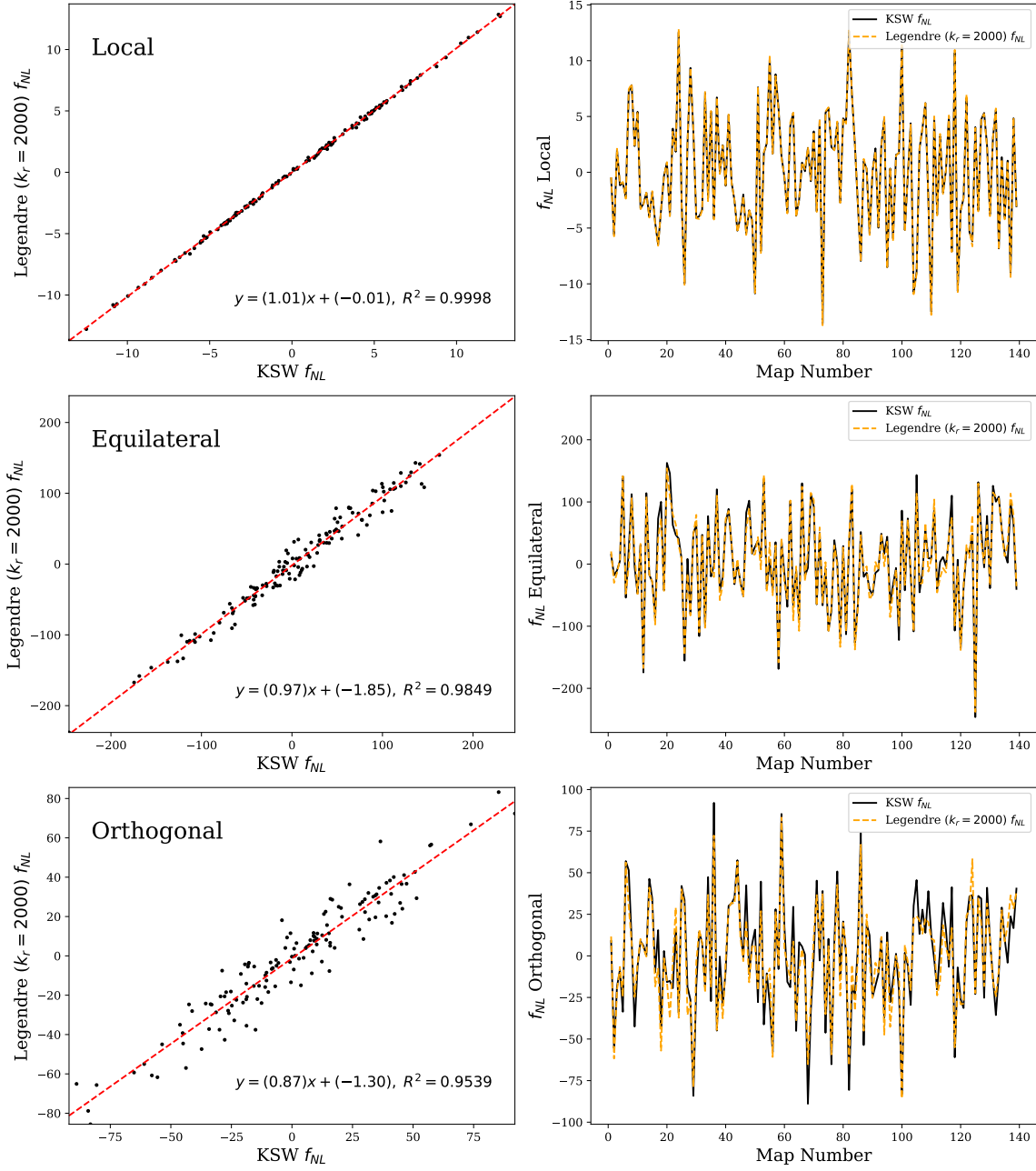


Fig. 5.6 Map-by-map comparison of  $f_{NL}$  estimates for standard templates from the KSW and Legendre basis sets, similar to Figure 5.4. Here, the Legendre basis has a wider  $k$  domain:  $k_{max}/k_{min} = 2000$  instead of the usual 1000. Number of modes ( $p_{max}$ ) has been reduced to 10 instead of 30 for simplicity. We see that additional information from large scales (low  $k$ ) fixes the small scatter present in  $f_{NL}^{local}$  of the previous plot.

Despite the improvements in squeezed limit and local template, we may not simply set  $k_{max}/k_{min} = 2000$  as default because it hurts convergence in other shapes of interest. As can be seen from the Equilateral and Orthogonal plots in Figure 5.6, newer estimates of  $f_{NL}$  are less accurate for shapes other than Local. The fact that  $p_{max} = 10$  here rather than 30 is one of the main causes of the drop in precision, but having smaller  $k$  values within Legendre polynomials' domain also has a negative impact. Shapes with inverse  $k$  scaling vary more dramatically when  $k$  is small and tends to be harder to expand in terms of Legendre polynomials.

For the final check of internal consistency, we inspect how each point in the line of sight integral ( $r$ ) contributes to  $f_{NL}$  estimates. CMB-BEst's formalism makes it straightforward to plot the  $r$  integrand since the integral is done at the very last. Figure 5.7 shows plots of  $f_{NL}$  contributions from different sources and for the three standard bispectrum templates. Shaded in light blue are the  $1\sigma$  regions obtained from 140 simulations for each point in  $r$ .

As illustrated in plots on the right hand side of Figure 5.7, the vast majority of signal comes from recombination around  $r = 14,000\text{Mpc}$ . In fact, its contribution is dominant enough so that neglecting signal from everywhere else would still be a good approximation. CMB-BEst uses an adaptive  $r$  grid which is denser around recombination, following the works of [52]. Other small but notable contributions to the total estimate come from reionisation ( $r \sim 10,000\text{Mpc}$ ) and ISW effect ( $r < 5,000\text{Mpc}$ ).

Zooming in on an interval around recombination, significant contributions from the cubic term to  $f_{NL}$  of Local template is rather prominent (upper left of Figure 5.7). The signal is sufficiently larger than the expected random fluctuations evaluated from Gaussian simulations, which could be hinting non-zero primordial non-Gaussianity. However, contributions from the linear term (shown orange) completely counterbalances it, bringing the total down to values consistent with zero. This again validates accuracy of our methodology; bias to  $f_{NL}$  generated from anisotropic sky masks are precisely subtracted off using the linear terms.

We do not find any statistically significant signal across the whole  $r$  range otherwise, especially when taking look-elsewhere effect into account. It is not meaningful to find a couple  $3\text{-}4\sigma$  values when the other 500 points are simply disregarded. If we detect primordial non-Gaussianity in the future, however, then these plots of  $f_{NL}$  contributions for each  $r$  will provide valuable insights on where the signal comes from.

### 5.3.2 Consistency with Planck

In the last section, we demonstrated how the integrity of CMB-BEst was validated. The next set of validations involves comparing it against other existing codes for CMB bispectrum estimation.

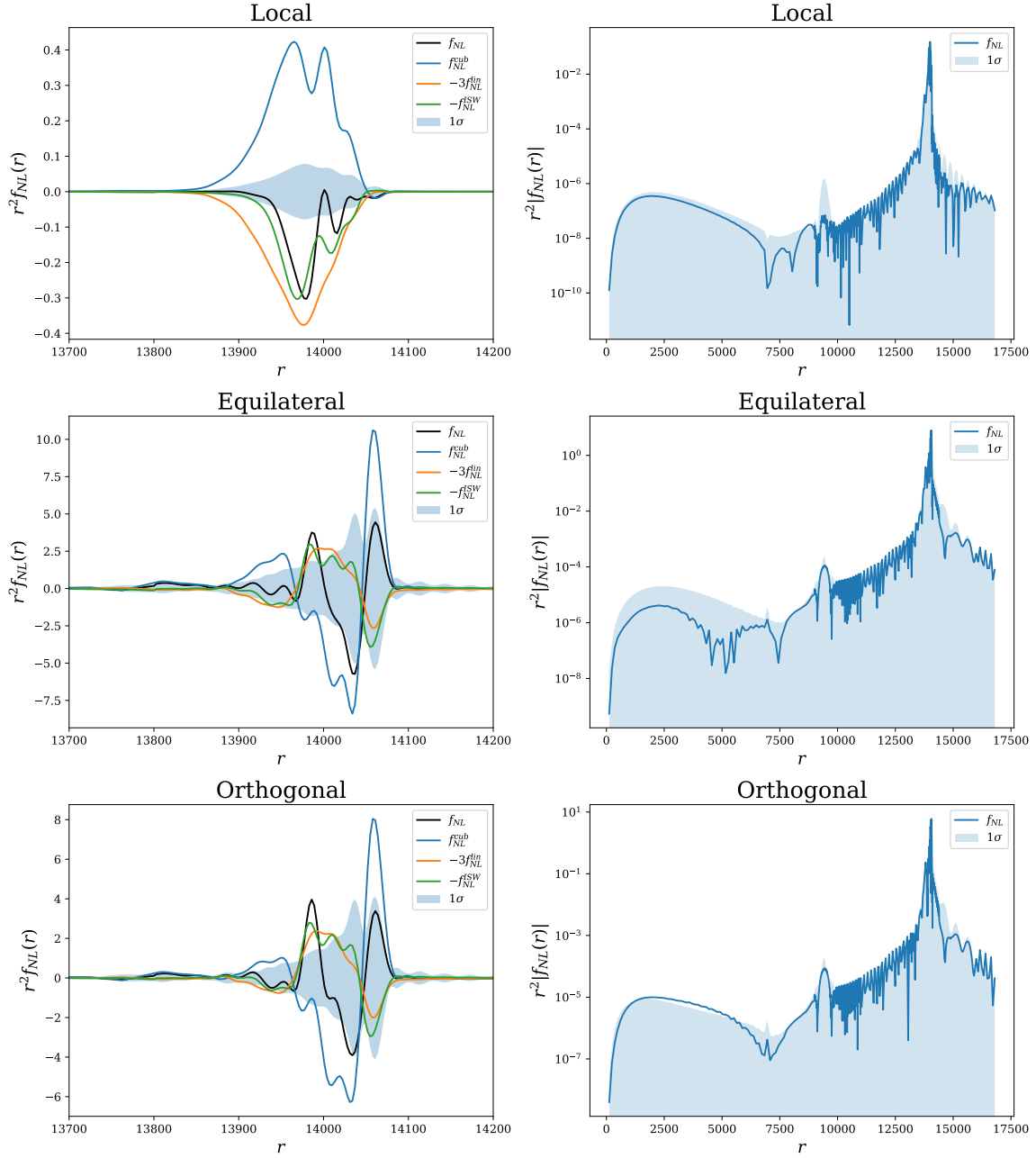


Fig. 5.7 Contributions to the total  $f_{NL}$  from each point in the line-of-sight integral over  $r$  for standard templates. On the left hand side, we plot contributions from the cubic, linear, and lensing-ISW bias, as well as the total  $f_{NL}$ . Shown in blue is the  $1\sigma$  interval obtained from corresponding terms in 140 FFP10 Gaussian simulations. We focus on the  $r$  interval around recombination where most of the signal comes from. Plots on the right hand side show  $f_{NL}$  contributions over the whole  $r$  range in log scale. ISW effect, reionisation, and recombination are responsible for the three most noticeable peaks in all three plots.



We test primordial non-Gaussianity constraints on Local, Equilateral and Orthogonal templates against the Planck 2018 analysis [49]. Two sets of basis functions, KSW and Legendre, have been used to compute  $f_{NL}$  from the foreground-cleaned CMB map included in the final data release. We choose SMICA as the main component separation method since they were shown to be the most reliable and robust for Planck bispectrum analysis [45, 47–49]. Table 5.4 summarises the constraints obtained, together with the quoted results from Planck team’s own KSW estimator and Modal 2 pipeline.

Table 5.4 Constraints on  $f_{NL}$  for the standard shapes from the KSW and Legendre basis of CMB-BEst, in comparison with the Planck 2018 analysis [49]. Only the temperature data from the SMICA foreground-cleaned map and FFP10 simulations were used for the analysis. Values shown are after the lensing bias subtraction, with uncertainties at 68% CL.

Shape	CMB-BEst		Planck 2018	
	KSW	Legendre	KSW	Modal
Local	$-2.2 \pm 5.5$	$-2.0 \pm 5.9$	$-0.5 \pm 5.6$	$-0.6 \pm 6.4$
Equilateral	$17 \pm 61$	$15 \pm 62$	$7 \pm 66$	$34 \pm 67$
Orthogonal	$-7 \pm 38$	$-9 \pm 38$	$-15 \pm 36$	$-26 \pm 43$

Note that while the constraints from CMB-BEst are largely consistent with Planck 2018 results, there are up to  $0.3\sigma$  discrepancies. However, there are variations around this level within the estimates from different pipelines of Planck as well. Equilateral constraints from Planck’s own KSW and Modal estimators shown here, for example, differ by  $\approx 0.4\sigma$ . Similar amount of fluctuations can be found in the full result shown in [49]. Even though in an ideal world they should match exactly across different approaches as long as same dataset is used, statistical significance of the individual  $f_{NL}$ ’s is not largely affected by such variations.

We invested significant proportion of our time investigating this error. Here we discuss three potential sources which might account for the discrepancies. First of all, human error during implementation and estimation process should not be neglected. Bispectrum analysis is complex and computationally expensive. Implementing it often involves writing a long and heavily optimised code. During development and testing stages, we found and fixed many mistakes in our 10,000+ lines of C code. Various unit tests were performed in the process to test individual sections of the code: basis expansion, projection to the  $l$  space, SHTs, parallelisation, and more. Internal consistency checks were then used to verify integrity of the combined pipeline. Planck team also went on lengths to validate and cross-check

different methods [47]. It therefore seems unlikely that simple mistakes are causing the gap in results.

Next source of error we studied is the parameter set. Cosmological parameters we used for constraints in Table 5.4 are identical to those of Planck Modal pipeline. Small changes in cosmological parameters are also shown to have little effect on  $f_{NL}$  [48, 49]. One major difference however, is the number of Gaussian simulations used. We include 140 simulated maps while Modal has about 300. This number is mainly restricted by computational resources required for the large Legendre basis in CMB-BEst. While we found 140 to be sufficient for most cases, sample variance may cause some fluctuations in the linear term and error bar. A rough estimate for sampling error is  $\sim \sqrt{2/N_{sims}} \approx 0.12$ , as calculated in the previous section. Other than  $N_{sims}$ , more internal parameters such as the grid density of discretised arrays have also been checked to yield consistent results when varied.

We are left with systematic errors as potential causes for discrepancies. The most significant bias to  $f_{NL}$  constraints is the lensing-ISW bias. Table 5.5 shows biases from the lensing bispectrum [32] for both CMB-BEst and Planck 2018 analysis. The numbers vary but are consistent overall. Map-by-map comparison of constraints from the Legendre basis and Modal are shown in Figure 5.8.

Table 5.5 Bias to  $f_{NL}$  of standard shapes originating from the lensing bispectrum. We compare CMB-BEst’s two different basis sets and the Planck 2018 analysis [49], using SMICA map and FFP10 simulations.

Shape	CMB-BEst		Planck 2018	
	KSW	Legendre	KSW	Modal
Local	7.5	8.2	7.3	6.9
Equilateral	−0.7	−0.6	−0.7	4.0
Orthogonal	−22	−22	−23	−25

Out of the three templates, local shape shows the largest scatter between constraints. Comparing  $f_{NL}$ ’s of simulated maps from CMB-BEst and Modal, we find correlation of 0.916. The intercept value of 0.78 in the linear fit is mainly due to sample mean present in Modal. Legendre’s sample mean is 0.069 for Local, while Modal has −0.698. Otherwise, the difference between two pipelines are distributed such that its sample standard deviation equals 2.5, skewness is −0.14, and kurtosis is 0.19. Having small  $< 1$  skewness and kurtosis implies that the distribution is close to univariate normal, consistent with random fluctuations.

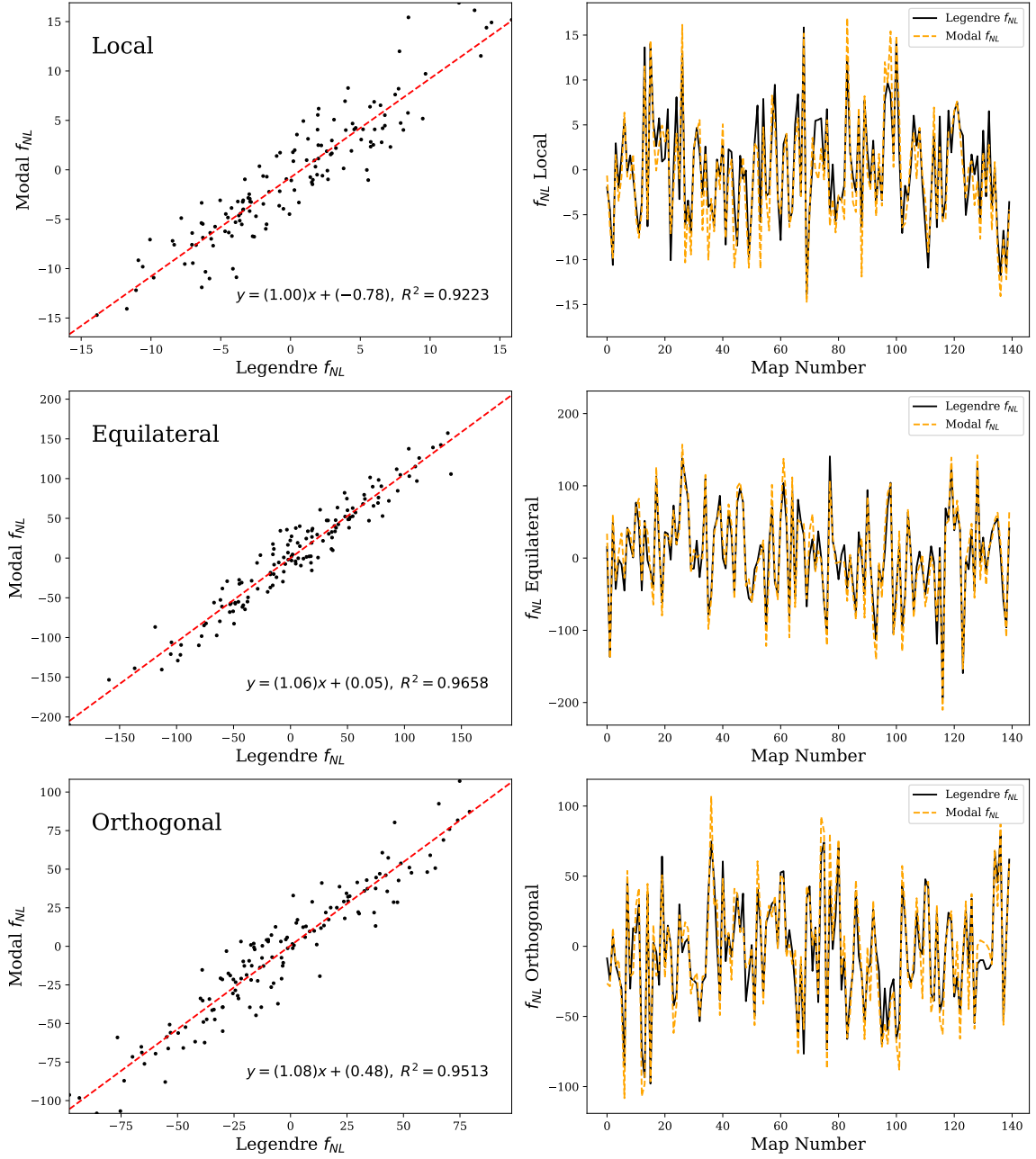


Fig. 5.8 Map-by-map comparison of the  $f_{NL}$  estimates obtained from CMB-BEst's Legendre basis set against the Modal estimator results for Planck 2018 analysis [49]. The first 140 FFP10 simulations are used. On the left hand side are scatter plots where each simulation is represented by a point according to  $f_{NL}$  estimates of standard templates. Their linear best fit lines are shown in dashed red. Results from the two routines are shown map by map on the right hand side. Overall, CMB-BEst and Modal are in good agreement, without any significant systematic errors.

Similarly, we do not find any significant systematic error from Equilateral and Orthogonal shapes either.

Having not found a clear source of error, we conclude that the small gaps between the  $f_{NL}$  estimates in Table 5.4 mainly come from differences in methodology and are consistent with random fluctuations.

We now move on to constraining models with oscillations. The simplest template for oscillatory models is the feature model studied in Chapter 4. We use a template shape function of form  $S^{feat}(k_1, k_2, k_3) = \sin(\omega(k_1 + k_2 + k_3) + \phi)$ . Figure 5.9 shows  $f_{NL}$  constraints obtained from the Legendre basis and compares them with Modal results from Planck 2018 analysis. The ‘phase’  $\phi$  is set to zero, while oscillation ‘frequency’  $\omega$  was varied from 10 Mpc to 350 Mpc. We follow [21] and increase  $\omega$  in steps of 10, so that correlation between shapes with different  $\omega$  is kept low.

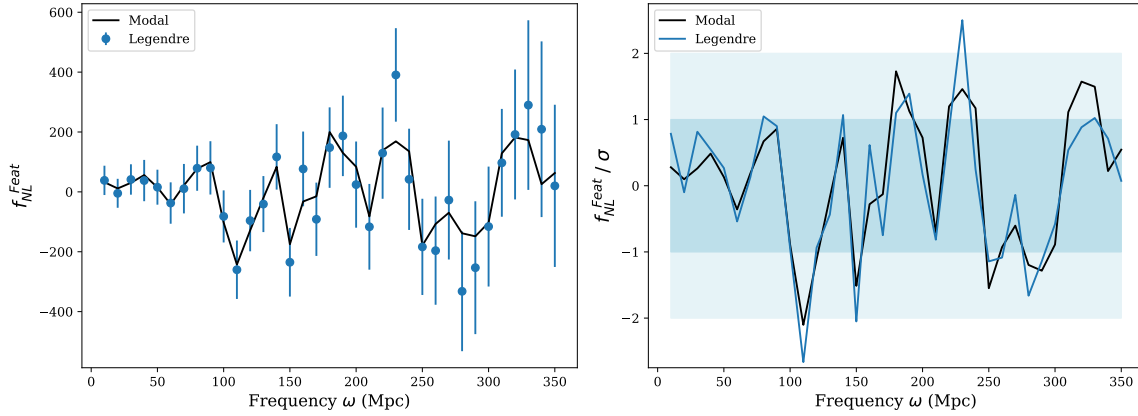


Fig. 5.9 Estimated  $f_{NL}$ 's for feature models with shape  $S(k_1, k_2, k_3) = \sin(\omega(k_1 + k_2 + k_3))$ , obtained using the Legendre basis with (blue) and Planck's Modal (black). Left: direct comparison of  $f_{NL}$  for different values of  $\omega$ . Error bars indicate the expected standard deviation in the estimator, calculated using 140 Gaussian simulations. Right: measured signal-to-noise  $f_{NL}/\sigma$ , again for a range of  $\omega$  values. Shaded in blue are the  $1\sigma$  and  $2\sigma$  levels. We see that the two approaches yield coherent estimates overall.

The Legendre basis accurately expands the feature model template using Legendre polynomials via basis expansion outlined in (5.28). Estimates from the two methods, CMB-BEst's Legendre and Planck's Modal, are mostly compatible. The most notable difference is at  $\omega = 230\text{Mpc}$  where  $f_{NL}$  from Legendre is more than  $1\sigma$  larger compared to Modal. Even though it is interesting that the new estimate now passes the  $2\sigma$  threshold, having one such point out of 35 shown here has less statistical significance.

Both Legendre and Modal approaches involve expanding the shape function with respect to a polynomial basis. Polynomials are versatile but has limited resolution for oscillatory

signals; it cannot resolve shape with number of oscillations greater than the maximum degree of polynomials ( $p_{max}$  here). For the Legendre basis with  $k$  range  $[2.09 \times 10^{-4}, 2.09 \times 10^{-1}] \text{Mpc}^{-1}$  and  $p_{max} = 30$ , frequencies greater than  $\pi p_{max}/(k_{max} - k_{min}) \approx 436 \text{Mpc}$  are unresolvable. In reality, numerics start to break before this value. We do not have a reference analytic value for true  $f_{NLS}$ , but evaluating correlations between shapes is effective for checking our numerics.

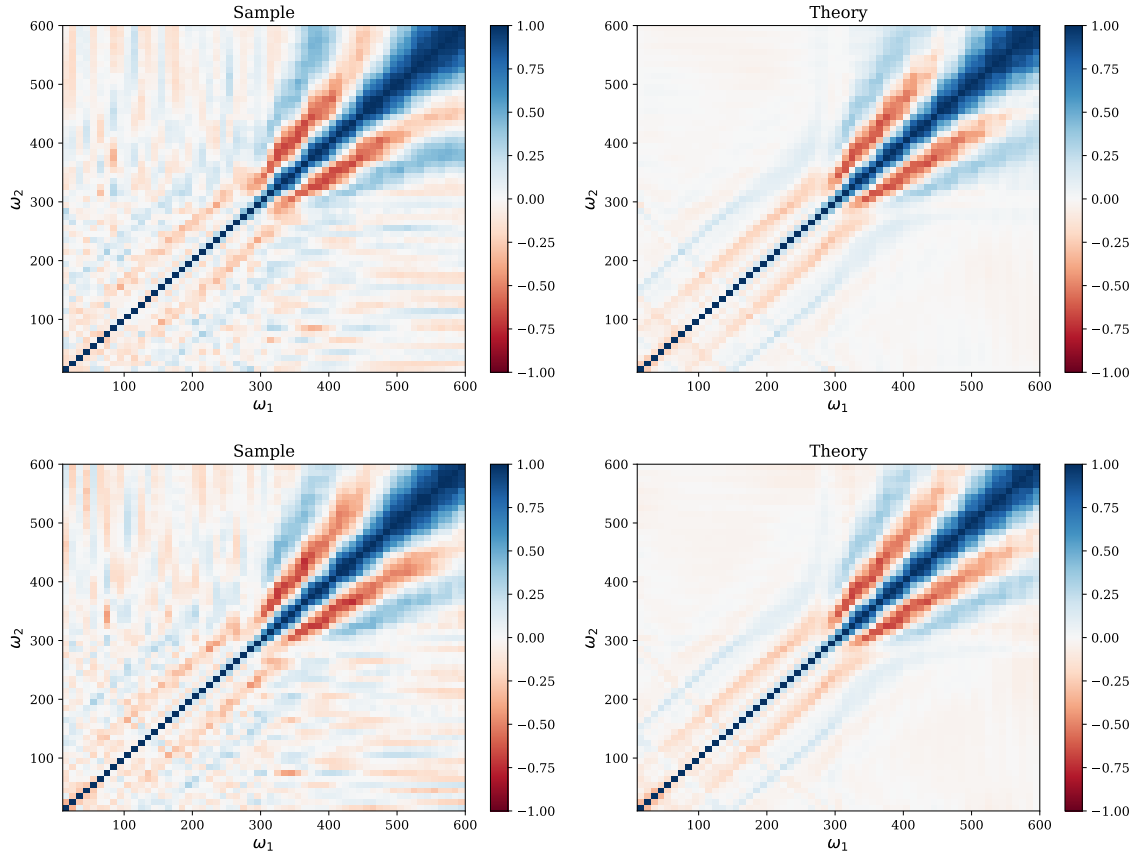


Fig. 5.10 Correlations between feature model templates  $S(k_1, k_2, k_3) = \sin(\omega(k_1 + k_2 + k_3) + \phi)$  with different  $\omega$  values, for  $\phi = 0$  (top two) and  $\phi = \pi/2$  (bottom two). Results are from Legendre basis. ‘Sample’ correlations are obtained from the  $f_{NL}$  estimates from 140 Gaussian simulations, while ‘theory’ correlations come from the inner product induced by  $\Gamma_{p_1 p_2 p_3, p_1 p_2 p_3}$  matrix in (5.11). Large non-diagonal correlations appear around  $\omega \approx 300$ , after which oscillations in the shape are no longer resolved by polynomials of degree up to  $p_{max}$ .

Figure 5.10 shows correlations between  $f_{NLS}$  from feature models with different frequency  $\omega$ s. The plots show correlation between  $f_{NL}$  estimates from 140 FFP10 Gaussian simulations (‘sample’), together with the one evaluated using our ‘late-time’ inner product (‘theoretical’)

given by

$$\langle b^{(i)}, b^{(j)} \rangle = \sum_{l_j} \frac{h_{l_1 l_2 l_3}^2 b_{l_1 l_2 l_3}^{(i)} b_{l_1 l_2 l_3}^{(j)}}{C_{l_1} C_{l_2} C_{l_3}} \quad (5.33)$$

$$= \sum_{p_j p'_j} \alpha_{p_1 p_2 p_3}^{(i)} \alpha_{p'_1 p'_2 p'_3}^{(j)} \sum_{l_j} \frac{h_{l_1 l_2 l_3}^2 (b_{p_1 p_2 p_3}^{(i)})_{l_1 l_2 l_3} (b_{p'_1 p'_2 p'_3}^{(j)})_{l_1 l_2 l_3}}{C_{l_1} C_{l_2} C_{l_3}} \quad (5.34)$$

$$= \sum_{p_j p'_j} \alpha_{p_1 p_2 p_3}^{(i)} \alpha_{p'_1 p'_2 p'_3}^{(j)} \Gamma_{p_1 p_2 p_3, p'_1 p'_2 p'_3} \quad (5.35)$$

$$= \alpha^{(i)} \Gamma \alpha^{(j)}, \quad (5.36)$$

where  $\Gamma$  is defined in (5.11). In the limit  $N_{sims} \rightarrow \infty$ , the sample correlation can be shown to approach the theoretical value in the weakly non-Gaussian limit. We see from Figure 5.10 that they indeed display the same qualitative behaviour for  $N_{sims} = 140$ .

The templates with  $\omega < 300$  are highly uncorrelated with each other, as can be seen from small non-diagonal elements. Noticeable correlations on lines  $\omega_2 = \omega_1 \pm c$  for  $c = 70, 140$  arise from resonance between oscillations and transfer functions at the Baryonic Acoustic Oscillation (BAO) scale, as we observed in Figure 4.7. Faint lines can also be found near  $\omega_2 = -\omega_1 + c$ ,  $c = 70, 140, 210, \dots$  for similar reasons.

When  $\omega > 300$ , however, large non-diagonal correlations appear. This is about when the oscillation frequency surpasses the resolution set by the highest degree of polynomials. Our basis expansion becomes inaccurate after this point. There are interesting linear structures present, with slopes roughly equal to  $2, 1/2$  and subsequently  $4, 1/4$ . These lines come from aliasing caused by subsampling rapid oscillations; our basis picks up  $\omega' = \omega/2$  signal instead.  $\omega_2/2 = -\omega_1 + 70$  and other pairs of  $(\omega_1, \omega_2)$  resonate to give large non-diagonal correlations.

We verify our claim that numerical inaccuracies at high  $\omega$ s are caused by the lack of resolution due to limited number of polynomial modes. Figure 5.11 illustrates how having smaller  $k$  range allows us to constrain faster oscillations more accurately. Note that we also change  $l_{max}$  correspondingly since smaller scales are neglected. Plot on the right hand side uses Legendre basis with  $(k_{min}, k_{max})$  range rescaled by a factor of  $3/4$ . Fewer oscillations appear within the  $k$  interval and are therefore easier to expand using fewer polynomials. As we expected, the scale at which non-diagonal correlations blow up is now shifted to a higher frequency,  $\omega \approx (4/3) \cdot 300$ .

There is one subtlety about  $f_{NL}$  estimates obtained from inaccurate primordial basis expansions. CMB-BEst computes  $\beta$ s and  $\Gamma$ s with respect to the fixed Legendre basis, which

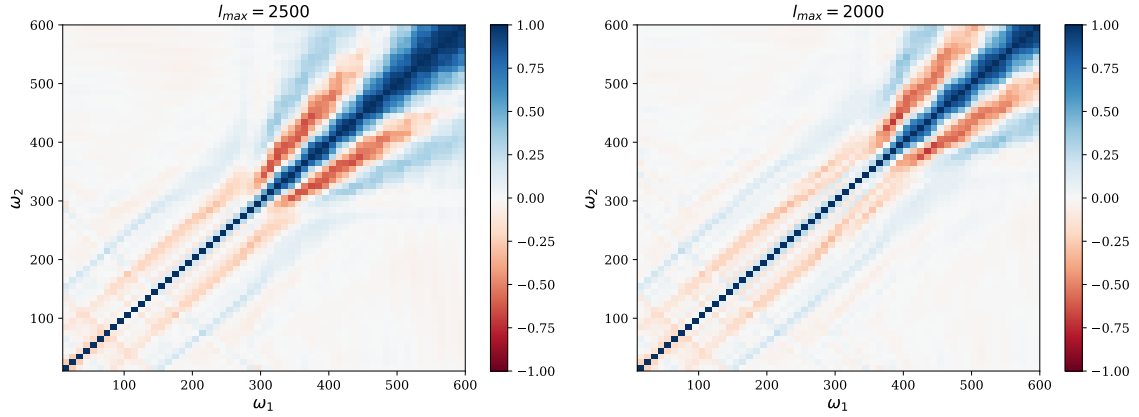


Fig. 5.11 Theoretical correlations between feature model templates with different frequency  $\omega$ s, as described in Figure 5.10. The phase  $\phi$  is set to zero in both cases, while the right plot is obtained from Legendre basis with a different  $k$  range. The maximum  $l$  value is reduced from 2500 to 2000, shifting  $(k_{min}, k_{max})$  by a factor of  $2000/2500 = 0.75$ . Having smaller  $k$  range means fewer oscillations within the  $k$  interval for same  $\omega$ , which provides better effective resolution. The right plot does indeed show smaller non-diagonal correlations at high frequencies.

has been shown to be accurate even for the highest degree of polynomials. When the primordial basis is unable to resolve rapid modulations as we have seen, the  $f_{NL}$  estimates we obtain are nevertheless meaningful; they are simply probing the wrong model. The constraints are not for the given shape function, but rather its projection to the vector subspace spanned by the basis functions as shown in (5.24). Detecting non-zero  $f_{NL}$  here is can still have significant implications.

Another popular template for models with oscillations is the ‘resonance’ shape parametrised as  $S(k_1, k_2, k_3) = \sin(\omega \log(k_1 + k_2 + k_3) + \phi)$ . Log-spaced modulations are numerically harder to deal with since the oscillation frequency diverges as  $k \rightarrow 0$ . Note also that any scaling factors to the  $k$ ’s can be absorbed into the phase via  $\log(c(k_1 + k_2 + k_3)) = \log(k_1 + k_2 + k_3) + \log(c)$ . For our Legendre basis with  $k_{max}/k_{min}$  fixed to 1000, the full  $k$  range includes  $\approx 1.1\omega$  oscillations. Any frequency larger than  $\approx 27$  therefore cannot be expanded using  $p_{max} = 30$  polynomials. We still explore shapes with higher  $\omega$ s however, since the basis can pick up slower oscillations in higher  $k$  values. Corresponding constraints should be taken with a grain of salt; they probe bispectrum shapes *similar* to the resonance template. Low- $k$  oscillations are especially likely to be wiped out from these shapes.

Figure 5.12 compares  $f_{NL}$  constraints for the resonance template over a range of  $\omega$ s. As can be seen from the top two plots, the signal-to-noise values obtained from Legendre basis and Modal are relatively consistent up until  $\omega \approx 35$ , after which the two results start

diverging significantly. The threshold is about the same for ‘sinlog’ ( $\phi = 0$ ) and ‘coslog’ ( $\phi = \pi/2$ ) shapes.

Recall that the sample  $\sigma$  from  $f_{NL}$  estimates of Gaussian simulations should converge to the theoretical value calculated from Fisher information as  $N_{sims} \rightarrow \infty$ , since the CMB bispectrum estimator is optimal. We have checked that the sample and theoretical variances are consistent for standard templates in Section 5.3.1, using both KSW and Legendre basis sets. The bottom two plots in Figure 5.9 show the equivalent results for resonance template with varying  $\omega$ .

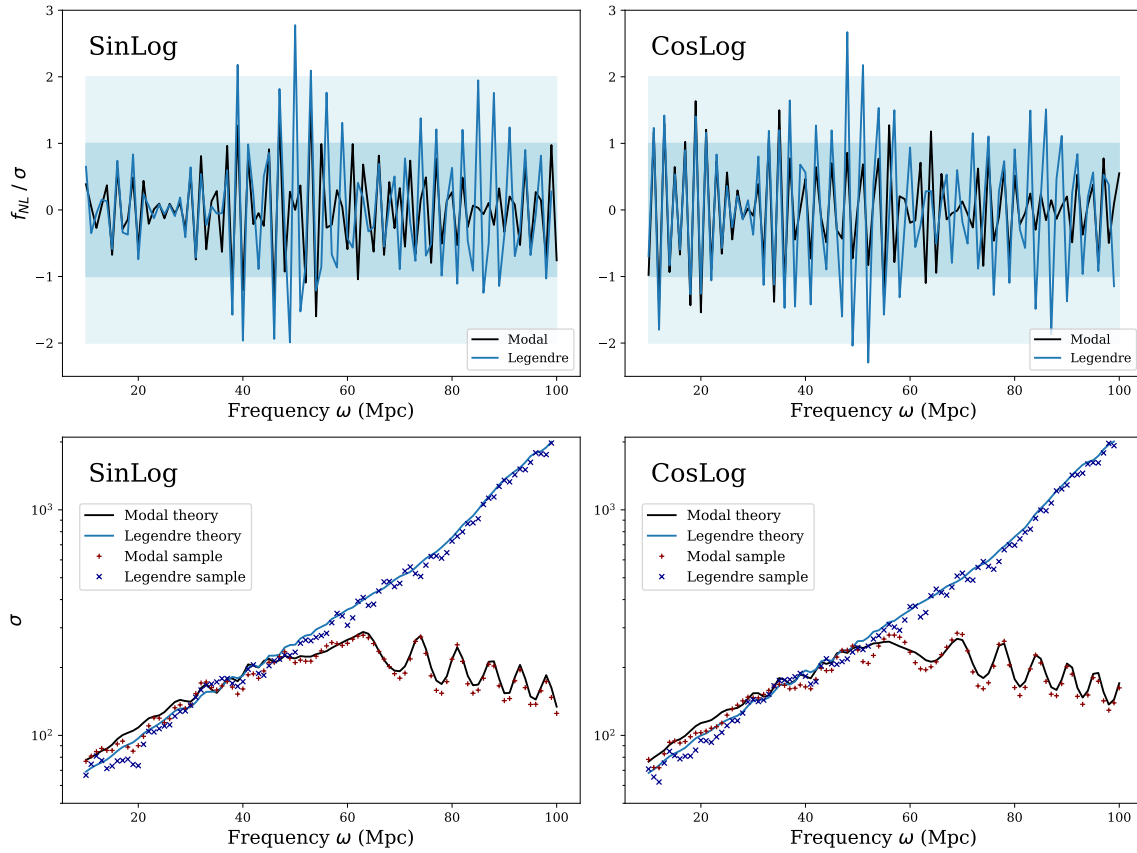


Fig. 5.12 Constraints for the resonance shape  $S(k_1, k_2, k_3) = \sin(\omega \log(k_1 + k_2 + k_3) + \phi)$  with varying  $\omega$ s and  $\phi$  set to 0 (left) and  $\pi/2$  (right). Results are obtained using CMB-BEst’s Legendre basis (blue) and Planck’s Modal estimator (black). Top: signal-to-noise significance of the estimated  $f_{NL}$ s with  $1\sigma$  and  $2\sigma$  levels shaded in blue. Bottom: standard deviations of the  $f_{NL}$  estimates against frequency  $\omega$ , calculated from the  $f_{NL}$ s of 140 simulations (sample) and the  $\Gamma$  matrix (theory).

Similarly to the feature models studied in Chapter 4, uncertainty in the estimated  $f_{NL}$ s increases as we raise  $\omega$ , exploring more rapid oscillations in bispectrum. Both Modal and Legendre methods lose their ability to resolve shapes with  $\omega$ s larger than 35. The constraints



are then no longer for the precise resonance shape but rather an approximation to it. A notable difference between Modal and CMB-BEst's Legendre basis is their behaviour at high  $\omega$ . Modal's numerical accuracy is completely lost after  $\omega \approx 50$ , leading to disproportionately large bispectra and small  $\sigma$ . On the other hand, Legendre retains stability in its basis expansion, yielding constraints for approximate bispectrum shapes closest to the true, high-frequency ones.

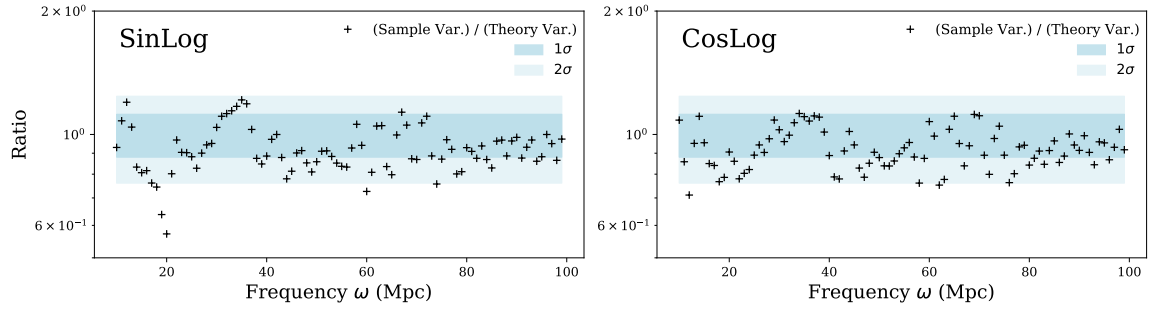


Fig. 5.13 Ratio between sample and theoretical variances obtained from Legendre basis for resonance shapes. Sampled variance is calculated from  $f_{NL}$  estimates of 140 Gaussian simulations.  $1\sigma$  and  $2\sigma$  intervals are chosen based on a  $\chi^2$ -distribution, which accurately describes sample variances as long as the  $f_{NL}$ s are normally distributed. Results are statistically consistent with random fluctuations except potentially one at  $\omega = 20$ , discussed in the main text.

A detailed comparison between the sample and theoretical variances is depicted in Figure 5.13. This serves as a useful consistency check within the CMB-BEst pipeline. Sample variances are calculated from finite number of  $f_{NL}$  samples from simulations. We test if these estimates are compatible with the underlying distribution:  $\chi^2$  with  $N_{sims} - 1$  degrees of freedom in this case. We achieve the desired consistency for both  $\phi = 0$  and  $\phi = \pi/2$ . One potential meaningful outlier is at  $\omega = 20$  and  $\phi = 0$ , where the sample estimate is below 60% of the expected level. This feature is not likely to be a numerical error specific to CMB-BEst since a similar dip can be found in Modal from Figure 5.12. No significant irregularity is found for different phases at the same frequency. We classify this point as a random fluctuation for now, but a further investigation using an independent set of Gaussian simulations would be useful.

As with the feature models before, we plot the correlation matrix between the templates with different  $\omega$ s in Figure 5.14. Shapes with similar  $\omega$ s are naturally correlated, but most off-diagonal terms of the matrix vanish. Even for  $\omega > 35$  where the basis expansion become less accurate, cross-correlations tend to remain small until  $\omega \approx 75$ . We verify the stability of CMB-BEst's Legendre basis expansion; best approximations to the highly oscillatory

template is found, allowing us to continue exploring independent bispectrum shapes with the characteristic log-spaced oscillations.

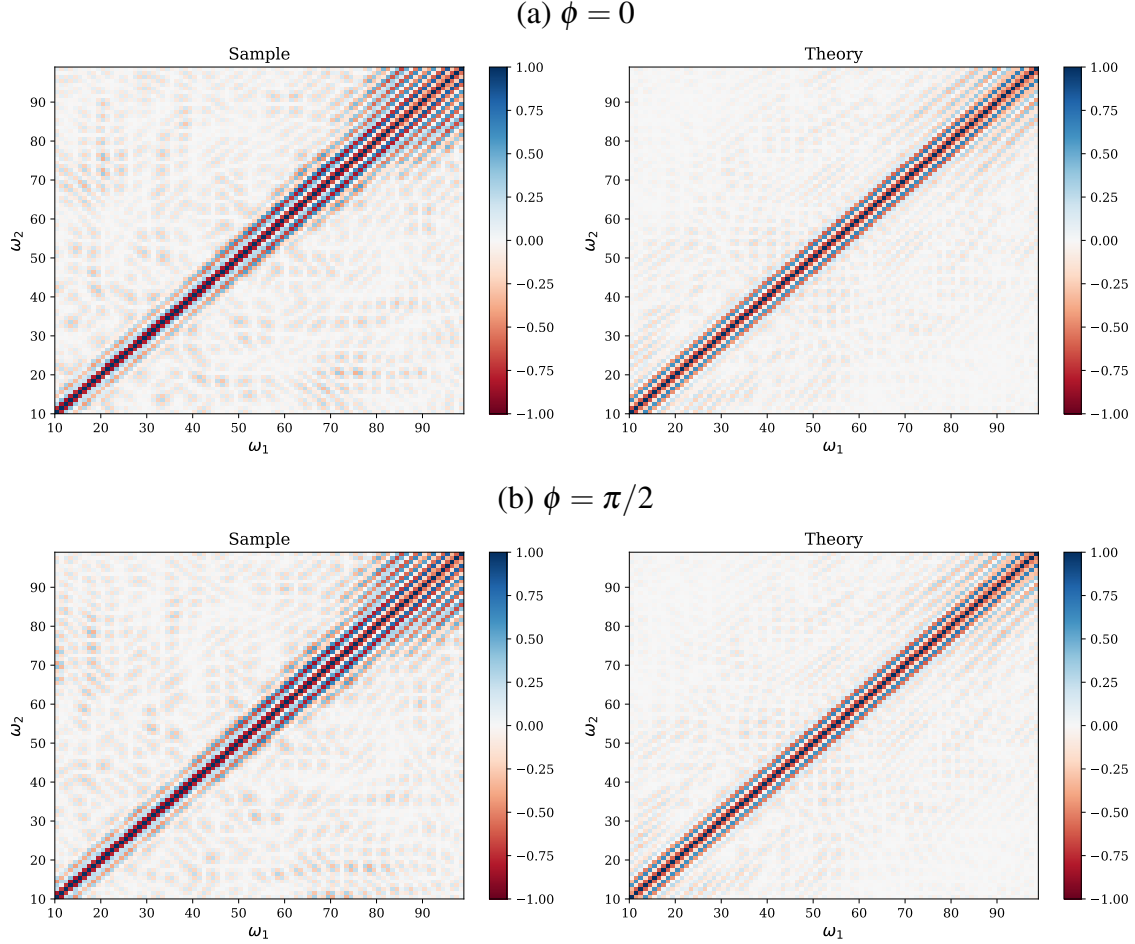


Fig. 5.14 Correlations between resonance model templates  $S(k_1, k_2, k_3) = \sin(\omega \log(k_1 + k_2 + k_3) + \phi)$  with different  $\omega$  values, for (a)  $\phi = 0$  and (b)  $\phi = \pi/2$ . ‘Sample’ correlations are obtained from the Legendre basis  $f_{NL}$  estimates from 140 Gaussian simulations. ‘Theory’ correlations come from the inner product induced by  $\Gamma$  matrix as shown in (5.36).

### 5.3.3 Proof of concept

*Primodal* is an efficient numerical code for computing bispectra of primordial perturbations using the in-in formalism [15]. Unlike many in-in codes, the computed bispectrum is expressed as coefficients of a separable basis expansion as opposed to a grid of discrete points. Choosing an equivalent basis set for *CMB-BE* therefore allows a direct link between the two codes. The combined pipeline is capable of constraining specific inflation models

directly. Template-free bispectrum analysis will also enable fast and extensive scan of theory parameters.

- DBI sound speed constraints - DBI resonance scan - tetrapyd decomp?

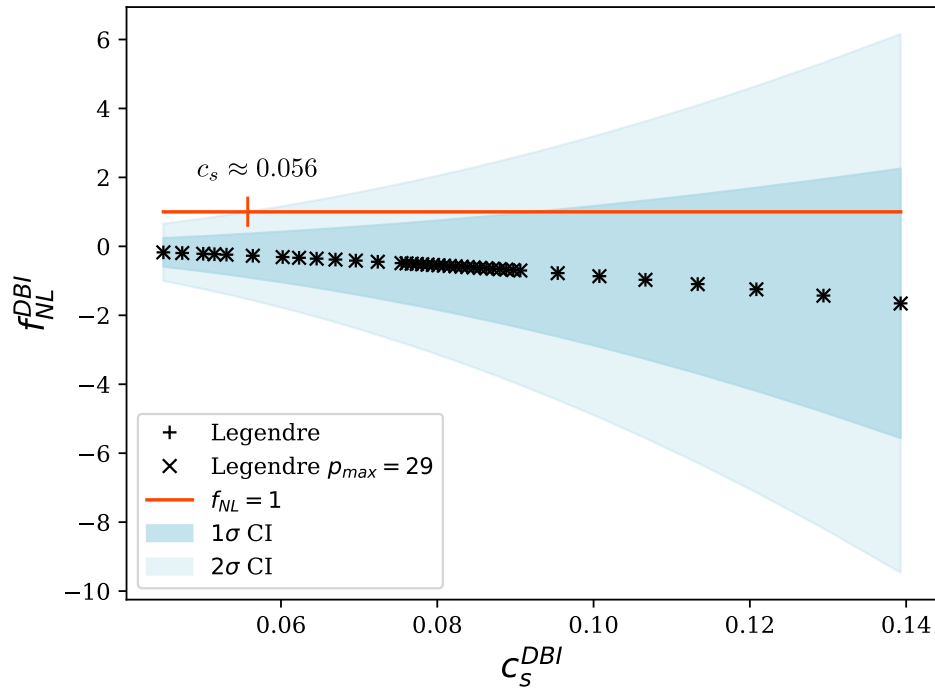


Fig. 5.15 DBI sound speed scan

### 5.3.4 Future work



# References

- [1] Achúcarro, A., Gong, J. O., Hardeman, S., Palma, G. A., and Patil, S. P. (2011). Features of heavy physics in the CMB power spectrum. *Journal of Cosmology and Astroparticle Physics*, 2011(1).
- [2] Adams, J., Easter, R., and Cresswell, B. (2001). Inflationary perturbations from a potential with a step. *Physical Review D - Particles, Fields, Gravitation and Cosmology*, 64(12):6.
- [3] Adshead, P., Dvorkin, C., Hu, W., and Lim, E. A. (2012). Non-Gaussianity from step features in the inflationary potential. *Physical Review D - Particles, Fields, Gravitation and Cosmology*, 85(2):1–26.
- [4] Ballardini, M., Finelli, F., Fedeli, C., and Moscardini, L. (2016). Probing primordial features with future galaxy surveys. *Journal of Cosmology and Astroparticle Physics*, 2016(10).
- [5] Bartolo, N., Cannone, D., and Matarrese, S. (2013). The effective field theory of inflation models with sharp features. *Journal of Cosmology and Astroparticle Physics*, 2013(10).
- [6] Benetti, M. and Alcaniz, J. S. (2016). Bayesian analysis of inflationary features in Planck and SDSS data. *Physical Review D*, 94(2):1–8.
- [7] Benetti, M., Lattanzi, M., Calabrese, E., and Melchiorri, A. (2011). Features in the primordial spectrum: New constraints from WMAP7 and ACT data and prospects for the Planck mission. *Physical Review D - Particles, Fields, Gravitation and Cosmology*, 84(6):1–8.
- [8] Bucher, M., van Tent, B., and Carvalho, C. S. (2010). Detecting bispectral acoustic oscillations from inflation using a new flexible estimator. *Monthly Notices of the Royal Astronomical Society*, 407(4):2193–2206.
- [9] Cardoso, J.-F., Le Jeune, M., Delabrouille, J., Betoule, M., and Patanchon, G. (2008). Component separation with flexible models—application to multichannel astrophysical observations. *IEEE Journal of Selected Topics in Signal Processing*, 2(5):735–746.
- [10] Chantavat, T., Gordon, C., and Silk, J. (2011). Large scale structure forecast constraints on particle production during inflation. *Physical Review D - Particles, Fields, Gravitation and Cosmology*, 83(10):1–9.
- [11] Chen, X. (2010). Primordial non-gaussianities from inflation models. *Advances in Astronomy*, 2010(ii).

- [12] Chen, X., Dvorkin, C., Huang, Z., Namjoo, M. H., and Verde, L. (2016). The future of primordial features with large-scale structure surveys. *Journal of Cosmology and Astroparticle Physics*, 2016(11).
- [13] Chen, X., Easther, R., and Lim, E. A. (2007). Large non-Gaussianities in single-field inflation. *Journal of Cosmology and Astroparticle Physics*, 06(6).
- [14] Chluba, J., Hamann, J., and Patil, S. P. (2015). Features and New Physical Scales in Primordial Observables: Theory and Observation. 24(10):1–133.
- [15] Clarke, P. and Shellard, E. P. S. (2021). Probing inflation with precision bispectra.
- [16] Dicke, R. H., Peebles, P. J. E., Roll, P. G., and Wilkinson, D. T. (1965). Cosmic black-body radiation. *The Astrophysical Journal*, 142:414–419.
- [17] Dvorkin, C. and Hu, W. (2010). Generalized slow roll approximation for large power spectrum features. *Physical Review D - Particles, Fields, Gravitation and Cosmology*, 81(2):1–14.
- [18] et al, K. N. A. (2016). CMB-S4 Science Book, First Edition.
- [19] Fergusson, J., Liguori, M., and Shellard, E. (2010). General cmb and primordial bispectrum estimation: Mode expansion, map making, and measures of  $f_{NL}$ . *Physical Review D*, 82(2):023502.
- [20] Fergusson, J. R. (2014). Efficient optimal non-Gaussian CMB estimators with polarization. *Physical Review D - Particles, Fields, Gravitation and Cosmology*, 90(4).
- [21] Fergusson, J. R., Gruetjen, H. F., Shellard, E. P., and Liguori, M. (2015a). Combining power spectrum and bispectrum measurements to detect oscillatory features.
- [22] Fergusson, J. R., Gruetjen, H. F., Shellard, E. P., and Wallisch, B. (2015b). Polyspectra searches for sharp oscillatory features in cosmic microwave sky data. *Physical Review D - Particles, Fields, Gravitation and Cosmology*, 91(12).
- [23] Fergusson, J. R., Liguori, M., and Shellard, E. P. S. (2012). The CMB bispectrum. *Journal of Cosmology and Astroparticle Physics*, 2012(12).
- [24] Gorski, K. M., Hivon, E., Banday, A. J., Wandelt, B. D., Hansen, F. K., Reinecke, M., and Bartelmann, M. (2005). Healpix: A framework for high-resolution discretization and fast analysis of data distributed on the sphere. *The Astrophysical Journal*, 622(2):759.
- [25] Hale, N. and Townsend, A. (2013). Fast and Accurate Computation of Gauss–Legendre and Gauss–Jacobi Quadrature Nodes and Weights. *SIAM journal on scientific computing*, 35(2):A652—A674.
- [26] Hazra, D. K., Shafieloo, A., Smoot, G. F., and Starobinsky, A. A. (2014). Wiggly whipped inflation. *Journal of Cosmology and Astroparticle Physics*, 2014(8).
- [27] Hu, B. and Torrado, J. (2015). Searching for primordial localized features with CMB and LSS spectra. *Physical Review D - Particles, Fields, Gravitation and Cosmology*, 91(6):1–10.

- [28] Intel (2019). *Second generation Intel Xeon Scalable Processors. Datasheet, Volume One, Electrical.*
- [29] Jeffers, J., Reinders, J., and Sodani, A. (2016). *Intel Xeon Phi Processor High Performance Programming: Knights Landing Edition.* Elsevier Science.
- [30] Komatsu, E. (2010). Hunting for Primordial Non-Gaussianity in the Cosmic Microwave Background. *Classical and Quantum Gravity*, 27.
- [31] Komatsu, E., Spergel, D. N., and Wandelt, B. D. (2005). Measuring Primordial Non-Gaussianity in the Cosmic Microwave Background. *The Astrophysical Journal*, 634(1):14–19.
- [32] Lewis, A., Challinor, A., and Hanson, D. (2011). The shape of the CMB lensing bispectrum. *Journal of Cosmology and Astroparticle Physics*, 2011(03):018.
- [33] Lewis, A., Challinor, A., and Lasenby, A. (2000). Efficient Computation of Cosmic Microwave Background Anisotropies in Closed Friedmann-Robertson-Walker Models. *The Astrophysical Journal*, 538(2):473–476.
- [34] Liguori, M., Sefusatti, E., Fergusson, J. R., and Shellard, E. P. (2010). Primordial non-gaussianity and bispectrum measurements in the cosmic microwave background and large-scale structure. *Advances in Astronomy*, 2010.
- [35] Maldacena, J. (2002). Non-Gaussian features of primordial fluctuations in single field inflationary models. *Journal of High Energy Physics*, 2003(05):13.
- [36] Martin, J. and Ringeval, C. (2004). Superimposed oscillations in the WMAP data? *Physical Review D - Particles, Fields, Gravitation and Cosmology*, 69(8):9.
- [37] Meerburg, P. D., Spergel, D. N., and Wandelt, B. D. (2014a). Searching for oscillations in the primordial power spectrum. I. Perturbative approach. *Physical Review D - Particles, Fields, Gravitation and Cosmology*, 89(6):19–26.
- [38] Meerburg, P. D., Spergel, D. N., and Wandelt, B. D. (2014b). Searching for oscillations in the primordial power spectrum. II. Constraints from Planck data. *Physical Review D - Particles, Fields, Gravitation and Cosmology*, 89(6):1–6.
- [39] Meerburg, P. D., Van Der Schaar, J. P., and Corasaniti, P. S. (2009). Signatures of initial state modifications on bispectrum statistics. *Journal of Cosmology and Astroparticle Physics*, 2009(5).
- [40] Meerburg, P. D., Wijers, R. A., and van der Schaar, J. P. (2012). WMAP7 constraints on oscillations in the primordial power spectrum. *Monthly Notices of the Royal Astronomical Society*, 421(1):369–380.
- [41] Miranda, V., Hu, W., and Adshead, P. (2012). Warp features in DBI inflation. *Physical Review D - Particles, Fields, Gravitation and Cosmology*, 86(6):1–10.
- [42] Münchmeyer, M., Bouchet, F., Jackson, M. G., and Wandelt, B. (2014). The Komatsu Spergel Wandelt estimator for oscillations in the cosmic microwave background bispectrum. *Astronomy & Astrophysics*, 570:A94.

- [43] Ng, K. W. and Liu, G. C. (1999). Correlation Functions of Cmb Anisotropy and Polarization. *International Journal of Modern Physics D*, 08(01):61–83.
- [44] Penzias, A. A. and Wilson, R. W. (1965). A measurement of excess antenna temperature at 4080 mc/s. *The Astrophysical Journal*, 142:419–421.
- [45] Planck Collaboration.
- [46] Planck Collaboration. Planck 2015 results. XII. Full Focal Plane Simulations. *Astronomy & Astrophysics*.
- [47] Planck Collaboration (2014). Planck 2013 results. XXIV. Constraints on primordial non-Gaussianity. *Astronomy & Astrophysics*, 571:A24.
- [48] Planck Collaboration (2016). Planck 2015 results. XVII. Constraints on primordial non-Gaussianity. *Astronomy & Astrophysics*, 594:A17.
- [49] Planck Collaboration (2020a). Planck 2018 results. ix. constraints on primordial non-gaussianity. *Astronomy & Astrophysics*, 641:A9.
- [50] Planck Collaboration (2020b). Planck 2018 results. vi. cosmological parameters. *Astronomy & Astrophysics*, 641:A6.
- [51] Reinecke, M. and Seljebotn, D. S. (2013). Libsharp–spherical harmonic transforms revisited. *Astronomy & Astrophysics*, 554:A112.
- [52] Smith, K. M. and Zaldarriaga, M. (2011). Algorithms for bispectra: Forecasting, optimal analysis and simulation. *Monthly Notices of the Royal Astronomical Society*, 417(1):2–19.
- [53] Starobinsky, A. (1992). Aa starobinsky, jetp lett. 55, 489 (1992). *JETP Lett.*, 55:489.
- [54] The CORe collaboration (2015). CORe (Cosmic Origins Explorer) White Paper.
- [55] The Simons Observatory Collaboration (2018). The Simons Observatory: Science goals and forecasts.
- [56] Yadav, A. P. S., Komatsu, E., and Wandelt, B. D. (2007). Fast Estimator of Primordial Non-Gaussianity from Temperature and Polarization Anisotropies in the Cosmic Microwave Background. pages 1–15.